

**Observations and modelling of birch pollen
emission and dispersion from an isolated source**

Inauguraldissertation

zur
Erlangung der Würde eines Doktors der Philosophie
vorgelegt der
Philosophisch-Naturwissenschaftlichen Fakultät
der Universität Basel

von

Dominik Michel
aus Basel, CH

Basel, 2014

Genehmigt von der Philosophisch-Naturwissenschaftlichen Fakultät

auf Antrag von

Prof. Dr. Eberhard Parlow
Meteorologie, Klimatologie und Fernerkundung
Departement Umweltwissenschaften
Universität Basel
Schweiz

und

Prof. Dr. Mathias W. Rotach
Institut für Meteorologie und Geophysik
Fakultät für Geo- und Atmosphärenwissenschaften
Universität Innsbruck
Österreich

Basel, den 10.12.2013

Prof. Dr. Jörg Schibler
Dekan



Namensnennung-Keine kommerzielle Nutzung-Keine Bearbeitung 3.0 Schweiz
(CC BY-NC-ND 3.0 CH)

Sie dürfen: Teilen — den Inhalt kopieren, verbreiten und zugänglich machen

Unter den folgenden Bedingungen:



Namensnennung — Sie müssen den Namen des Autors/Rechteinhabers in der von ihm festgelegten Weise nennen.



Keine kommerzielle Nutzung — Sie dürfen diesen Inhalt nicht für kommerzielle Zwecke nutzen.



Keine Bearbeitung erlaubt — Sie dürfen diesen Inhalt nicht bearbeiten, abwandeln oder in anderer Weise verändern.

Wobei gilt:

- **Verzichtserklärung** — Jede der vorgenannten Bedingungen kann **aufgehoben** werden, sofern Sie die ausdrückliche Einwilligung des Rechteinhabers dazu erhalten.
- **Public Domain (gemeinfreie oder nicht-schützbarer Inhalte)** — Soweit das Werk, der Inhalt oder irgendein Teil davon zur Public Domain der jeweiligen Rechtsordnung gehört, wird dieser Status von der Lizenz in keiner Weise berührt.
- **Sonstige Rechte** — Die Lizenz hat keinerlei Einfluss auf die folgenden Rechte:
 - Die Rechte, die jedermann wegen der Schranken des Urheberrechts oder aufgrund gesetzlicher Erlaubnisse zustehen (in einigen Ländern als grundsätzliche Doktrin des **fair use** bekannt);
 - Die **Persönlichkeitsrechte** des Urhebers;
 - Rechte anderer Personen, entweder am Lizenzgegenstand selber oder bezüglich seiner Verwendung, zum Beispiel für **Werbung** oder Privatsphärenschutz.
- **Hinweis** — Bei jeder Nutzung oder Verbreitung müssen Sie anderen alle Lizenzbedingungen mitteilen, die für diesen Inhalt gelten. Am einfachsten ist es, an entsprechender Stelle einen Link auf diese Seite einzubinden.

Acknowledgements

First, I would like to express my gratitude to Prof. Dr. Eberhard Parlow for giving me the opportunity to write this PhD thesis at his institute and letting me be a member of his staff. The many years of work in this motivational environment are much appreciated. Many thanks go to Dr. Roland Vogt for his trust in my abilities in this field of work and great assistance with the experimental set-up. A special thank goes to Prof. Dr. Mathias Rotach for facilitating the start of this thesis during our shared time at MeteoSwiss, the long discussions later at the ETH Zürich, for allowing me to use the three-dimensional LPDM and for being the co-referee in this thesis.

My great appreciation goes to the European Cooperation in Science and Technology (COST) Action ES0603. The financial support for this project by the Swiss State Secretariat for Education and Research (SBF), grant C07.0111, and the Freiwillige Akademische Gesellschaft Basel, is gratefully acknowledged.

Many thanks go to the members of the staff at Meteorology, Climatology and Remote Sensing at the University of Basel: Firstly, Dr. Andres Gartmann for his expertise and patient help with the CFD modelling and the interesting and fruitful collaboration in terms of combining experimental observations and numerical simulation. Günter Bing for his computer support, without which the numerical simulations would not have been possible, Björn Lietzke for countless interesting as well as entertaining discussions as well as Josette Pfefferli-Stocky for her administrative support. A special thank goes to Hans-Rudolf Rüegg for his extensive work on the aerosol sampler as well as his help with the assembly of the micrometeorological towers.

Further, I would like to thank the members of the former department of Bio- and Environmental Meteorology at MeteoSwiss, namely Dr. Regula Gehrig for sharing her ample knowledge on pollen characteristics and their analysis as well as for her help during the experimental campaign. I would like to thank Dr. Bernard Clot for always trusting in my work and his expertise in the field as well as Dr. Andreas Pauling for the interesting discussions on modelling pollen dispersion and emission. The help of Dr. Barbara Pietragalla with the analysis of pollen from several experiments is highly appreciated.

At this point, I express my gratefulness to Benoît Guillod, Ambros Werner and Thomas Meuli for their invaluable help in the field and for making this part of my work very enjoyable. A special thank goes to all the pollen analysts, without whom this work would not have been possible: Marie-José Graber, Christine Salline, Eilin Hickel, Sann Heller and Isabelle Stöckli. Also, my great thank goes to Paul Kunz, who very spontaneously let me use his property and infrastructure to set-up two experimental arrays. Last but not least, I want to express my gratitude to my family and close friends for their support and trust.

However, my greatest thanks are committed to Catherine. Her love, encouragement and patience in hectic moments were essential for this thesis.

Abstract

The occurrence of allergic diseases in western countries increased during the last decades due to greater awareness towards a hygienic lifestyle. The hygiene hypothesis relates the reduced exposure to microbial pollution to an underdevelopment of the immune system, which in turn favours the development of allergies. In order to provide information to affected individuals on adequate pre-emptive measures, numerous studies on the health impact of allergenic pollen focus on their atmospheric abundance and dispersion, including observations and simulation of emission and transport. Prognostic models for the spatial distribution and concentration of different pollen species on a regional scale are operational in many countries in order to identify highly affected regions and allow health offices to announce warnings to the affected population. These models are capable of predicting long-range transport in a full spatial resolution with respect to meteorological conditions. However, the initial abundance of airborne pollen in the models is determined with empirically derived emission parameters, which are mostly based on long-term observation averages with respect to large areas.

Field measurements and modelling work conducted in the framework of this thesis aimed at describing the emission and dispersion characteristics of an isolated natural birch pollen source in the micro-scale, in order to improve the accuracy of the emission part in prognostic pollen transport models. The basic approach was to infer the emission of the pollen source from downwind observations, with respect to meteorological conditions, by reproducing the observed pollen dispersion with numerical simulations. Birch pollen are used, because they are among the most important aeroallergens in Europe. In terms of quantifying the absolute pollen emission in specific cases, however, the field observations of pollen concentrations were subject to various difficulties related to sensor uncertainties and non-stationary conditions in the natural environment.

Firstly, the detailed investigation of pollen transport up- and downwind of the isolated source relied on a large array of different instruments. In order to make the observations of birch pollen concentrations comparable among different used instruments, a substantial part of this thesis is dedicated to the description of performance and uncertainty of different pollen sampling methods. Secondly, since naturally emitted pollen are used for tracers, instead of a controlled release of artificial particles, the observed pollen concentration can be biased by natural background concentration, which relates to emission from unknown sources upwind of the experiment site. The windflow directed towards the birch canopy is substantially disturbed by its roughness and, additionally, a certain amount of airborne pollen is filtered by its vegetation elements. Observations of undisturbed concentrations upwind of the windbreak thus fall short of describing the complex pattern of downwind distribution. A computational fluid dynamics model, therefore, is used to simulate Lagrangian-based trajectories of the pollen with respect to the disturbance of the wind field. The results indicate that the portion of background concentration in the observed downwind concentration is largely dependent on effects of accumulation due to deceleration of the wind flow. Deposition within the birch canopy is accounted for in a separate model, which is based on the optical porosity of the windbreak. A combination of the two model approaches allows to eliminate the portion of background concentration from the measured downwind concentrations, providing information on the emissivity of the isolated birch pollen source.

Based on the corrected concentrations downwind of the windbreak, i.e. un-biased by background concentration, a method of estimating the source strength of the isolated pollen source with a Lagrangian particle model is assessed.

Contents

List of Figures	v
List of Tables	vii
List of Symbols	viii
List of Abbreviations	xi
1 Introduction	1
1.1 Preface	1
1.2 Objectives	1
1.3 State of current research	2
1.3.1 Observations of pollen release	2
1.3.2 Observations of pollen dispersion	3
1.3.3 Modelling of pollen dispersion	3
1.3.4 Modelling pollen transport across a windbreak	4
1.3.5 Emission parameterisation	5
1.4 Structure	6
Experiment design and methods	6
Observational data	6
Performance of blunt volumetric aerosol samplers	6
Transport of background pollen concentration across a windbreak	6
Estimation of emission using a three-dimensional stochastic Lagrangian dispersion model	6
2 Experimental design and methods	8
2.1 Introduction	8
2.2 Experiment location	8
2.3 Isolated source	9
2.4 Instrumentation	10
2.4.1 Meteorological sensors	10
2.4.2 Aerosol samplers	11
Hirst-type pollen traps	11
Air-O-Cell pollen trap	12

3	Observational data	13
3.1	Introduction	13
3.2	Meteorological conditions	13
	Atmospheric conditions	13
	Wind conditions	13
3.3	Turbulence characteristics up- and downwind of the windbreak	14
3.4	Atmospheric pollen concentration	19
4	Performance of blunt volumetric aerosol samplers	20
4.1	Introduction	20
4.2	Aspiration efficiency of blunt samplers at different orientations	20
4.3	Particles in a non-Stokesian regime	23
4.4	Correction of vertically oriented Air-O-Cell samplers	25
P1	Introduction	26
P1	Materials and Methods	27
P1	Pollen sampling methods	27
P1	Sampler intercomparison experiment	27
P1	Post-processing	28
P1	Overview on the sampler agreement	29
P1	Quantification of the error induced by vertical orientation	29
P1	Aspiration characteristics of blunt samplers at different orientations	30
P1	An alternative linear correction for vertical aspiration using wind velocity	31
P1	Results	31
P1	Performance of the physically based aspiration model	31
P1	Performance of the linear correction model	33
P1	Conclusions	33
5	Transport of background pollen concentration across a natural windbreak	35
5.1	Introduction	35
5.2	Modelling and observations of pollen transport through a natural windbreak	35
P2	Introduction	36
P2	Material and Methods	37
P2	Experiment site	37
P2	Instrumentation	37
P2	Pollen transport across a windbreak	39
P2	Windbreak transmissivity σ_p	40
P2	Wind field effect ω	42
P2	CFD model	42

P2 Lagrangian particle dispersion modelling	44
P2 CFD set-up	45
P2 Results	48
P2 Pollen transmissivity of the canopy	48
P2 Results of numerical simulation	49
P2 Validation of modelled actual pollen concentrations	50
P2 Sensitivity to non-stationary conditions	52
P2 Parameterisation of CFD-based pollen transport	54
P2 Conclusions	57
P2 Appendix A Effect of wind velocity on pollen dispersion	62
5.3 Set-up of the source characteristics in the CFD model	64
5.4 Estimating background concentration based on spatial uniformity	64
6 On the estimation of pollen emission using a Lagrangian dispersion model	67
6.1 Introduction	67
6.2 The LPDM model	67
6.3 Assessment of the approach	67
7 Summary and conclusions	70
Bibliography	73
Appendix A Pollen concentration in high elevations	78
A.1 Methods	78
A.2 Observations	79
Appendix B Diurnal course of pollen concentrations	80
Appendix C Perspective correction of the optical porosity profile	81
Appendix D Stepwise pollen dispersal across a windbreak	82

List of Figures

1.1	Eulerian-Eulerian simulation of maize pollen concentration	4
1.2	Lagrangian-Eulerian simulation of particle distribution around a windbreak . . .	5
2.1	Aerial view of the experiment location with observed wind directions.	9
2.2	Lateral distribution of potential source strength	10
2.3	Burkard and composition of AOC sensor	12
3.1	Radiation, air temperature and humidity during the experimental period	14
3.2	Diurnal course of wind velocity and wind direction during the experimental period	15
3.3	Relation of wind direction to atmospheric stability	16
3.4	Vertical profiles of turbulence intensity and the turbulent kinematic heat flux up- and downwind of the vegetation canopy in the case of normal approach and neutral to unstable conditions	17
3.5	Profiles of wind velocity and turbulent kinetic energy under neutral conditions .	18
3.6	Course of uncorrected pollen concentrations at 2 m above the ground	19
4.1	Streamline patterns in the case of anisokinetic and isokinetic sampling	21
4.2	Aspirating thin-walled sampler at an angle to the freestream	22
P1-1	Satellite images of the intercomparison experiment location	28
P1-2	Set-up of the intercomparison experiment	28
P1-3	Lateral pollen deposition on the Burkard sampling slide	29
P1-4	Agreement of 1-h pollen concentrations measured with Burkard and AOC samplers	30
P1-5	Difference of vertically and horizontally oriented AOC samplers as function of the ratio of wind to aspiration velocity	31
P1-6	Aspiration efficiency of the Burkard sampler as function of wind velocity	32
P1-7	Measured aspiration efficiency as function of the ratio of wind to aspiration velocity	32
P1-8	Corrected 1-h AOC data using the physically based and the linear model	33
P2-1	Satellite images of the experiment location	37
P2-2	Experimental instrument set-up	38
P2-3	View of the north face of the windbreak	41
P2-4	Agreement of modelled and measured wind profiles	45
P2-5	Lateral view of the simulated wind field around the windbreak	46
P2-6	Lateral view of particle distribution	47
P2-7	Modelled pollen field in the case of one source height	48

Figure numbers of journal papers are indicated with P1 or P2, respectively.

P2-8	Pollen transmissivity and porosity of the birch stand	49
P2-9	Modelled field of normalised pollen concentrations around the windbreak for different velocity classes	50
P2-10	Variability of the ratio between measured to modelled pollen concentration . .	51
P2-11	Effect of background pollen concentration profile on downwind concentration pattern	52
P2-12	Influence of non-stationary conditions	53
P2-13	Vertical footprint and virtual emission profile	54
P2-14	Vertically resolved deviation of the parameterisation from model results	56
P2-15	Influence of windbreak width on pollen dispersion	57
P2-A.1	Modelled field of normalised pollen concentrations around the windbreak for all velocity classes	63
5.1	Different approaches of implementing particle release at the point sources . . .	65
5.2	Validation of the uniform concentration approach	66
6.1	Interpolated β_c -corrected longitudinal and lateral downwind pollen concentrations observed at 2 m height	68
6.2	Interpolated modelled longitudinal and lateral downwind pollen concentrations at 2 m height	68
A.1	Rotorod pollen sampler	78
A.2	Birch pollen concentrations in high elevations	79
B.1	Diurnal course of normalised pollen concentration during the experimental period	80
C.1	Perspective correction of the optical porosity	81

List of Tables

2.1	Tower instrumentation	11
P1-1	Precision of different sampler types	29
P1-2	Goodness-of-fit and coefficients of statistical correction models	32
P1-3	Summary of relative bias and relative <i>rmse</i> between uncorrected and corrected AOC and Burkard samplers	33
P2-1	Summary of the used model constants	44
A.2	Timing of tethered ballon ascents	79
D.1	Start and duration of stationary source conditions in the CFD simulations . . .	82

Table numbers of journal papers are indicated with P1 or P2, respectively.

List of Symbols

A	Air-O-Cell pollen sampler
A_o	orifice area
A_p	upwind-projected orifice area
B	Burkard pollen sampler
B_p	upwind-projected width of sampler body
B_w	width of sampler body
b	source separation distance
C_{1-2}, C_{4-5}	$k - \epsilon$ turbulence model parameters
C_d	drag coefficient
C_F	correction function for Burkard data
C_M	pollen emission-meteorology coupling (Sofiev)
C_μ	$k - \epsilon$ dissipation model parameter
c	atmospheric pollen concentration
c_0	undisturbed particle concentration
c_{0u}	uniform undisturbed particle concentration
c_1	particle concentration field downwind of c_0 and c_{0u}
c_{Av}, c_{Ah}	pollen concentration measured with vertical/horizontal AOC sampler
c_B	pollen concentration measured with Burkard sampler
c_e	plant-specific flowering factor
c_i	empirical constant for the time period of turbulent particle influence
c_l	pollen concentration at lower sensor (2 m)
c_{lin}^*, c_{lin}^{**}	linearly corrected pollen concentration
c_m	measured pollen concentration
c_s	simulated pollen concentration
c_{pl}	pollen concentration entering sampler inlet plane
c_u	pollen concentration at upper sensor (18 m)
c_{phys}^*	physically-based corrected pollen concentration
d	particle diameter
d_{ae}	aerodynamic particle diameter
E	aspiration efficiency
E_{90}	aspiration efficiency of vertically oriented blunt sampler
E_{90t}	aspiration efficiency of vertically oriented thin-walled sampler
E_{Av}	aspiration efficiency of vertically oriented Air-O-Cell sampler
E_B	aspiration efficiency of the Burkard sampler
E_c	cell-based pollen emission flux (Sofiev)
E_{mdl}	area-based pollen emission flux (Sofiev)
E_θ	aspiration efficiency at yaw orientations
F	forces of gravity and lift
F_b	portion of birch coverage in a given area
F_e	vertical pollen emission flux (Helbig)
f	body force per unit mass
G	empirical description of bluntness
g_1	empirical scale of inlet dimension
g	acceleration due to gravity
h	height of roughness elements
h_{rel}	relative humidity of air
I	turbulence intensity
K_e	pollen emission-meteorology coupling (Helbig)

k	turbulent kinetic energy
k_w	Weibull shape factor
k'	von Kármán constant
L	Obukhov length
L_t	Lagrangian integral time scale of turbulence
m	meandering factor
n	sample size
n_p	number of particles
n_q	number of sources in a discretised vertical profile
P	porosity
P_v	point of view
p	thermodynamic pressure
p_f	cell-wise flowering probability
p_s, q_s	empirical coefficients for particle shape
Q	strength of point sources in the CFD model
q_p	total annual pollen production
R	ratio of wind velocity and sampling velocity
R_p	part of emitted pollen since begin of season
R_{sd}	shortwave downward radiation
Re_p	Reynolds particle number
\mathcal{R}	random number
r	inlet dimension ratio
r_f	scaling factor for parameterisation of CFD-based pollen dispersion
r_{fi}, r_{fs}	functions for parameterisation of CFD-based pollen dispersion
S	area of pollen emission
S_k	source term for flow turbulence
S_u	source term for flow velocity
S_ϵ	source term for dissipation
St	Stokes number
St_d	Stokes number for turning flow
T	air temperature
T_1, T_2, T_3	Micrometeorological tower installed 20 m upwind, 100 m downwind and 350 m downwind of the birch stand
t	time
U	wind vector
U_c	critical rebound velocity
U_i	model initial velocity
U_s	sampling velocity
u_*	friction velocity
u, v, w	longitudinal, lateral and vertical wind component
V	volume
V_a	volume of air passing the sampler orifice area
V_p	height of neutral perspective
w_f	weighting factor for pollen emission
w_s	longitudinal width of the birch stand
$\overline{w'\theta'_t}$	kinematic turbulent heat flux
x	longitudinal distance
x_{T1}	longitudinal position of the observation tower T_1
Y, y	arbitrary flow variables
z	vertical height above ground
z_d	zero-plane displacement
z_m	height of maximum leaf-area density

z_p	particle release height above ground
z_q	source bin height above ground
z_s	specified height above ground
z_t	characteristic length related to turning of a flow
z_0	roughness length
α	leaf-area density
α_a, α_b	aspect angles
α_m	maximum leaf-area density
α_{1-4}	linear model coefficients
β	impaction efficiency
β_c	windbreak effect
β_d	coefficient of TKE breakdown
β_e	windbreak effect error under assumption of uniform concentration
β_p	transfer coefficient for turbulent energy production
β_1	linear model coefficient
γ	pollen density
γ^*	density of water
δ	characteristic length scale of a body
ϵ	dissipation
ζ	stability index
θ	orientation of pollen sensors
θ_d	wind direction
θ_t	virtual acoustic temperature
κ	optical porosity
κ_{ae}	aerodynamic shape factor
λ	Weibull scale factor
λ_0	Weibull scaling factor
μ	dynamic molecular viscosity of air
ν_t	turbulent viscosity
ρ	air density
ρ_p	particle density
σ_p	pollen transmissivity
σ_w/\bar{u}	normalised turbulence intensity
τ	particle response time
τ_i	time period of turbulent particle influence
τ_d	time scale related to turbulence
ν	$k - \epsilon$ model coefficient
ϕ	discrete virtual emission profile
ϕ_P	discrete probability of virtual emission
ϕ_p	parameterised virtual emission
ω	wind field effect

List of Abbreviations

AOC	Air-O-Cell sampler
CFD	Computational Fluid Dynamics
COST	European Cooperation in Science and Technology
EUPOL	Assessment of Production, Release, Distribution and Health Impact of Allergenic Pollen in Europe
IOP	Intensive Operation Period
LAI	Leaf-Area Index
LES	Large Eddy Simulation
LPDM	Lagrangian Particle Dispersion Model
MICROPOEM	Impact of Micrometeorological Factors on Birch Pollen Emission
MOST	Monin-Obukhov Similarity Theory
NSE	Navier-Stokes Equations
OpenFoam	Open Field Operation and Manipulation
PDF	Probability Density Function
PBL	Planetary Boundary Layer
RMSE	Root Mean Square Error
RANS	Reynolds-Averaged Navier-Stokes
SL	Surface Layer
TKE	Turbulent Kinetic Energy
UTC	Universal Time Coordinated

1 Introduction

1.1 Preface

In western countries, the prevalence of diseases related to aeroallergens increased over the last decades and has reached about 20 percent up to date. Adequate protective and pre-emptive measures require both the reliable assessment of production and release of allergenic pollen species and the forecasting of their atmospheric dispersion. A new generation of pollen forecast models, which are either statistically-based or rely on full physical transport and dispersion modelling, are capable of forecasting pollen concentrations with full spatial coverage (Skjøth et al., 2006; Helbig et al., 2004; Schueler and Schlünzen, 2006; Sofiev et al., 2006a,b; Siljamo et al., 2013). Basically, the central part of these recent pollen forecast models corresponds to traditional air pollution transport and dispersion models (Venkatram and Wyngaard, 1988). The main difference between traditional air pollutants, such as gaseous matter, and pollen consists of the fact that the latter are heavy and thus subject to gravitational forces. The most important shortcoming in recent pollen dispersion systems, however, is the description of the emission, which determines the actual abundance of airborne pollen. This is largely due to the missing knowledge of the physical and biological processes that effect the release of pollen and determine the emission rate, namely turbulent exchange, mean transport and preparedness for release. In order to understand in detail the physical processes governing the pollen emission and derive robust parameterisations to be used in a forecast model, the release and dispersion characteristics of an isolated source need to be described with respect to meteorological factors.

1.2 Objectives

Within the COST Action ES0603 (*EUPOL*), which was dedicated to the assessment of production, release distribution and health impact of allergenic pollen in Europe, one working group focused on pollen production and release and their quantitative description. It included analyses of observational and modelling information in order to identify key characteristics of these processes. From this framework the project MicroPoem emerged as a collaboration of the Federal Office of Meteorology and Climatology MeteoSwiss and the Institute of Meteorology, Climatology and Remote Sensing at the University of Basel. The objectives of the study include three parts:

- I. The main objective is the investigation of pollen production and emission by combining experimental and modelling work in order to quantify the released pollen as function of meteorological factors. Birch trees are used, because their pollen are among the most important allergens in Europe. Micrometeorological analyses focus on reproducing the observed downwind pollen distribution with a local three-dimensional Lagrangian-based stochastic particle dispersion model valid for neutral to convective conditions (Rotach et al., 1996; De Haan and Rotach, 1998). The micrometeorological observations provide the necessary input of turbulence characteristics. In order to identify and understand the processes related to birch pollen emission, a small and isolated stand of birch trees was chosen to obtain a well-defined source. The gained information on the local dispersion from the isolated source and measured concentrations can be used to infer the emission rate of birch trees as function of meteorological conditions. Existing parameterisations of birch pollen emission rely on empirical estimates of the total pollen release of large areas during one season, rather than an independent dynamic source strength with respect to short-term atmospheric conditions. The results of this study help to understand the birch pollen emissivity on a substantially smaller scale, which can be

extrapolated to larger regions for the use in forecast models.

- II. Spatial variations of the pollen concentration are addressed with a large number of aerosol sensors, which required the use of self-built instruments in order to enhance the spatial resolution of the measurements. An analysis of the data collected with these instruments revealed a substantial underestimation of the pollen concentration as function of wind velocity. The present study, therefore, also addresses the uncertainty, performance and correction of aerosol samplers under non-isokinetic conditions, which includes a separate field study. A special focus lies on the performance of blunt samplers at yaw orientations to the mean free stream.
- III. The streamfield of the wind flow towards the birch stand is substantially disturbed around the vegetation canopy due to the mechanical influence of the natural barrier on the fluid. Thus, the birch stand acts both as a pollen source *and* as a windbreak. The wind field disturbance results in a complex distribution of the airborne pollen, which originate from upwind regions, i.e. the background concentration. The spatial variability of background concentration has been underestimated in the process of the experimental design. Thus, it is difficult to distinguish the background part from the emission part in downwind observations. In the present study the distribution of background pollen concentration is addressed with a numerical simulation of Lagrangian-based pollen trajectories in regard of the wind field disturbance. The latter is described by a computational fluid dynamics (CFD) model based on the Reynolds-averaged Navier-Stokes (RANS) method.

1.3 State of current research

Studies focusing on the dispersion of airborne particles have been performed in different fields of research including observations and modelling under natural and artificial environments. In the context of heavy particle dispersion under natural conditions, numerous studies have been motivated by the increasing prevalence of allergic diseases and thus the greater interest in the atmospheric abundance and short- and long-range transport of allergenic pollen. The importance of understanding the processes, which determine pollen transport on a local scale, has increased with the growing adoption of genetically modified (GM) crops and resulting contamination of surrounding areas with their pollen. The protection of adjacent crops from unwanted cross-pollination or the reduction of particle loss is addressed in studies focusing on the effect of natural windbreaks on the atmospheric dispersion due to deceleration of the wind flow and filtering within the canopy. Hence, the current research can be related to purely observational studies focusing on the timing of emission, observational and modelling of the dispersion, emission parameterisation and pollen transport through natural windbreaks.

1.3.1 Observations of pollen release

In the context of diseases due to aeroallergens in Europe, Galán et al. (2001) identified the rainfall in March and air temperature prior to the flowering period as the main factors determining the pollination intensity. Nieddu et al. (1997) investigated the intensity and timing of olive pollination in relation to phenological stages and the influence of meteorological parameters on pollen emission and dispersal. They found a significant positive correlation between pollen concentrations and air temperature and a negative correlation between pollen concentrations and air humidity. These findings are confirmed in the case of birch pollen by Méndez et al. (2005), who measured airborne birch pollen with respect to meteorological variables between 1992 and 2000. A positive correlation between pollen count and both temperature and shortwave downward radiation and a negative

correlation to relative humidity were observed. They conclude that air temperature is the governing factor for flowering onset and intensity. Šaulienė and Veriankaitė (2012) also found that the release of ragweed pollen is a function of air temperature and humidity. Van Hout et al. (2008) performed field experiments including vertical profile measurements to study the diurnal cycle of corn pollen concentration and its relation to meteorological and micrometeorological conditions. The diurnal cycles of pollen concentrations were characterised as uni-modal or bi-modal with peak values during the morning and decreasing values during the afternoon. They conclude that humidity and solar radiation may be important variables that govern the release of pollen. They also found a correlation of high pollen concentration periods to ejection periods in coherent structures within the Canopy Boundary Layer.

1.3.2 Observations of pollen dispersion

In terms of investigating plant reproduction and dispersion Raynor et al. (1970) performed a study on the correlation of meteorological factors to the dispersion and deposition of ragweed pollen released both naturally and artificially. They conclude that the variation of pollen dispersion and deposition rates is regulated not only by meteorological but both biological and meteorological factors. Jarosz et al. (2003, 2005) performed experimental studies on the local dispersion of maize pollen with respect to deposition to the ground. The findings indicate that pollen concentrations decrease rapidly with increasing distance from the source. The high deposition rate indicates that only a small fraction of the emitted pollen is still airborne after a distance of 30 m.

Several studies focus on the pollen transport in high elevations, which is associated to long-range transport. Lavigne et al. (1998) performed a pollen-dispersal experiment aiming at the assessment of gene flow associated with the release of transgenic oilseed rape (Lavigne et al., 1996). They found that 50% of the pollen are deposited within a distance of 1.5 times the plant height and thus only a small amount is contributing to a larger area. These findings are in contrast to the results of Brunet et al. (2004), where observations of maize pollen are used, which correspond rapeseed pollen in terms of their diameter. The presence of viable maize pollen within the Convective Boundary Layer have been investigated as an evidence for long-range transport. Up to a height of more than 1500 m above the ground, pollen concentrations of the order of near-ground concentrations were observed, which indicates substantial mixing of heavy pollen in the Convective Boundary Layer. They also found that maize pollen seem to behave like a gas or small particles, since their settling velocity is small compared to the vertical velocities found in the Convective Boundary Layer. Raynor et al. (1974) have investigated the pollen transport of tree pollen up to heights of 3 km. They found that the vertical distribution of pollen is related to the atmospheric lapse rate. The pattern of airborne pollen concentrations at high elevations in relation to meteorological factors was also studied by Comtois et al. (2000) with respect to different species, including pollen released from trees. The findings confirm the high pollen abundance in high elevations with 130% higher concentrations compared to the values found near the ground and thus identified an aerobiological transport layer at 500 m above ground.

1.3.3 Modelling of pollen dispersion

Recent modelling studies on the pollen dispersion often focused on the transport of maize pollen, because of the increasing interest in cross-pollination by GM crops. In contrast to trees, maize plants are substantially smaller and thus release their pollen near the ground, where wind velocity is generally smaller due to friction. The dispersion of airborne pollen is often simulated using a trajectory-based Lagrangian approach, since it can be extended to complex flow fields. Reynolds (1999, 2000); Wilson (2000); Boehm and Aylor (2005) extended Lagrangian dispersion models for traditional pollutants for the use of heavy particles by including the effect of gravitational set-

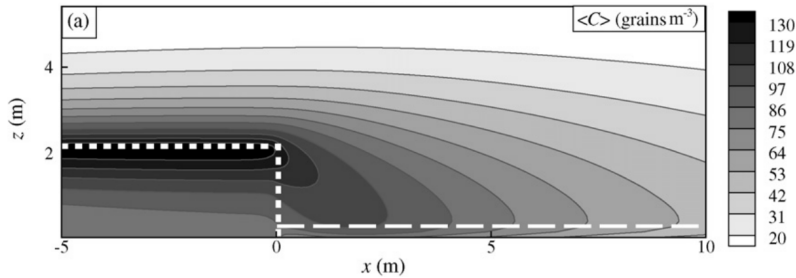


Figure 1.1: Eulerian-Eulerian simulation of maize pollen concentration around the vegetation canopy (dashed white lines). Adapted from: Dupont et al. (2006).

ting, which generally decreases the range of airborne transport due to the higher settling velocity. The skills of Lagrangian simulations of maize pollen dispersion have been investigated based on observations by Aylor and Flesch (2001); Jarosz et al. (2004); Aylor et al. (2006); Arritt et al. (2007); Boehm et al. (2008). The results of the study by Aylor et al. (2006) indicate an average overestimation of the model due to the fact that the natural pollen flux is not stationary and pollen are rather released in gusts (Aylor, 1990). Boehm et al. (2008) have assessed the performance of a Lagrangian simulation with maize pollen measurements in different conditions of atmospheric stratification. They found a good agreement of vertical profiles of modelled and measured data in the case of highly convective conditions with low wind velocities. In the case of stronger turbulence due to shear-stress, i.e. less unstable conditions, the model substantially underestimates the measurements.

An Eulerian-Eulerian approach of maize pollen dispersion is tested by Dupont et al. (2006) and compared to a Lagrangian-based model (Fig. 1.1). The Eulerian simulation agrees well to the Lagrangian model. However, both models underestimate the settling velocity of the heavy particles. Chamecki et al. (2009) validated meso-scale Large Eddy Simulations (LES) of pollen dispersal with experimental observations of artificial tracers and pollen. They conclude that the main parameters governing the shape of the dispersion is the turbulent transport and pollen settling due to the gravitational effect.

1.3.4 Modelling pollen transport across a windbreak

In the case of pollen dispersion from a crop, the wind field is influenced due to the roughness of the canopy, which affects the fluid and particle velocities above. Windbreaks, in contrast, are used to shelter a certain area from wind or airborne matter in the upwind area. They can be artificial or natural (shelterbelts) and porous or non-porous. The impact of windbreaks on the dispersion of particles is characterised mainly by two processes, namely the disturbance of the wind field and particle filtering. While the effect on the wind field is well-documented (Wilson, 1985; McNaughton, 1988; Cleugh, 1998, 2002; Vigiak et al., 2003; Santiago et al., 2007; Rosenfeld et al., 2010), only few modelling studies exist on the specific subject of pollen transport through natural windbreaks, with respect to the disturbance of the wind field and the deposition within the canopy. Bouvet et al. (2007) use a Lagrangian approach to simulate particle trajectories around a shelterbelt of maize (Fig. 1.2). The wind field is driven with the RANS method. However, gravitational settling of the particles (glass beads) and thus inertial effects on their motion are not taken into account. The filtering effect is based on the impaction of Lagrangian-based pollen onto vegetation obstacles. A Lagrangian trajectory-based dispersion is capable of resolving spatially and temporally highly complex situation, which is an advantage in comparison to Eulerian models in the case of local particle dispersion in a disturbed flow field. The effect of spatio-temporal resolution on the model

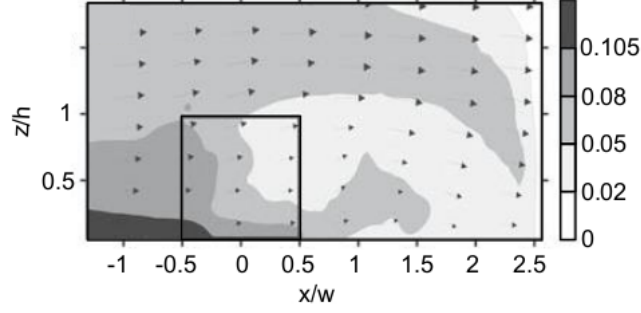


Figure 1.2: Lagrangian trajectory-based particle concentrations downwind of a windbreak (solid lines) normalised with the source strength. The wind field is simulated using a Reynolds-averaged Navier-Stokes approach. The arrows denote vectors of the mean wind field. Adapted from: Bouvet et al. (2007).

detail is indicated by a comparison of Fig. 1.1 and Fig. 1.2. Guo and Maghirang (2012) use an Eulerian-Eulerian model to incorporate windflow and filtering effects in the case of a row of trees.

1.3.5 Emission parameterisation

Helbig et al. (2004); Sofiev et al. (2013) have established parameterisations of birch pollen emission, which rely on the observation of airborne pollen concentrations as function of meteorological factors regardless of the source location. The emission parameterisation by Helbig et al. (2004) incorporates physical as well as biological mechanisms in order to estimate the vertical flux of pollen F_e . It is defined as:

$$F_e = w_f c_e K_e \frac{q_p}{LAI h} u_*, \quad (1.1)$$

where q_p describes the total pollen production during one season in pollen per square meter, LAI is the leaf-area index and h denotes the canopy height. $q_p/(LAI h)$ describes the characteristic concentration. c_e is a plant-specific factor that takes into account that not all plants are flowering at the same time. K_e denotes a correction factor that relates the pollen emission to certain thresholds of meteorological variables, such as air temperature and wind velocity. The friction velocity u_* is used as the characteristic wind velocity and w_f is a weighting factor.

The parameterisation proposed by Sofiev et al. (2013) is based on the principle of temperature sum, which determines the timing of pollination (Linkosalo et al., 2010). The temperature thresholds for the start and the end of the birch pollen season are stable from year to year. The parameterisation provides a release flux of pollen from a certain area during a certain interval via:

$$E_{mdt}(t, i, j) = E_c(t, i, j) F_b(i, j) S(i, j), \quad (1.2)$$

where (i, j) describes one grid cell, $S(i, j)$ is the area in question and t is the time interval. $E_c(t, i, j)$ is the number of pollen emitted from an area of one square meter and $F_b(i, j)$ describes the portion of birch forest in the area S . The temperature sum thresholds are included in E_c :

$$E_c(t, i, j) = \frac{dR_p}{dt} q_p p_f(t, i, j) C_M, \quad (1.3)$$

where R_p is the part of pollen that have been emitted since the start of the season until t . p_f denotes the probability of flowering in a grid cell and C_M accounts for changes in the emission flux due to meteorological conditions.

Both parameterisations [Helbig et al. (2004) and Sofiev et al. (2013)] include the empirically derived constant q_p , which denotes the total of emitted pollen during the entire pollination season from one square meter of birch covered area.

1.4 Structure

The present work is divided into 7 parts, of which each constitutes a section. The content of each part is shortly presented in the following.

In Section 2 the experiment site and used instruments are described. The analyses and results of the obtained observations are presented in the Sections 3 to 6, of which the latter three focus each on one of the main objectives of this study. The results are synthesised and discussed in Section 7.

Experimental design and methods

This part describes the experimental environment and justifies the experiment location. It is situated in a large valley, where a mountain-valley wind system is dominant throughout the field study. The isolated source, consisting of a planted shelterbelt of birch trees, is described in detail with respect to dimension and potential source strength, which has been estimated visually. Also, the used micrometeorological instruments and two different types of bioaerosol sensors are presented. In the case of bioaerosol sensors, the methodology of data collection is described in more detail.

Observational data

In this part the meteorological characteristics at the experiment site during the field study in 2009 are described with focus on phenomena, which are related to the observations described in the following sections. This includes above all an overview on weather conditions by means of radiation data, the description of mean wind and turbulence characteristics with respect to the influence of the birch canopy and an evaluation of uncorrected airborne pollen concentrations measured with two different sensor types.

Performance of blunt aerosol samplers

In this part the correction of the self-built Air-O-Cell samplers used in the present study is addressed. An introduction to the methods of aerosol sampling and the theoretical background of physical principles are provided, which help to understand the problems arising from measurements in a natural environment. The substantial error of the self-built sensors resulting from these problems made a separate field experiment necessary, which was conducted in 2010 during the birch pollen season. The obtained data are used to establish a correction function for vertically oriented AOC samplers, which is compared to existing correction functions for aerosol samplers at yaw orientation to the free stream.

Transport of background pollen concentration across a windbreak

In this part the distribution of the background pollen concentration around the birch stand is investigated. Since the birch canopy has a substantial influence on the streamfield of the oncoming windflow, the dispersion of the transported pollen is more complex than anticipated. Additionally, airborne pollen are filtered at vegetation elements, which also impacts the downwind distribution of pollen concentrations. The set-up and use of a CFD model including trajectory-based Lagrangian simulation of the pollen dispersion are introduced with respect to different approaches of particle injection. The filtering efficiency of the birch canopy is determined separately on the basis of its optical porosity, according to a model developed by Raupach et al. (2001). An introduction to the filtering model provides the theoretical background of this approach as well as a description of the methods used to estimate the porosity of the birch canopy.

Estimation of emission using a three-dimensional stochastic Lagrangian dispersion model

This part consists of the estimation of the birch pollen emission from the isolated source based on the CFD-simulated background concentration and the thereby corrected concentration data downwind of the windbreak. The previous work allows to infer the emission from the birch trees with the assumption $\text{emission} = \text{observed concentration} \times \text{background concentration}$, when the part of background concentration is

eliminated from the measurements. The simulation of a three-dimensional stochastic Lagrangian particle dispersion model (Rotach et al., 1996; De Haan and Rotach, 1998) is presented for the case of unstable atmospheric conditions, i.e. stratifications.

Numbers of figures and tables within journal papers are labelled in relation to their respective sections, e.g. Fig. 1 and Table 1, but they are referred to with the prefix P1 or P2 outside those sections, e.g. Fig. P1-1 and Table P2-1, denoting the first (Section 4.4) and the second paper (Section 5.2), respectively.

2 Experimental design and methods

2.1 Introduction

Studies focusing on the spatial dispersion of airborne particles in a natural environment often use artificial tracers in order to be independent of natural emissions. The artificial release of particles allows to control the source strength, i.e. particle flux, and thus to relate measurements of airborne concentrations directly to the emission, without biasing due to possible background concentration. Yet, the produced particle flux and resulting atmospheric concentrations do not necessarily represent natural conditions. Above all, this is true in the case of natural emission, which involves biological processes that are difficult to simulate. Studies on natural particle emission and dispersion, therefore, need to resort entirely to observations of natural conditions.

The present study aims at inferring the birch pollen emission of an isolated source from downwind concentration measurements. In order to account for the contribution of background concentration to the readings, the concentration of the oncoming pollen stream in the upwind area is observed. This method requires quasi-stationary conditions of wind direction, which conversely determines the orientation of the set-up along the mean wind. In order to facilitate the measurements and fulfil these requirements, the experiment was set in a valley, which is dominated by two wind directions. The experimental study was conducted during the birch pollination season 2009 from 2 to 24 April.

2.2 Experiment location

The site is located at $46^{\circ} 17' 49.8''$ N $6^{\circ} 55' 39.6''$ E in Illarsaz, situated in the Rhone valley in the Southwest of Switzerland (Fig. 2.1). The valley extends in a southeasterly to northwesterly direction with a width of approximately 5.7 km, where it opens to the Lake of Geneva at approximately 11.5 km from the experiment site. To the south, the valley narrows down to a lateral extension of about 1.5 km at 12 km from the experiment site. During daytime a northwesterly wind is dominant with an average velocity of approximately 4 ms^{-1} , which is replaced by wind from southeast during the night with average velocities of around 1 ms^{-1} (see Fig. 2.1). The diurnal course of wind direction is a component of the mountain-valley wind system, which is characterised by a cycle of local daytime upvalley winds and nighttime downvalley winds near the surface (Steinacker, 1984; Weigel et al., 2006). It usually occurs during clear periods with high solar irradiance and weak synoptic influence. Among others, the geometry of a mountain valley effects that the irradiated area corresponds to a much smaller volume of air compared to the situation over adjacent plains. The atmosphere in the valley is, therefore, heated more strongly during daytime and cooling faster during nighttime compared to air above the plains. The resulting temperature gradient between plains and valley causes a cyclic wind system with a diurnal pattern. During daytime, air from the plains flows into the valley and air from the valley flows back into the plains during nighttime. A return branch at higher elevation is sometimes present, flowing in the opposite direction of the surface winds and thus completing the circulation. The mean wind direction during daytime was used to determine the alignment of the instrumental set-up.

The region is characterised by mostly agricultural land-use. Apart from cross-wind vegetation shelterbelts between different crops, the area around the experiment location is undisturbed. To the north, the isolated birch stand is bordered by an area of bare soil (i.e. fallow), which extends to about 475 m in the along-wind direction. The adjacent area to the south extends to approximately 500 m and is divided centrally into a grass field in the east and a potato crop in the west. The height of the grass was around 0.2 m during the experimental campaign. The potato crop had not sprouted during the measurement period and was covered with acrylic sheets. In the lateral

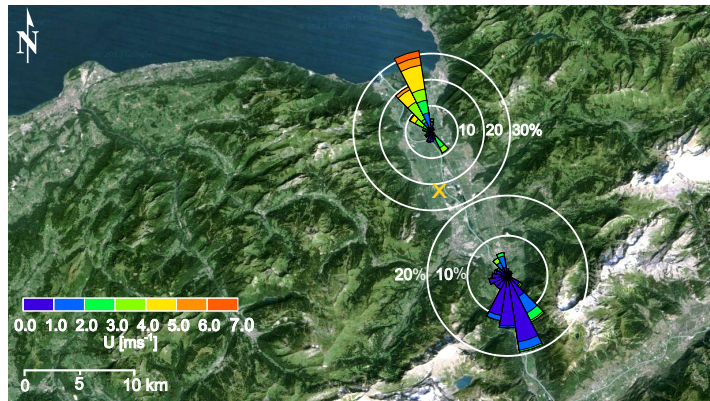


Figure 2.1: Aerial view of the experiment location. Frequency of wind direction and velocities during daytime are shown in the upper inset plot, nighttime conditions are shown in the bottom inset plot. The wind data are obtained at the experiment location (cross).

direction the downwind area is mostly undisturbed.

The closest birch populated tree-lines in the north of the experiment location, i.e. daytime upwind region, is found at a distance of approximately 600 m. For a more detailed view of the experiment site see Section 5.2.

2.3 Isolated source

The pollen source is a planted shelterbelt (or windbreak) of birch trees, which is aligned in the cross-wind direction in order to protect the downwind crops from wind damage and loss of fertilizer due to aerial drift (Wenneker et al., 2005; Mercer, 2009). The birch stand consists of 140 adult birch trees of two different species (*Betula pubescens* and *B. pendula*). Their pollen are nearly identical in terms of their aerodynamic properties. The shelterbelt is 203 m long in the cross-wind direction and 30 m wide in the along-wind direction, with an average height of 19 m. The leading edge of the canopy is exposed to 342° , which corresponds approximately to the daytime mean wind direction. According to the ratio of canopy width to height $w_s/h = 1.6$, the birch stand can be described as a thin windbreak, in contrast to, e.g., small forests, which are considered thick windbreaks in the context of their influence on wind flow. The trunk space has an average height of approximately 5 m, which overlaps with an understorey consisting of dense grass and scrubs with an average height of 1.5 m. For more information on the canopy properties, i.e. its leaf-area density and porosity, see Section 5.2.

A qualitative estimate of the potential emission strength with respect to variations in the cross-wind direction has been performed manually based on the number and size of the catkins of each individual birch tree. The emission potential is classified into four groups, (very weak, weak, average and strong), which are associated with the indices 1 to 4. In order to derive a cross-wind distribution of emission potential in the case of a normally approaching wind flow, the indices of trees in a column in the along-wind direction are cumulated. The resulting distribution is normalised with the average potential emission. It is defined as the index total of the average number trees in a row for the case of average potential emission class only. Figure 2.2 shows that the spatial distribution of birch trees is not regular. In the western part their density is substantially higher and the spacing is more regular than in the western part. This results in a west-east gradient of emission potential. The lowest emission, however, is expected around the middle part of the birch stand, where a group of low-emitting trees and low spatial density effect a dip in the lateral emission potential. Lateral variations of emission affect the cross-wind

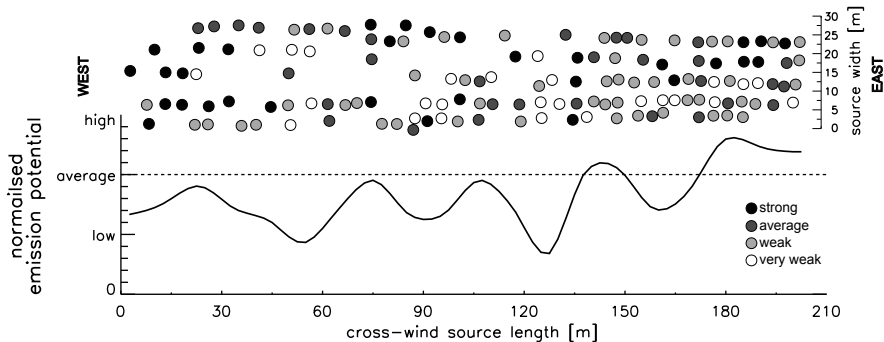


Figure 2.2: Lateral distribution of qualitatively estimated potential source strength. In the upper part the locations of the single birch trees in the stand are indicated with circles. In the lower part the potential source strength is shown as normalised cumulated values in the longitudinal direction, i.e. normal to the windbreak.

distribution in the downwind area. Therefore, the normalised emission potential distribution is taken into account in numerical simulations of the pollen dispersion (Section 6).

2.4 Instrumentation

The set-up aimed at monitoring vertical, along-wind and cross-wind profiles of micrometeorological and airborne aerosol conditions. The orientation of the sensor array was determined according to the mean daytime wind direction, which is oriented approximately normal to the birch stand. In order to be able to observe the greater part of pollen dispersal from the birch stand, the arrangement of the instruments, most importantly their longitudinal and lateral separation, was determined with preliminary simulations of a three-dimensional Lagrangian particle dispersion mode (Rotach et al., 1996; De Haan and Rotach, 1998).

Along the center-line of the experimental area three towers of 18 m height were installed, which were equipped with micrometeorological and aerosol sensors. One tower (T_1) was located in the upwind area of the birch stand in a distance of 20 m in order to measure the vertical profile of background birch pollen concentration and wind flow conditions during daytime upvalley periods. At distances of 100 m and 350 m two towers (T_2 and T_3) were monitoring the corresponding vertical profiles downwind of the pollen source. The arrangement of the towers is shown in detail in Section 4.4 and 5.2. The instruments on the tower T_1 were operational from 2 to 14 April, at T_2 and T_3 the measurements were continued until 23 April. Three cross-wind transects of aerosol measurements near the ground were installed at 100 m, 200 and 350 downwind of the pollen source.

2.4.1 Meteorological sensors

Continuous observations of the meteorological conditions presented in this work were performed above the grass field south of the birch stand at a boom in 2 m height, providing averaged 10 minute data based on a 1 minute resolution. The components of the radiation balance, i.e. short-wave downward (R_{sd}) and upward radiation as well as longwave downward and upward radiation was measured with a CNR1 net radiometer (Kipp & Zonen B.V.) operated without heating or ventilation. Air temperature was monitored using a psychrometer using resistance thermometers for dry (T) and wet temperature. Precipitation and relative humidity h_{rel} was measured with a WXT510 weather transmitter (Vaisala Ltd.).

The turbulence and wind profile up- and downwind of the birch stand was probed with CSAT3

Table 2.1: Tower instrumentation.

instrument	height a.g.	resolution	instrument	height a.g.	resolution
T ₁			T ₂		
CSAT3	2.02 m	20 Hz	CSAT3	2.06 m	20 Hz
CSAT3	9.10 m	20 Hz	CSAT3	4.66 m	20 Hz
CSAT3	17.98 m	20 Hz	CSAT3	9.17 m	20 Hz
Burkard	2 m	2 h	CSAT3	13.64 m	20 Hz
Burkard	18 m	2 h	CSAT3	18.19 m	20 Hz
T ₃			Burkard Sc.	2 m	2 h
CSAT3	2.16 m	10/20 Hz	Burkard Sc.	18 m	2 h
CSAT3	9.16	10/20Hz			
CSAT3	18.15	10/20Hz			
Burkard	2 m	2 h			
Burkard	18 m	2 h			

ultrasonic anemometers (Campbell Scientific Ltd.) with a resolution of 20 Hz. Only for the anemometers mounted on tower T₃ the sampling rate was set from 20 to 10 Hz on 20 April until the end of the experiment. The towers T₁ and T₃, which were located in less disturbed regions (see Section 3.3) were equipped with three ultrasonic anemometers. The tower T₂ located 100 m behind the windbreak was used to monitor the influence of the windbreak on the windflow with a higher spatial resolution and, therefore, was equipped with five ultrasonic anemometers. For the individual sensor heights, see Table 2.1. The calculations of the sensible heat flux and turbulence parameters are based on 30 minute averages.

2.4.2 Aerosol samplers

The concentration of airborne birch pollen concentration was measured with four different types of aerosol samplers, of which all rely on a manual analysis of collected particles. Automatic optical instruments in the stage of evaluation are described by Takahashi et al. (2001); Masanari and Tadashi (2003); Shigeto et al. (2004); Shigetoshi et al. (2005) and Ronneberger (2007). For a detailed description of the sensor alignment and further information on the used methods of pollen analysis, including data correction, see Section 5.2.

Hirst-type pollen traps

Information on vertical and longitudinal profiles of atmospheric birch pollen concentration was obtained with a total of eight aerosol sensors mounted in heights of 2 m and 18 m at all three towers. The used Hirst-type (Hirst, 1952) Burkard (Burkard Manufacturing Co. Ltd.) and Burkard Scientific (Sporewatch) pollen traps are widely used in European operational and experimental frameworks (Fig. 2.3 I). The sensor is originally designed to measure the inhalability of particles (Tsai and Vincent, 1993; Lacey and West, 2006) and thereby to be able to describe the pollen concentration with respect to health impact. In order to obtain the absolute atmospheric concentration from the observations, however, the data need to be corrected. The theoretical background of the applied correction method is described in Frenz (1999).

The sampling part of the sensor is mounted on a pivot and uses a wind vane to align the horizontally oriented inlet towards the oncoming stream. The sensor applies the impaction principle, where air aspirated with a velocity of 1.84 ms^{-1} is diverted around an adhesive slide, on which the suspended pollen collide due to their greater inertia. The collected pollen on the slide are manually analysed (Mandrioli et al., 1998). The used analysis method provided a two-hourly resolution of the pollen concentration. For all observations with different types of pollen samplers in the present study, the Burkard trap served as reference.

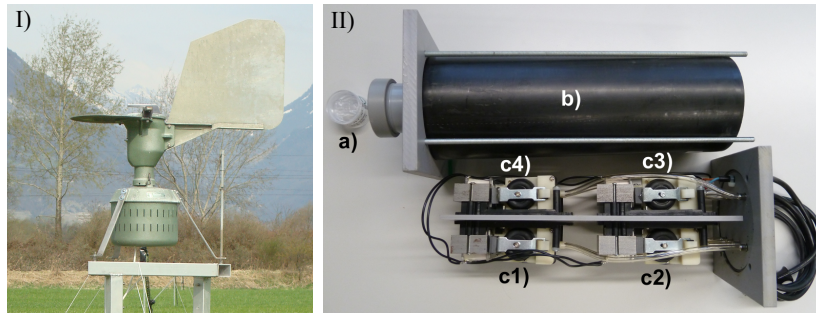


Figure 2.3: I) Burkard sensor mounted at 2m above the ground. II) Composition of the AOC sensor. *a)* AOC cassette *b)* hermetical PVC housing *c1-4)* membrane pumps providing the aspiration of air through the AOC when inserted into the hermetical housing.

Air-O-Cell pollen trap

An array of 18 additional aerosol samplers consisting of three cross-wind transects at 100 m, 200 m and 350 m distance aimed at obtaining a high spatial resolution of the atmospheric pollen distribution in the downwind area of the source with respect to the pollen distribution in the lateral and longitudinal direction. Since the above-mentioned Burkard samplers are very expensive, a pollen sampler was developed, which uses Air-O-Cell (AOC) sampling cassettes (Zefon International) for the pollen collection (Levetin, 2004). Figure 2.3 II shows the composition of the self-built sampler. A set of parallel operating membrane pumps enclosed in a hermetical housing provide the necessary aspiration of air through the inlet dock (shown on the left hand side in the figure) with a velocity of 6.0 ms^{-1} . If an AOC is inserted into the dock, airborne pollen are filtered from the aspirated air within the cassette, according to the impaction principle mentioned above. The sensors were oriented vertically (upward facing) in order to make the measurements independent of wind direction. The AOC array was operated only during intensive operation periods (IOP) in favourable conditions, i.e. clear weather and persistent wind direction, and provided a one-hourly resolution of the pollen concentration.

In order to identify the presence of birch pollen in high elevations, the Planetary Boundary Layer (PBL) was probed in discrete intervals during IOPs using Rotorod pollen collectors mounted on a tethered balloon. Their methods and results are presented in Appendix A.

3 Observational data

3.1 Introduction

In this section observations of (micro)meteorological phenomena and patterns of atmospheric pollen concentrations are analysed, which provides a better understanding of the conditions related to the results presented in the following parts of this work.

3.2 Meteorological conditions

Atmospheric conditions

In order to assess the significance of the obtained pollen measurements under natural conditions, the atmospheric conditions during the experimental period are evaluated with respect to meteorological factors, which reportedly have an impact on pollen emission and airborne concentrations, namely air temperature and humidity (see Section 1.3). A mountain-valley system is expected to establish in clear weather conditions, i.e. when the local conditions are not superimposed by synoptic phenomena.

The course of R_{sd} (Fig. 3.1) shows that the first half of the experimental period is characterised by clear weather conditions, whereas the second half was influenced by intermittent periods of rain and cloud coverage. A continuous clear weather period from the beginning of the campaign until 10 April (including the first and second IOP) is indicated, which resulted in an increasing trend of air temperature. The highest temperature of more than 20°C on 10 April (i.e. the second IOP) are related to a south foehn event. The IOP needed to be interrupted due to the changing wind direction. The foehn event is followed by a two-day period of warm temperatures yet intermittent cloud coverage (including the third IOP). After another two days of clear weather (i.e. the fourth and fifth IOP) a cold front passage from 16 to 18 April, including rainfall, resulted in a substantial temperature decrease. Until the end of the campaign the meteorological conditions were characterised by increasing temperature and cloud coverage, except for a clear weather period on 22 April. During the day the air temperature was above 15°C except for the cold front period. This is well above the threshold of 8°C, which is necessary for the release of birch pollen, according to the ample experience of MeteoSwiss in long-term pollen monitoring. h_{rel} is characterised by a distinct diurnal course with values mostly between 80 and 90% during the night and around 50% during the day. The lowest daytime humidity is observed during the south foehn event, where dry air was mixed down to the valley.

Wind conditions

The experiment location was dominated by a very reliable mountain-valley system during the measurement campaign in terms of persistent wind direction and velocities during the day (top panel in Fig. 3.2). The diurnal course of wind direction (θ_d) is clearly characterised by southerly mountain wind during the night with velocities of around 1 ms⁻¹ and northerly daytime wind from the valley of around 4 ms⁻¹. The transition phase between alternating wind directions is rather short and can be associated to approximately one hour after sunrise (06:00 h) for the change from mountain to valley wind and to approximately two hours before sunset (19:00 h) for the change from valley to mountain wind. The daytime wind direction is more persistent in comparison to the nighttime conditions, which was generally associated with low wind velocities. The southerly wind directions during the day displayed in Fig. 3.2 denote consecutive readings during the south foehn event. Hence, in regard of the two-hourly resolution of the aerosol measurements, the daytime wind

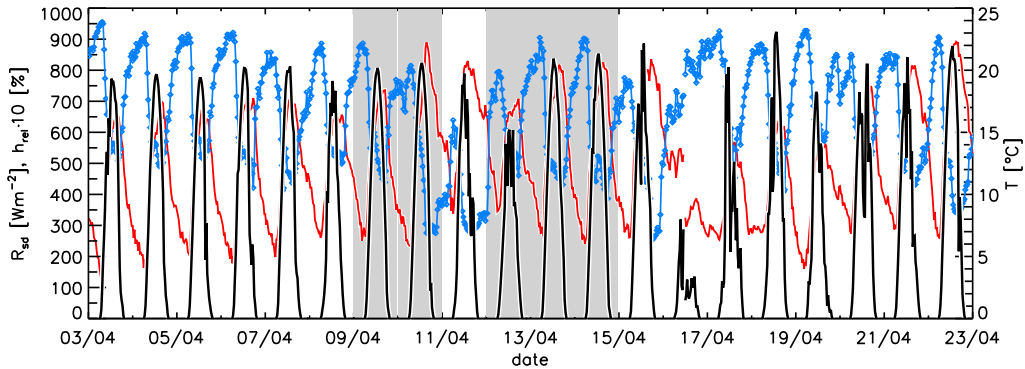


Figure 3.1: 30 minute averaged data of the course of global radiation R_{sd} (black line), dry air temperature T (red line) and relative humidity $h_{rel} \cdot 10$ (blue line) during the experimental period. The shaded areas denote intensive operation periods during favourable weather conditions, when all sensors (including AOCs) were operated.

conditions were in favour of the alignment of the sensor array. The problems of non-stationarity of wind conditions in the case of a higher temporal resolution are addressed in Section 5.2, when the natural conditions are confronted with stationary model conditions.

The influence of the birch canopy on wind velocity is most pronounced between 08:00 h and 22:00 h regarding the difference between upwind and downwind observations in the case of the average diurnal course (see bottom panel in Fig. 3.2). During the northerly wind phase, i.e. when the tower T_2 is in the sheltered downwind area, its measurements indicate lower wind velocities than at T_1 (located upwind). Conversely, during the southerly wind phase, i.e. when T_2 is upwind of the windbreak and T_1 is in the sheltered area, the measurements at T_2 are higher. This effect occurs also in the case of the observations at the tower T_3 . Only during the day the wind velocity is approximately the same as upwind of the birch canopy, because its shelter effect is less effective due to the larger distance and allows the flow to revert to the undisturbed conditions.

3.3 Turbulence characteristics up- and downwind of the wind-break

In the case of a stationary undisturbed flow, the trajectories of transported heavy particles deviate from the fluid streamlines due to gravitational settling, resulting eventually in deposition to the ground. In turbulent conditions, the detachment of particle motion from the fluid is amplified due to the effect of their greater inertia, resulting in stochastic particle dispersal and thus complex concentration distribution. Apart from buoyancy, i.e. thermally induced turbulence in a unstable atmosphere, turbulent atmospheric conditions are produced mechanically by fluid shear stress and friction on roughness elements (Stull, 1988), i.e. vegetation elements in the case of the birch stand. In order to understand the effect of the birch canopy on the wind field and the related pollen dispersion, the turbulence characteristics up- and downwind of the windbreak are investigated with focus on mechanical production turbulence.

Purely mechanically induced turbulence is associated with stable atmospheric stratification, when convective vertical exchange of energy is absent and the PBL is characterised by a uniform potential temperature profile. An estimate of the atmospheric stability within the Surface Layer (SL) is based on the characteristic length L (Obukhov, 1946), which relates mechanical to thermal turbulence. It can be interpreted as a length scale proportional to the vertical height, above which the production of turbulent kinetic energy (TKE) relies more on buoyant processes than

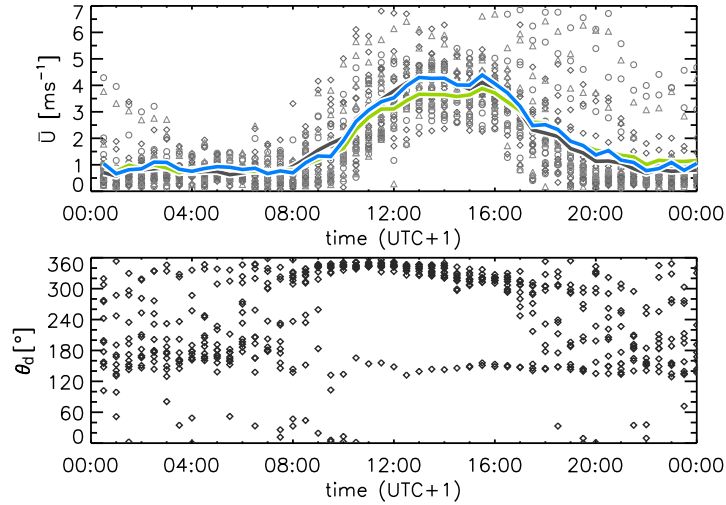


Figure 3.2: *top panel:* 30 minute averaged data of the diurnal course of wind velocity measured at 18 m height at 20 m north of the windbreak (diamonds), 100 m south (circles) and 350 m south of the birch stand (triangles). The lines denote the average diurnal course at 20 m north (black line), 100 m south (green line) and 350 m south of the birch stand (blue line). *bottom panel* 30 minute average data of the diurnal course of wind direction measured at 18 m height 20 m north of the birch stand.

mechanical turbulence. L is expressed as:

$$L = -\frac{u_*^3}{k' \frac{g}{\theta_t} (w'\theta_t')}, \quad (3.1)$$

where k' is the von Kármán constant. It characterises the proportionality of wind shear to height above the surface in the case of neutral stratification. u_* is a scaling parameter for velocity (friction velocity), θ_t denotes the virtual temperature and g is acceleration due to gravity. The term g/θ_t accounts for buoyancy. w' and θ_t' denote the turbulent part of vertical velocity w and θ_t , respectively. The turbulent part of an entity flow is determined using Reynolds decomposition based on instantaneous values via:

$$a' = A - \bar{a}, \quad (3.2)$$

where a' is the turbulent part of any flow A and \bar{a} its mean value in a defined averaging interval. $w'\theta_t'$ thus expresses the kinematic flux of sensible heat, which determines the sign of L . Negative values are associated to unstable conditions, i.e. when the heat flux is directed away from the surface, while positive values are associated to stable conditions, when the flux is directed towards the surface. Equation 3.1 is tied to the Monin-Obukhov Similarity Theory (MOST) for thermally stratified layers, which states that fluxes of momentum, sensible and latent heat vary less than 10% within the SL. It is valid in the case of homogeneous and stationary conditions. A dimensionless parameter of atmospheric stratification is obtained with the stability index ζ , which is defined as:

$$\zeta = \frac{z - z_d}{L}, \quad (3.3)$$

where z is the measuring height above ground and z_d denotes the zero-plane displacement, which is assumed to be $2/3h$. Typically, values of $-0.05 < \zeta < 0.05$ denote neutral conditions. Note that for the analysis of turbulence characteristics the data have been streamline-corrected.

In Fig. 3.3 the relation of wind direction to atmospheric stability is shown in the case of the observations above bare soil north of the birch canopy with respect to day and night conditions. Note that $z_d = 0$ m is assumed, since no vegetation is present. The differentiation between daytime

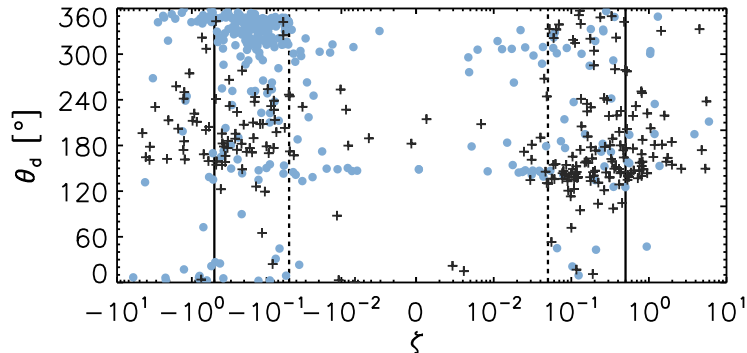


Figure 3.3: Relation of wind direction to the atmospheric stability index ζ during the day (dots) and during the night (plus signs) measured at 2 m above the ground north of the birch stand (T_1). Negative values indicate unstable conditions, positive values indicate stable conditions. The vertical dashed lines denote the transition from neutral ($-0.05 < \zeta < 0.05$) to unstable and stable stratification, respectively. Values of ζ between the solid and dashed vertical lines ($\zeta = \pm 0.5$) are weakly unstable or weakly stable, respectively.

and nighttime is obtained from measurements of solar irradiance, i.e. $R_{sd} > 0 \text{ Wm}^2$ denoting daytime and $R_{sd} \leq 0 \text{ Wm}^2$ denoting nighttime. 30 minute averages of daytime wind direction from the valley are mostly associated to weakly unstable conditions. In fewer cases the stability is neutral, which indicates strong shear stress turbulence due to high wind velocities. Southerly wind during the night is mostly associated to stable conditions. The few cases of unstable conditions during the night and stable conditions during the day occur during the transition phases between upward and downward directed exchange of energy. During the transition periods, the turbulent heat flux is still directed upward shortly after sunset (i.e. positive) due to the warm surface, and, conversely, still directed downward shortly after sunrise (i.e. negative), because the surface is still cooling.

In order to evaluate the production of TKE due to the vegetation elements of the birch canopy, the effect of convective turbulence is assessed by comparing the kinematic heat fluxes up- and downwind of the windbreak. Due to the roughness of the shelterbelt, the MOST condition of homogeneity is not fulfilled for observations in the disturbed downwind region. As an indicator of convection (related to thermal turbulence), the kinematic heat flux $\overline{w'\theta'_t}$ is assessed by comparing vertical up- and downwind profiles. Only cases of northerly wind directions normal to the windbreak are analysed with a threshold of 15° . Figure 3.4 (left column) shows that the turbulent heat flux at 2 m above ground is substantially larger upwind than downwind of the windbreak, although the roughness of the canopy induces mechanical turbulence due to friction on vegetation elements. This discrepancy can not be explained by stronger shear stress due to the higher upwind velocity, since the heat flux at the tower T_3 , where daytime wind velocity is approximately equal (Fig. 3.2), is also significantly smaller. The larger upwind heat flux rather results from stronger convection due to the thermal property of the bare soil. Since the soil is not covered by vegetation (in contrast to the area downwind of the birch stand), the greater part of available energy contributes to the turbulent exchange of heat. Above the vegetated downwind area, in contrast, the sensible heat flux is mitigated due to the partition of available energy into evapotranspiration sensible heat. With increasing height above the ground, the magnitude of $\overline{w'\theta'_t}$ 100 m behind the windbreak substantially increases and approximately equals the upwind condition at $z = 18 \text{ m}$. The vertical variation of the upwind flux is around 1.8% and around 5.5% at 350 m. The slightly larger variation of the measurements at T_3 indicate that the disturbance of the windbreak is still effective to some extent at $x/h = 18.4$. At the closest tower behind the windbreak, however, the vertical variation of the sensible heat is approximately 65.5%, which indicates the substantial disturbance of the wind

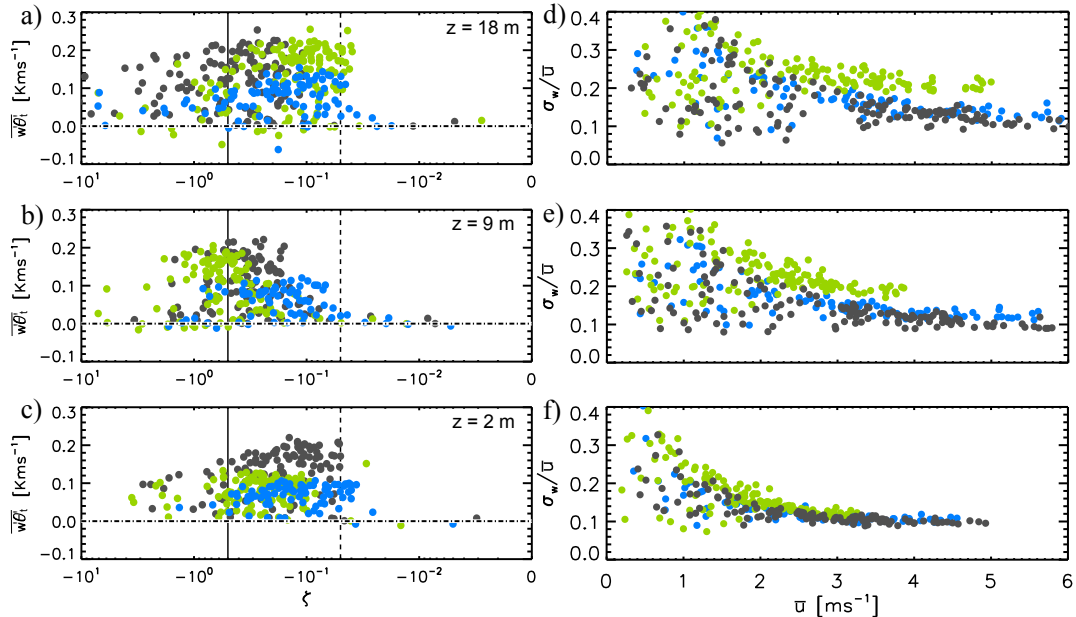


Figure 3.4: *Left column:* Vertical profile of the turbulent kinematic heat flux up- and downwind of the vegetation canopy in the case of northerly normal approach and neutral to unstable conditions identified at the upwind tower T_1 . The vertical dashed line denotes the transition from neutral ($-0.05 < \zeta < 0.05$) to unstable ($\zeta \leq -0.05$) stratification. The vertical solid line denotes the transition from weakly unstable ($-0.5 < \zeta \leq -0.05$) to strongly unstable ($\zeta \leq -0.5$) conditions. *Right column:* Normalised turbulence intensity as function of wind velocity during northerly flow normal to the windbreak. Measurements 20 m upwind (dark grey), 100 m downwind (green) and 350 m downwind (blue) of the birch canopy. Note that in the case of upwind measurements (bare soil) $z_d = 0$ m and in the case of downwind measurements (grass) $z_d = 0.13$ m is assumed. For the exact measuring heights in a-c), respectively d-f), see Table 2.1.

flow that relates to the birch canopy roughness. Furthermore, it can be stated that the produced mechanical turbulence is strongest at the higher levels of the canopy, where the weaker convective process is compensated with shear stress, which results in a heat flux equal to the more convective upwind situation.

An estimate of turbulence intensity is the standard deviation of vertical motion of air (σ_w). In order to compare the characteristics of vertical turbulence in flows of different velocities, i.e. up- and down wind of the birch canopy, it is normalised with the wind velocity \bar{u} . Figure 3.4 (right column) shows that the greatest turbulence intensity σ_w/\bar{u} is observed close behind the windbreak, although thermal effects are substantially smaller. This effect is most pronounced for cases, where $\bar{u} < 2 \text{ ms}^{-1}$ and increases with height above the ground. Hence, the canopy roughness induces stronger vertical turbulence throughout the height of the birch stand, which affects the dispersion of airborne pollen.

As shown above, the mechanical disturbance of wind flow due to the birch canopy roughness is mostly superimposed by buoyant effects due to a thermally stratified SL during northerly approach. The effect of deceleration and purely mechanically produced turbulence on the profile of wind velocity and the resulting production of TKE is, therefore, assessed for cases of neutral stability. In a neutrally stratified PBL, the profile of wind velocity due to friction at the surface and fluid shear stress is determined via (Stull, 1988):

$$U(z) = \frac{u_*}{k'} \ln\left(\frac{z}{z_0}\right), \quad (3.4)$$

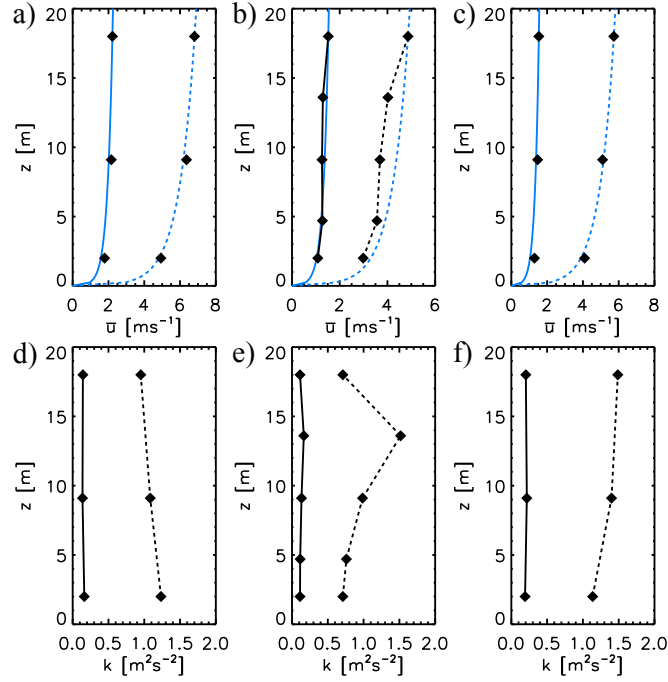


Figure 3.5: *Top row:* Two examples of wind velocity profiles under neutral conditions in the case of normal approach to the windbreak: $\bar{u} = 2 \text{ ms}^{-1}$ and $\bar{u} = 7 \text{ ms}^{-1}$. Blue lines denote the logarithmic wind profile based on the reference measurement at 18 m above the ground. Note that the x-axis is not equally scaled in all plots. *Bottom row:* Corresponding profiles of turbulent kinetic energy (k). Diamonds denote measurements of \bar{u} and TKE at *a,d*) 20 m upwind *b,e*) 100 m downwind *c,f*) 350 m downwind of the birch windbreak.

where $U(z)$ is the wind magnitude as function of height above the ground and z_0 is the roughness length, which can be approximated by $z_0 = 0.1h$. The deviation of the observed wind velocity profile behind the windbreak from the logarithmic profile due to mechanical disturbance is shown in Fig. 3.5 for two different velocity classes. In both cases the measurements upwind and far downwind correspond very well to the theoretical logarithmic case based on the observation at the specific location. 100 m behind the windbreak the velocities are significantly decreased in relation to the theoretical wind profile based on the observation at this specific location. Note that in the case of the higher wind velocity class, the difference to the upwind velocities amounts to about 2 ms^{-1} .

The TKE (k) is defined by (Kaimal and Finnigan, 1994):

$$k = 0.5 \left(\overline{u'^2} + \overline{v'^2} + \overline{w'^2} \right), \quad (3.5)$$

where v denotes the lateral component of wind and is aligned across the mean direction. Hence, the TKE accounts for three-dimensional turbulence, in contrast to the turbulence intensity σ_w mentioned above. Figure 3.5 indicates that the TKE is substantially increased behind the windbreak at around $z/h = 0.7$ due to mechanically induced turbulence. This corresponds to the height of highest leaf-area density in the canopy (see Section 5.2). The influence of turbulence on the pollen dispersion in a disturbed flow is described in Section 5.2.

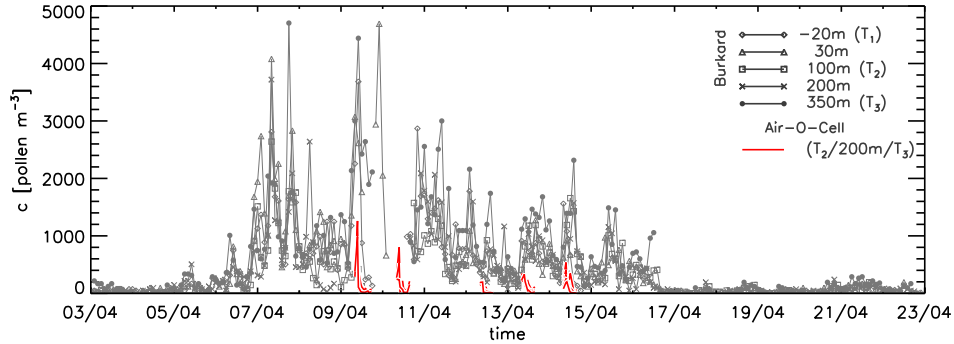


Figure 3.6: Course of pollen concentrations measured 2 m above the ground at different locations up- and downwind of the birch stand. Grey lines denote continuous two-hourly Burkard measurements. Red lines denote discrete one-hourly AOC measurements during intensive operation periods along the center-line of the instrumental array.

3.4 Atmospheric pollen concentration

The start of observations of atmospheric pollen concentrations (c) was timed by a manual evaluation of the catkins in the birch stand with respect to their preparedness to release pollen. Figure 3.6 shows that at the begin of the measurements birch pollen were already present, yet in very low concentrations ($c < 200 \text{ pollen m}^{-3}$). The main part of emission started on 7 April and ended on 16 April. The course of pollen concentrations indicate peaks on 7 April, 9 April and 11 April. The median of the pollen concentration during the main part emission was $412.8 \text{ pollen m}^{-3}$ near the ground and $535.8 \text{ pollen m}^{-3}$ at a height of 18 m above the ground. After the part of intensive emission, the concentration levelled out again at $c < 200 \text{ pollen m}^{-3}$. The data represent the situation during valley and mountain wind periods, i.e. daytime and nighttime. Ogden et al. (1969); Von Wahl and Puls (1989); Jäger (1990); Van Hout et al. (2008) and Mahura et al. (2009) report diurnal courses of pollen concentration, which indicate stronger emission during the day and nearly zero emission during the night for different species, including birch. In the present study, however, the abundance of airborne birch pollen is substantial throughout day- and nighttime and no distinct diurnal pattern is detectable (see Appendix B). Only on average do daytime values slightly exceed nighttime values during the main emission period. This could be related to mixing of deposited pollen into the air due to mechanically induced turbulence. Furthermore, a certain portion of the night concentration could be associated to long-range transport, i.e. pollen, which have been airborne for a long time and eventually settled into the domain.

Since the abundance of airborne pollen in the upwind area for both valley and mountain wind was substantial, the observed birch pollen concentrations at the experiment location are biased by background concentration. In order to be able to determine the pollen emission from the isolated source only, the amount of background concentration in the readings is determined with numerical simulations (see Section 5).

The readings of the AOC pollen traps during IOPs indicate a substantial underestimation of pollen concentrations compared to the Burkard measurements. Since the sensors were facing upward, i.e. normal to the mean flow, the collection efficiency underlay the effects of inertia as function of wind velocity in the case of the heavy birch pollen. A correction of the AOC data in relation to the reference Burkard observations was established on the basis of a separate field experiment using vertically as well as horizontally oriented (i.e. facing the oncoming wind) sensors. The additional field experiment and the correction function are presented in Section 4.4.

4 Performance of blunt volumetric aerosol samplers

4.1 Introduction

The volumetric method of airborne particle observations (e.g. Hirst-type samplers and AOC samplers) relates a quantity of collected pollen to the corresponding volume of air. The air is aspirated mostly with a constant flow rate, which determines the sampled volume in a given time interval. Uncertainties of this method relate to distortion of the flow upwind of the sensor, which is induced by the sensor body opposed to the stream and the discrepancy between aspiration rate and wind velocity. These uncertainties apply for both sensor types used in the present study. In the case of the AOC samplers, additional uncertainties arise from their vertical orientation (see Fig. 3.6).

4.2 Aspiration efficiency of blunt samplers at different orientations

Experimental and theoretical work on the determination of the aspiration efficiency of aerosol samplers are mostly related to thin-walled, tubular inlets facing the freestream, e.g. Badzioch (1959) and Belyaev and Levin (1974). In theory, a infinitely thin-walled sampler has no physical effect on the oncoming freestream in terms of disturbance due to its shape. This idealisation is a starting point to understand the basic principles governing the aspiration of aerosols. In practice, however, the flow pattern upstream of a sampler orifice is much more complex. It is affected by various parameters, such as the orientation θ of the orifice, the aspiration velocity U_s and the characteristic bluntness of the sampler body. Vincent et al. (1986) investigated the physics of thin-walled samplers with respect to their orientation relative to the freestream. Based on his work, Tsai and Vincent (1993) developed a model for blunt sampler types, which is tested in the present study for the specific case of vertical orientation.

In theory, the aspiration efficiency of a sampler is defined by:

$$E = c_{pl}/c, \quad (4.1)$$

where c_{pl} is the particle concentration entering the plane of the sampler inlet and c is the upstream concentration, given that the air and particle velocity distributions are uniform. The aspiration efficiency can be characterised using the following dimensionless parameters:

$$R = \frac{U}{U_s}, \quad (4.2)$$

where U is the freestream velocity and U_s is the sampling or aspiration velocity through the sampling orifice. In the case of idealised thin-walled samplers, $R = 1$ denotes isokinetic sampling, where $E = 1$. The flow directed towards the sampler is not distorted in this case, since the aspiration velocity equals the oncoming freestream (Fig 4.1). If sampling is sub-isokinetic ($R > 1$), the air diverges around the sampler orifice. However, due to their greater inertia, the particles continue their motion into the orifice, resulting in an overestimation of pollen concentration, i.e. $E > 1$. Conversely, if sampling is super-isokinetic ($R < 1$), the fluid streamlines converge towards the sampling orifice, whereas particles tend to pass the orifice, resulting in an underestimation of particle concentrations, i.e. $E < 1$. Since the Burkard and AOC trap both use a fixed aspiration rate (see Section 2.4.2), isokinetic sampling conditions are reached in rare cases only due to the large natural variation of the freestream velocity.

The deviation of particles from fluid streamlines in a distorted flow is related to their inertia. The

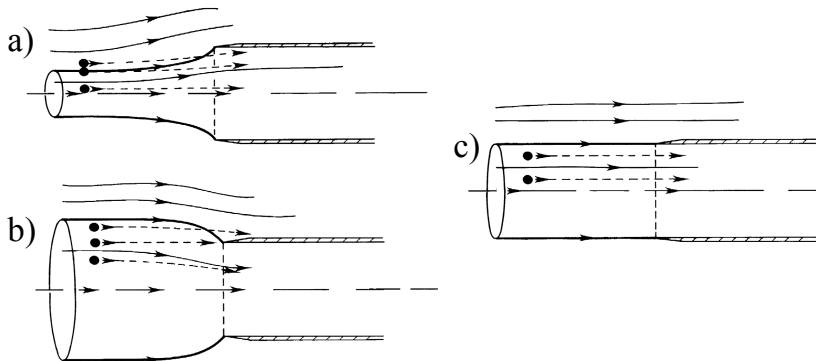


Figure 4.1: Streamline patterns in the case of anisokinetic and isokinetic sampling. *a)* sub-isokinetic ($R > 1$) *b)* super-isokinetic ($R < 1$) *c)* isokinetic ($R = 1$). The dots denote particles, dashed arrow-lines denote their trajectories and solid arrow-lines denote fluid streamlines. Adapted after: Vincent (2007).

inertially-dominated behaviour of particles in a turbulent flow is described by the dimensionless Stokes number, which is defined as

$$St = \frac{\tau U}{\delta}, \quad (4.3)$$

where δ is a characteristic length scale and τ denotes the response time of a particle to perturbation. In combination with the flow (and particle) velocity, τU describes the stopping distance of a particle. It can be interpreted as the distance, over which a moving particle would continue its motion due to its inertia, if the flow velocity abruptly becomes zero ms^{-1} . The Stokes number thus denotes the ratio of the stopping distance of the particle to a characteristic length, e.g. the width of the sampling orifice. Small values of St indicate that the particles tend to follow the fluid trajectories, while large values indicate a separation of particle motion from the fluid motion. The response time of the particle to perturbation in a Stokesian regime, i.e. in a laminar flow, is defined as:

$$\tau = \frac{\gamma^* d_{ae}^2}{18\mu}, \quad (4.4)$$

where μ is the dynamic molecular viscosity of air and d_{ae} is the aerodynamic particle diameter. It characterises a sphere with the density equivalent to water ($\gamma^* = 1 \text{ gcm}^{-3}$), which has the same settling velocity as the particle in question. According to Bates et al. (1966) it can be expressed as:

$$d_{ae} = d \left(\frac{\rho_p}{\gamma^* \kappa_{ae}} \right)^{1/2}, \quad (4.5)$$

where d is the particle diameter, ρ_p denotes the particle density and κ_{ae} denotes an aerodynamic shape factor. For spherical particles (such as birch pollen), $\kappa_{ae} = 1$ is used. In this form, d_{ae} is valid only in a laminar (i.e. Stokesian) flow regime.

With the consideration of sub- and super-isokinetic sampling of a thin-walled sampler (as function of R), Eq. 4.1 can be extended to:

$$E = \frac{c_{pl}}{c} = 1 + \beta(R - 1), \quad (4.6)$$

where β is the impaction efficiency, defined as the ratio between the number of particles impacting onto the virtual plane between the limiting trajectories and the number of particles impacting onto the plane of the sampling orifice. A robust empirical expression for β is:

$$\beta = 1 - \frac{1}{1 + GSt}, \quad (4.7)$$

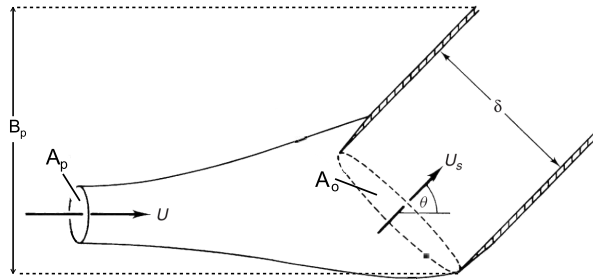


Figure 4.2: Aspirating thin-walled sampler at an angle to the freestream. A_o denotes the orifice area, A_p denotes the upwind-projected area of the orifice between the limiting streamlines. U_s denotes sampling velocity. B_p denotes the upwind projected length of the sampler body. Adapted after: Vincent (2007).

where G is an empirical coefficient, which was investigated by Belyaev and Levin (1974) and Paik and Vincent (2002). Following Eq. 4.6, the aspiration efficiency of thin-walled samplers in moving air and with orientation up to $\theta = 90^\circ$ can be expressed by an impaction model, which in similar form was used by Belyaev and Levin (1974); Durham and Lundgren (1980); Vincent et al. (1986); Wiener et al. (1988); Lipatov et al. (1988); Vincent (1989); Grinshpun and Lipatov (1990); Hangal and Willeke (1990*a,b*); Grinshpun et al. (1994); Vincent (2007):

$$E_\theta = \frac{c}{c_0} = 1 + \beta_\theta(R \cos \theta - 1), \quad (4.8)$$

where θ is the angle between the horizontal plane and the plane normal to the sampling orifice. In Vincent et al. (1986), a new Stokes number is introduced, which relates to particle motion in a turning airflow due to yaw sampler orientations. Since the present work focuses on the aspiration characteristics of upward facing samplers, only the special case of $\theta = 90^\circ$ is considered here. For detailed information on semi-empirical aspiration models for thin-walled samplers based on impaction for angles up to $\theta < 90^\circ$ see Vincent (1987, 1989, 2007) and Tsai and Vincent (1993). The new Stokes St_d number is expressed as the ratio of the particle response time τ to time scale τ_d , which relates to the flow distortion, i.e. convergence/divergence and turning of the flow. The first effect is dependent on the bluntness of the sampler. It is important to understand that the area projected upstream by the sampler body (B_p) increases with θ (Lundgren et al. (1978), Fig. 4.2). Hence, for the case of vertical orientation, the bluntness is maximised and determined by the entire length of the sampler. The second effect is dependent on the aspiration velocity, namely the ability of turning the horizontal freestream. A characteristic length z_t is introduced, which relates to the turning of the flow with:

$$\tau_d = \frac{z_t}{U} \quad (4.9)$$

The length scale z_t may be estimated using the aspiration velocity U_s in the expression:

$$4\pi z_t^2 U = \frac{\pi \delta^2 U_s}{4}, \quad (4.10)$$

assuming that z_t is the distance from the sampling inlet, where the aspiration velocity is equal to the freestream velocity component parallel to the plane of the sampling inlet. This yields $z_t = \delta$ and, therefore, Eq. 4.9 and 4.10 can be summarised to:

$$\tau_d = \frac{\delta}{4R^{1/2}U}, \quad (4.11)$$

so that the new Stokes number related to the turning effect can be expressed with Eq. 4.9 and 4.11 as:

$$St_d = St \left(4R^{1/2} \right) \quad (4.12)$$

Together with Eq. 4.8, this provides a model for vertical sampling using thin-walled probes:

$$E_{90t} = \frac{1}{1 + 4G_{90}StR^{1/2}} \quad (4.13)$$

Vincent et al. (1986) found a good agreement of the model with experimental data for a constant value $G = 2.1$ for $\theta = 0^\circ$ up to 90° .

The models mentioned so far still represent a rather idealised case, however, since they do not take into account flow distortion around the sampler inlet due to the sampler body, i.e. its bluntness. In the specific context of monitoring atmospheric pollen concentration this problem stands out, since blunt samplers are very common. On the basis of the model for thin-walled samplers by (Vincent et al., 1986), a modification for the range of blunt samplers at orientation $\theta = 90^\circ$ and 180° was developed by Tsai and Vincent (1993). They introduced a characteristic number, which describes the bluntness of the sampler inlet:

$$r = \frac{\delta}{B_w}, \quad (4.14)$$

where B_w is the width of the sampler body. Thus, a small r accounts for a large bluntness, which can result in a divergent air flow, even if sampling is isokinetic. In the case of large Stokes numbers of the sampled particles, this would lead to an overestimation of concentration, due to the inertial effects discussed earlier. The aspiration model for blunt samplers with orientation $\theta = 90^\circ$, i.e. AOC samplers, is based on Eq. 4.13 and has the form

$$E_{90} = \frac{1}{1 + 4G_{90}r^{g_1}StR^{1/2}}, \quad (4.15)$$

where G_{90} and g_1 are both empirical coefficients. From experimental human head studies (Ogden and Birkett, 1977; Armbruster and Breuer, 1982) and on the basis of the thin-walled model by Vincent et al. (1986), Tsai and Vincent (1993) obtained an agreement of the corrected data of $R^2 = 0.61$ for $G_{90} = 2.21$ and $g_1 = -0.5$, where the term $G_{90}r^{g_1}$ accounts for the bluntness and the inlet dimension ratio r .

The physically-based correction function shown in Eq. 4.15 is tested with birch pollen observations obtained with AOC samplers in comparison to Burkard sensors, since the sampling orifice of the Burkard sampler is horizontal and facing the oncoming wind (Section 4.4). However, streamline divergence due to its wide body results in an uncertainty in addition to errors related to anisokinetic sampling. Therefore, also the measured Burkard data need to be corrected in order to represent the atmospheric pollen concentration. On the basis of empirical data by Ogden et al. (1974), Frenz (1999) determined the aspiration efficiency of the Burkard sensor with respect to different pollen sizes and wind conditions. For *Ambrosia* pollen, which are similar to birch pollen in terms of mass and shape, the efficiency of the Burkard traps is defined as:

$$E_B = 2.088 U^2 - 17.977 U + 99.959, \quad (4.16)$$

where E_B denotes the sampling efficiency in percent. Based on Eq. 4.16, the correction factor $C_F = 1/(E/100)$ is defined, which accounts for the influence of wind velocity on the sampling efficiency and thus compensates over- or underestimation of sampled pollen.

4.3 Particles in a non-Stokesian regime

As mentioned above, the expression of τ (Eq. 4.4) is valid in the Stokesian regime only, where the flow is laminar. This applies when the particle Reynolds number Re_p (Eq. 4.17) is low. A common threshold for the Stokesian regime is $Re_p < 1$ (Vincent, 2007).

$$Re_p = \frac{dU\rho}{\mu}, \quad (4.17)$$

where ρ is the density of air. If the particle motion is influenced by turbulent fluctuations of the fluid, the particle Reynolds number increases ($Re_p > 1$). The Stokes law describes the influence of the drag force on particles in motion. Stöber (1972); Raabe (1976) suggested the limitation of Eq. 4.5 to small particle Reynolds numbers. Note that in the case of birch pollen, assuming $d = 22 \mu\text{m}$ and $\gamma = 800 \text{ kgm}^{-3}$, Re_p equals 1 at $U = 0.75 \text{ ms}^{-1}$ already. Typical wind daytime velocities during the experiment reached about 4 ms^{-1} (Fig. 3.2), so that the general daytime particle flow condition can be described as mainly non-Stokesian. In Eq. 4.15, however, the Stokes number is described by τ , which is valid in Stokesian conditions only. This can explain the discrepancy of observations and the function shown in Fig. P1-7 in the journal paper P1 (Section 4.4) and the need for the establishment of a correction based on own observations.

4.4 Correction of vertically oriented Air-O-Cell samplers

Michel, D., Rotach, M.W., Gehrig, R. Vogt, R. (2012): *On the efficiency and correction of vertically oriented blunt bioaerosol samplers in moving air*, Int. J. of Biometeorol. **56** (6), pp. 1113-1121, DOI: 10.1007/s00484-012-0526-x.

On the efficiency and correction of vertically oriented blunt bioaerosol samplers in moving air

Dominik Michel · Mathias W. Rotach · Regula Gehrig · Roland Vogt

Received: 9 May 2011 / Revised: 30 January 2012 / Accepted: 30 January 2012
© ISB 2012

Abstract The aspiration efficiency of vertical and wind-oriented Air-O-Cell samplers was investigated in a field study using the pollen of hazel, sweet chestnut and birch. Collected pollen numbers were compared to measurements of a Hirst-type Burkard spore trap. The discrepancy between pollen counts is substantial in the case of vertical orientation. The results indicate a strong influence of wind velocity and inlet orientation relative to the freestream on the aspiration efficiency. Various studies reported on inertial effects on aerosol motion as function of wind velocity. The measurements were compared to a physically based model for the limited case of vertical blunt samplers. Additionally, a simple linear model based on pollen counts and wind velocity was developed. Both correction models notably reduce the error of vertically oriented samplers, whereas only the physically based model can be used on independent datasets. The study also addressed the precision error of the instruments used, which was substantial for both sampler types.

Keywords Burkard sampler · Air-O-Cell sampler · Orifice orientation · Birch pollen · Field measurement

D. Michel (✉) · R. Vogt
Meteorology, Climatology and Remote Sensing,
University of Basel,
Basel, Switzerland
e-mail: dominik.michel@unibas.ch

D. Michel · M. W. Rotach · R. Gehrig
Federal Office of Meteorology and Climatology MeteoSwiss,
Zurich, Switzerland

M. W. Rotach
Institute of Meteorology and Geophysics, University of Innsbruck,
Innsbruck, Austria

Introduction

Experimental investigation of local aerosol dispersion requires both spatially and temporally detailed information on their concentrations. Spatial resolution is often limited by the availability of instruments. Therefore, different instrument types may be used in order to increase the instrumental set-up, i.e., spatial information. The comparability of different aerosol sensors, however, presumes a knowledge of their aspiration characteristics. The present study was motivated by a field experiment (Michel et al. 2010) in which different bioaerosol samplers were used to sample birch pollen (22 μm diameter). The measurements indicate a substantial discrepancy between wind-oriented Hirst-type (Hirst 1952) Burkard samplers and vertically oriented Air-O-Cell samplers. The latter were facing upwards to make the measurements independent of wind direction. In the present study, field intercomparison of Burkard and Air-O-Cell samplers was carried out during the birch pollen season in 2010. The Air-O-Cells were oriented vertically as well as horizontally. The effect of orifice orientation on the aspiration efficiency (i.e., the ratio of sampled aerosols to the aerosol number in the considered volume of air upstream of the orifice) is well-known (Ogden et al. 1974). Aspiration is related to inertial effects on particle motion. As the angle between the orifice and the freestream increases, the behavior of the flow approaching a sampler is progressively complicated, and the aspiration efficiency decreases dramatically (Lundgren et al. 1978; Vincent et al. 1986). Thus, in the case of vertically oriented blunt samplers, which represents most pollen samplers used in the field (Levetin 2004), a correction of the measured data is indispensable. It would be of great benefit to bioaerosol-related research (e.g., the advancing field of aeroallergenic studies), if corrections of measured data were performed at experimental as well as

operational stations. The impaction efficiency of Air-O-Cell and Burkard samplers (i.e., the ratio of sampled aerosols to the number of aspirated aerosols) was investigated under laboratory conditions by Aizenberg et al. (2000). Their results indicate a good agreement of the Air-O-Cell with the Burkard sampler for small fungal and bacterial aerosols ($< 3.5 \mu\text{m}$). The aspiration efficiency of the Burkard sampler was determined under laboratory conditions with respect to wind velocity and pollen size by Hirst (1952) and Ogden et al. (1974). For Ambrosia pollen, which have a similar size as birch pollen ($20 \mu\text{m}$), Ogden et al. (1974) found an efficiency declining to 60% for wind velocities $< 5 \text{ms}^{-1}$. A physically based semi-empirical model accounting for the effects of vertical oriented sampler inlets, wind velocity and bluntness of the sampler body on aerosol motion has been developed by Tsai and Vincent (1993). In the present work, this aspiration model was verified with the measured data of the sampler intercomparison. The deviation of vertical Air-O-Cells from Burkard measurements could be reduced notably. Additionally, an alternative linear correction model was constructed on the basis of pollen counts and wind velocity. The linear correction yields a better agreement of Air-O-Cells with the Burkard sampler, yet it cannot be transferred to independent datasets.

Apart from aspiration efficiency, uncertainties are also induced by the manual sample analysis, which is still the standard at most operational pollen observation sites. Large errors may occur when aerosol deposition on the impaction area is inhomogeneous. In the present study, this applies only to the Burkard sampler, since the Air-O-Cell counting covers the entire impaction area. Laboratory and field studies (Comtois et al. 1999; Aizenberg et al. 2000; Gottardini et al. 2009) on pollen density distribution on the slide of volumetric pollen samplers showed that the distribution is mostly inhomogeneous and dependent on pollen size.

Materials and Methods

Pollen sampling methods

The instrument set-up included two different types of bio-aerosol samplers, which both use the impaction principle, where aerosols impinge on a sampling substrate as an effect of greater inertia than that of air, accelerated by aspiration. The Air-O-Cell (A) sampler (Zefon International, <http://www.zefon.com>; Levetin 2004) is a disposable cylindrical cassette, which includes a sampling substrate-coated glass slide. Its orifice tapers to a slit of $14.4 \text{mm} \times 1 \text{mm}$. The instrument can be mounted wind-oriented (horizontally) when the wind direction is persistent, or facing upwards (vertically), making the measurements independent of wind direction. In the present study both orientations were used.

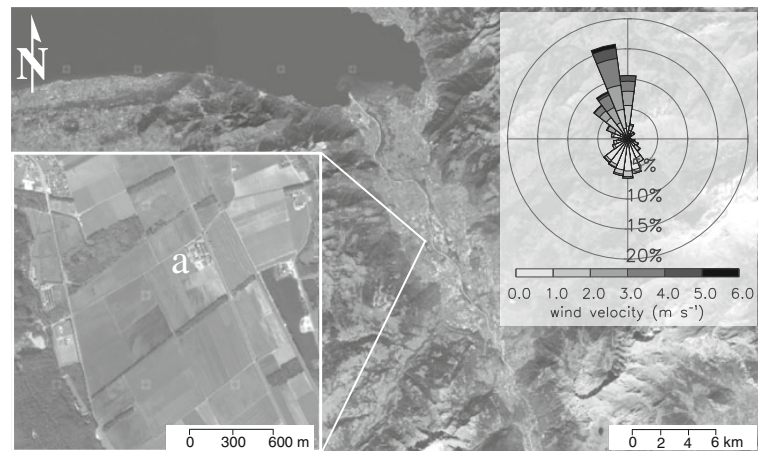
The Air-O-Cell cassette needs to be connected to a pump, which is capable of producing a sampling rate of 15lmin^{-1} . The pump provided by Zefon is not suitable for experimental outdoor use and very costly if a larger array of A samplers is to be equipped. Therefore, an alternative self-constructed aspiration system consisting of parallel membrane pumps was attached to the cassettes conferring a cylindrical shape on the total A sampler (see Fig. 2). The system provides a sampling rate of 18.5lmin^{-1} , which exceeds the factory-recommended minimal sampling rate. A larger sampling rate increases the range of sampled particles towards lighter particles. The temporal resolution is determined by the cassette exposure. The sampling rate was monitored in situ using a thermal gasflowmeter (red-y smart, Vögtlin Instruments, Aesch, Switzerland). The exposure time was 45 min, then the cassettes were replaced. The collected pollen numbers were extrapolated to obtain a 1-h resolution. The pollen counting procedure covered the entire impaction area.

The Burkard (B) sampler (Burkard Manufacturing, Rickmansworth, UK) is a wind-oriented instrument with a $2 \text{mm} \times 14 \text{mm}$ slit orifice (Mandrioli et al. 1998). The sampling rate is 10lmin^{-1} . Particles are collected on an adhesive sampling tape mounted on a rotating cylinder, which provides a continuous 7-day information on pollen concentration. The temporal resolution depends on the analysis method. In the present study, a 1-h resolution was obtained. Four or five longitudinal counting sweeps were performed across the impaction area, which yields a coverage of 20.5 and 25.7%, respectively. The total pollen number was extrapolated to the entire impaction area. The body shape (i.e., bluntness) is similar to that of the human head, since the B sampler was designed to measure inhalable aerosols rather than their atmospheric concentration. The B sampler is used commonly in European bioaerosol monitoring networks. In the present study, therefore, their measurements are taken as a reference.

Sampler intercomparison experiment

The sampler intercomparison was conducted in Illarsaz, Switzerland during the emission period of birch (*Betula*) pollen from 5–23 April 2010. The study site (Fig. 1) was located in a valley where birch is common. The region is dominated by a plains-mountain wind system with persistent wind conditions (mean wind direction 350° during daytime and southerly wind during the night). Knowledge of the predominant daytime wind direction was used to align the instrument set-up normal to the mean wind direction. A small spatial instrument separation ($< 10 \text{m}$) was chosen to minimize sampling discrepancies due to inhomogeneities of the atmospheric pollen distribution (Fig. 2). In the case of

Fig. 1 Satellite images of the experiment locations in Illarsaz, Switzerland (*top left* Lake of Geneva). *Inset, lower left* Location of intercomparison experiment 2010 (*a*). *Inset, top right* The frequency of wind direction and velocity measured at *a*. Federal Office of Topography swisstopo (<http://www.swisstopo.admin.ch/internet/swisstopo/en/home.html>)



low concentrations, however, atmospheric inhomogeneities may induce large relative sampling errors of 1-h averages. The measuring height was 2 m above the ground.

The intercomparison set-up consisted of two B samplers and four A samplers; two A samplers were oriented horizontally (A_h , where the subscript refers to orientation), facing the mean wind. Two A samplers were oriented vertically (A_v), facing upwards. This set-up was chosen in order to assess the difference between the A and B sampler when both are mounted such that the orifice faces the mean wind direction, as well as the impact of vertical orientation of the A sampler. Simultaneously, a USA-1 ultrasonic anemometer (METEK, Elmshor, Germany, 10 Hz) was mounted at 2 m above the ground and 21 m upwind of the bioaerosol samplers to monitor the wind velocity. The B samplers as well as the sonic anemometer were operated during the entire campaign period. The A samplers were operated only during periods of favourable wind conditions (i.e., northerly wind direction).

Additional data were available for different pollen species [hazel (*Corylus*), 28 μm average diameter and sweet

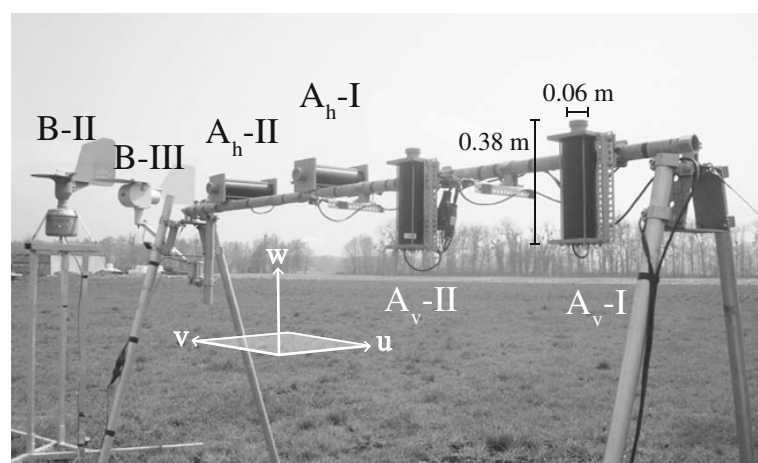
chestnut (*Castanea*), 14 μm average diameter, Bucher et al. (2004)]. These shorter intercomparisons were conducted in 2009 using a similar experimental arrangement as in Fig. 2, but at operational MeteoSwiss pollen monitoring sites.

Post-processing

The pollen concentration of B samples was calculated according to the recommendations of Mandrioli et al. (1998). In the case of A samplers, the pollen concentration was calculated as the ratio of the total pollen count and the aspirated volume of air. Since the exposure time was only 45 min, the concentration was extrapolated to 1 h. This may have led to a certain error when compared to B measurements, because pollen transport occurs as intermittent gusts rather than a steady pollen flux.

With respect to the azimuth of the horizontal A samplers (350°), only wind directions related to the mean wind direction $\pm 50^\circ$ were accepted for analysis.

Fig. 2 Set-up of instruments in the sampler intercomparison in Illarsaz 2010. Sampler *B-I* was mounted at the far right side of this figure. The coordinate system denotes the orientation of the wind components relative to the instrument orientation. Measurements from the Burkard Scientific sampler (*B-III*) were not used in the present study. The dimensions of the A sampler including the pump housing are specified for *A_v-I*



Overview on the sampler agreement

Prior to the comparison of different sampler types, the precision of each sampler type B, A_v and A_h was addressed separately on the basis of sweet chestnut and birch pollen measurements by analyzing pairs of identical sampler types.

The dataset of hazel pollen was not taken into account because the sample size was too small. The measurements indicate a good correlation of all sampler types ($R^2 \geq 0.61$, Table 1). The root mean square error (rmse) is used to quantify the precision of the instruments. The relative rmse is calculated as rmse normalized by $\langle \bar{c} \rangle$, where $\langle \bar{c} \rangle$ is the spatial and temporal average of the two measurements (e.g., A_v–I/II). The relative rmse of the A and B samplers is rather large (from 26% to 57%). The large error among the vertically oriented A samplers may have resulted from strong statistical effects of atmospheric inhomogeneities in the case of low $\langle \bar{c} \rangle$ measurements. In contrast, horizontal A samplers agree comparably well, since the observed $\langle \bar{c} \rangle$ is considerably larger. The large uncertainty among the B samplers arises from the counting procedure rather than from the aspiration efficiency. The agreement among identical sampler types is summarized in Table 1.

A re-analysis of three B slides was performed in order to quantify the influence of the number of sweeps on the calculated pollen concentration. The slides have been re-counted on the basis of 24-h -slides with 4 and 30 longitudinal sweeps of 0.36 mm width, which yields a coverage of 10% and 77%, respectively, of the impaction area (48 × 14 mm). Figure 3 illustrates that the position of the sweeps has a strong influence on the extrapolated total, if the distribution is not homogeneous (e.g., bipolar). Cariñanos et al. (2000) investigated different pollen counting methods of slides using a Hirst-type sampler. They found an overestimation of extrapolated pollen numbers when the sweeps are positioned in the middle of the slide, where most pollen are deposited. The present counting method considered depositions near the edge of the impaction area as well in the center. The variation in the numbers of sweeps yielded a relative error of 16%, when only 10% of the deposition area

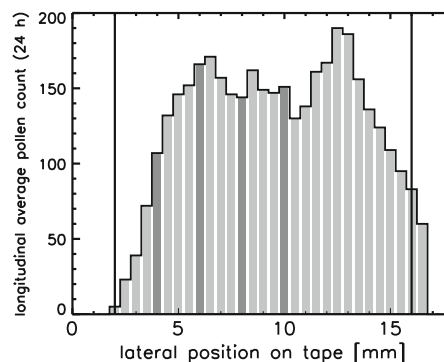


Fig. 3 Lateral pollen deposition on the Burkard sampling slide obtained from 24-h averages of longitudinal pollen counts. *Gray area* Absolute pollen counts (y-axis) and analyzed area (x-axis) when 30 sweeps were performed, *dark gray bars* four sweeps only performed, *black vertical lines* outer limits of impaction area, which corresponds to the inner inlet orifice (2 × 14 mm)

was analysed instead of 77%. Comtois et al. (1999) found a larger relative error (almost 30%) in the case of four sweeps (slide coverage of 13.3%), when 100% of the entire slide was analyzed.

Quantification of the error induced by vertical orientation

For the following sampler intercomparison, spatial averages of aspirated pollen concentrations, c , i.e., for example $\langle c_{Av} \rangle$, are analyzed, denoted as c_{Av} , c_{Ah} and c_B , respectively, where the subscripts refer to sampler type and orientation. The bias denotes the mean deviation of a data series from the reference. The relative bias is calculated as bias normalized by \bar{c} of the reference instrument. The relative rmse is calculated as rmse normalized by \bar{c} of the reference instrument.

Figure 4 illustrates that the aspiration efficiency is decreased when the sampler orifice is facing upwards. Hence, the vertically oriented samplers underestimated the pollen concentration dramatically in comparison to the B sampler. In the case of sweet chestnut pollen, the relative bias was -70% . The birch pollen measurements underestimated the concentration with an error of almost three orders of magnitude, with a relative bias of -104% . The better agreement of the sweet chestnut measurements is a result of their lower inertia compared to the larger birch pollen. The majority of the vertically measured concentrations did not exceed 60 pollen m^{-3} , while c_B observations range up to $5 \times 10^3 \text{ pollen m}^{-3}$.

The aspiration efficiency of the horizontal A samplers facing the freestream, in contrast, is considerably better. The c_{Ah} data agree well with the B samplers ($R^2=0.76$). However, the A_h samplers also slightly underestimate the pollen concentration, with a relative bias of -20% . The impaction efficiency of the A cassette already tends towards 100% with aerosols of an aerodynamic diameter up to $5 \mu\text{m}$

Table 1 Precision of different sampler types. The relative root mean square error (rmse) is calculated as rmse normalized by $\langle \bar{c} \rangle$, where rmse denotes the root mean square difference of two samplers (I and II) with the same orientation and $\langle \bar{c} \rangle$ is the spatial and temporal average of the two samplers. n Sample size

Pollen species sampler	Sweet chestnut Av-I/II	Birch Av-I/II	Birch Ah-I/II	Birch B-I/II
R^2	0.61	0.89	0.96	0.90
relative rmse [%]	37	57	26	38
$\langle \bar{c} \rangle$ [pollen m^{-3}]	19.0	25.3	684.7	848.9
n	24	47	47	47

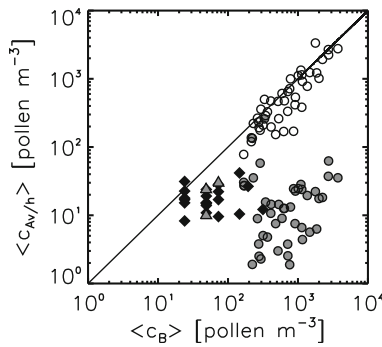


Fig. 4 Agreement of 1-h pollen concentrations measured with B and A samplers; *triangles* hazel, *squares* sweet chestnut, *circles* birch pollen. *Filled symbols* A_v data, *open symbols* A_h data. In the case of the birch pollen dataset, only cases where the wind direction was $\pm 50^\circ$ compared to the azimuth of the A_h samplers are shown. Note that the plot is double-logarithmic

(Aizenberg et al. 2000), i.e., much smaller and lighter than birch pollen (22 μm diameter; Birks 1968). Hence, the error of the A_h sampler is due mainly to its blunt design, diverting the approaching freestream. The relative bias between birch c_{A_v} and c_{A_h} amounts to -105% . This denotes a very large error between identical samplers, which is induced by their orientation. The relative errors of the A_v sampler are summarized in Table 3.

Aspiration characteristics of blunt samplers at different orientations

Experimental and theoretical work on the determination of the aspiration efficiency of aerosol samplers related mostly to thin-walled, tubular inlets facing the freestream, e.g., Badzioch (1959) and Belyaev and Levin (1974). This idealization was a starting point to understanding the basic principles that determine aspiration efficiency. In practice, however, the flow pattern upstream of a sampler orifice is much more complex. It is affected by various parameters, such as the orientation, θ , of the orifice relative to the freestream, the aspiration velocity and the characteristic bluntness of the sampler body. Vincent et al. (1986) have investigated the physics of thin-walled samplers with respect to their orientation relative to the freestream. Based on his work, Tsai and Vincent (1993) developed a model for the range of blunt samplers, which was assessed in the present for the single case of vertical orientation.

In theory, the aspiration efficiency of a sampler is defined by:

$$E_t = c/c_0, \tag{1}$$

where c is the particle concentration entering the plane of the sampler inlet, and c_0 is the upstream concentration, given that the air and particle velocity distributions are

uniform. Taking into consideration the influence of inertial effects on the aspiration efficiency due to divergence and convergence of the flow as it approaches the sampler inlet, Eq. 1 can be extended to:

$$E = \frac{c}{c_0} = 1 + \beta(R - 1), \tag{2}$$

where β is the impaction efficiency, defined as the ratio between the number of particles impacting onto the virtual plane between the limiting trajectories, and the number of particles impacting onto the plane of the sampling orifice. A robust empirical expression for β (Vincent 2007) is:

$$\beta = 1 - \frac{1}{1 + GSt}, \tag{3}$$

where St is the particle Stokes number and G is an empirical coefficient, which was investigated by Belyaev and Levin (1974) and Paik and Vincent (2002). R is defined as:

$$R = \frac{U}{U_s}, \tag{4}$$

where U is the freestream velocity and U_s is the sampling velocity through the sampling plane. The sampling velocity of the A sampler is $U_s = 1.84\text{ ms}^{-1}$. In the case of idealized thin-walled samplers, $R=1$ denotes isokinetic sampling, where $E_t=1$. If sampling is sub-isokinetic ($R>1$) or super-isokinetic ($R<1$), the trajectories of the air flow are divergent or convergent, respectively, and particles are either gained or lost at the sampler inlet due to inertial effects on the particle motion. With respect to orientations up to $\theta=90^\circ$, Eq. 2 can be expressed by an impaction model, which in similar form was used by Belyaev and Levin (1974); Durham and Lundgren (1980); Vincent et al. (1986); Wiener et al. (1988); Lipatov et al. (1988); Vincent (1989); Grinshpun and Lipatov (1990); Hangal and Willeke (1990a, b); Grinshpun et al. (1994) and Vincent (2007):

$$E_\theta = \frac{c}{c_0} = 1 + \beta_\theta(R \cos \theta - 1) \tag{5}$$

The aspiration performance of a blunt sampler facing upwards in calm air, i.e., for super-isokinetic sampling, has been investigated by Dunnett et al. (2006). The particle Stokes number St accounts for turbulent particle motion, i.e., the inertially dominated behavior of particles in a distorted flow and is defined as:

$$St = \frac{\tau U}{\delta}, \tag{6}$$

where δ is the sampling orifice width, and τ is the response time of the particle to perturbation. It can be expressed as:

$$\tau = \frac{\gamma^* d_{ae}^2}{18\mu}, \tag{7}$$

where μ is the dynamic molecular viscosity of air, and d_{ae} is the aerodynamic particle diameter. d_{ae} characterizes a sphere with the density equivalent to water $\gamma^*=1 \text{ g cm}^{-3}$ and, therefore, has the same settling velocity as the particle in question. For laminar flow d_{ae} is defined as:

$$d_{ae} = d \left(\frac{\gamma}{\gamma^*} \right)^{1/2}, \tag{8}$$

where d is the particle diameter.

Thus, the Stokes number denotes the ratio of the stopping distance τU_0 of the particle to the width of the sampler orifice, when the particle motion is turbulent, i.e., within distorted flow. Small values of St indicate that the particles tend to follow the fluid trajectories, while large values indicate a separation of particle motion from the fluid motion.

Based on experimental studies on the human head (Ogden and Birkett 1977; Armbruster and Breuer 1982) and cylindrical thin-walled samplers (Vincent et al. 1986), an aspiration model for the limited case of blunt samplers with orientation $\theta = 90^\circ$ was developed (Tsai and Vincent 1993). It is expressed as:

$$E_{90} = \frac{1}{1 + 4G_{90}r^{g_1} StR^{1/2}}, \tag{9}$$

where G_{90} and g_1 are both empirical coefficients. Tsai and Vincent (1993) obtained an agreement of the corrected data of $R^2=0.61$ for $G_{90}=2.21$ and $g_1=-0.5$, where G_{90} is a scale of the sampler bluntness and g_1 is a modification of the inlet dimension ratio $r=\delta/D$, where D is the characteristic sampler width. It is important to understand that the area projected upstream by the sampler body, i.e., its bluntness, increases with θ (Lundgren et al. 1978). Assuming $r=1$, the term $G_{90}r^{g_1}$ approaches the bluntness of a thin-walled sampler, which was empirically determined to be $G_0=2.1$ for θ up to 90° (Vincent et al. 1986).

An alternative linear correction for vertical aspiration using wind velocity

Aspiration efficiency is dependent strongly on the sampler design, i.e., affected by the characteristic bluntness of the sampler body and the inlet design, described with r . It is unknown to what extent the findings of human head studies (Ogden and Birkett 1977; Armbruster and Breuer 1982; Vincent et al. 1986) apply to the bulky body of the A sampler in the present work. Therefore, an alternative approach to the correction of vertical aspiration is presented, which applies only to the exact experiment sites of the present study and that of Michel et al. (2010).

Based on the knowledge of inertial effects on suspended particle motion, the relation between wind velocity and the discrepancy between A_v and A_h samplers was determined using the data collected during sampler intercomparison in order to

obtain a relative correction of A_v against A_h . The correlation of the corrected A_v with the B data was then determined.

Since the A_h sampler azimuth is fixed, i.e., not automatically wind-oriented, the effect of yaw orientations needed to be minimized. Therefore, only the wind component u facing the A_h sampler orifices with a threshold of $\pm 50^\circ$ were accepted for analysis. Hence, R is expressed as $R=\bar{u}/U_s$. Figure 5 shows that the slope of c_{Av} deviations from c_{Ah} is steeper, when $R>1$, than for cases where $R<1$. Therefore, the linear regression was calculated separately for cases where $R\leq 1$ and $R>1$. Consequently, the correction procedure incorporates sub-models separated according to the longitudinal wind velocity. The correlation of A_v with A_h data provided two models, which use different sets of coefficients according to values of u (Eqs. 10, 11):

$$c_{lin}^* = \alpha_1 c_{Av} + \alpha_2 \bar{u}, \quad \text{if } R \leq 1 \text{ and } c_{Av} > 0 \tag{10}$$

$$c_{lin}^* = \alpha_3 c_{Av} + \alpha_4 \bar{u}, \quad \text{if } R > 1 \text{ and } c_{Av} > 0, \tag{11}$$

where c_{lin}^* denotes the corrected pollen concentration.

In a second step, the c_{lin}^* data are fitted against the B data to decrease the offset indicated in Fig. 4 between B and A_h measurements. The resulting linear correction model is defined as:

$$c_{lin}^{**} = \beta_1 c_{lin}^*, \quad \text{if } c_{lin}^* > 0 \tag{12}$$

where c_{lin}^{**} refers to the concentration of the vertically oriented A samplers after the 'double correction'. The goodness-of-fit and coefficients of linear models c_{lin}^* and c_{lin}^{**} are shown in Table 2.

Results

Performance of the physically based aspiration model

The aspiration model for upwards-facing blunt samplers (Eq. 9) was tested against the measured aspiration efficiency

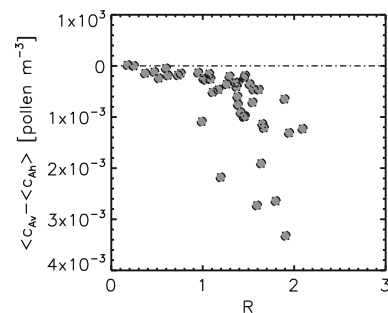


Fig. 5 The difference $c_{Av}-c_{Ah}$ as a function of $R=\bar{u}/U_s$, where \bar{u} is the longitudinal wind component, and U_s is the sampling velocity of the Air-O-Cell sampler (1.84 m s^{-1})

Table 2 Goodness-of-fit and coefficients of statistical models. c_{lin}^* denotes the linear correction of A_v data using Eqs. 10 or 11 according to the longitudinal wind velocity component \bar{u} , c_{lin}^{**} denotes the linear correction of A_v data using Eq. 12

Correction	Validity range	Predictors	R^2	P-value
c_{lin}^*	$R \leq 1$	$c_{Av}; \bar{u}$	0.62	0.01
c_{lin}^*	$R > 1$	$c_{Av}; \bar{u}$	0.78	$1.04 \cdot 10^{-10}$
c_{lin}^{**}	Entire data range	c_{lin}^*	0.85	$2.2 \cdot 10^{-16}$
Coefficients				
c_{lin}^*	$R \leq 1$	0.91 (α_1)	225.93 (α_2)	
c_{lin}^*	$R > 1$	36.09 (α_3)	176.02 (α_4)	
c_{lin}^{**}	Entire data range	1.17 (β_1)		

of A_v samplers, assuming a birch pollen diameter $d=22 \mu\text{m}$ (Birks 1968) and a density $\gamma=800 \text{ kg m}^{-3}$. The measured aspiration efficiency of the vertical samplers was determined with $E_{Av}=c_{Av}/c_B$. Note that the aspiration of the B sampler underlies the same inertial effects discussed above. Its bulky body presents a considerable obstacle to the freestream, which distorts the freestream as it approaches the sampler. Since the B sampler was designed to rather register inhalable aerosols, its readings do not exactly represent the atmospheric concentration. The ‘true’ aspiration efficiency of the B sampler was determined by Ogden et al. (1974) using Ambrosia pollen ($20 \mu\text{m}$). A mathematical equation for the empirical data was provided by Frenz (1999). Figure 6 shows that the B sampler aspiration declines to 60% at $U=5 \text{ ms}^{-1}$. With increasing wind velocity, the aspiration efficiency exceeds 100%. Hence, measurements aiming at the atmospheric aerosol concentration need to be corrected with respect to wind velocity. The physically based aspiration model, however, was derived also from studies on inhalability by the human head. Therefore, comparison of the model to the uncorrected B sampler seems reasonable.

Figure 7 shows that the physically based model dramatically overestimates the aspiration efficiency of the A_v

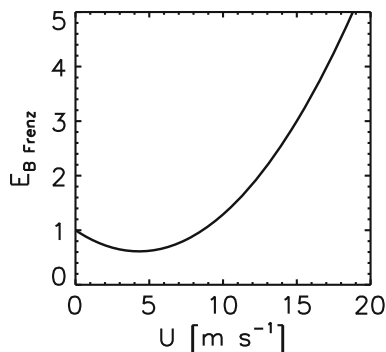


Fig. 6 Aspiration efficiency of the Burkard sampler as a function of the wind velocity U , using the mathematical equation provided by Frenz (1999) based on the empirical data of Ogden et al. (1974)

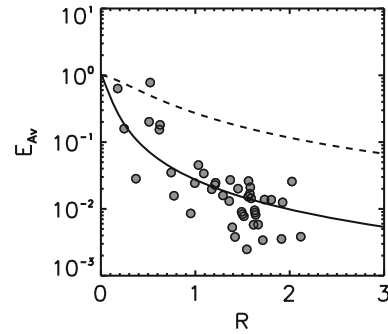


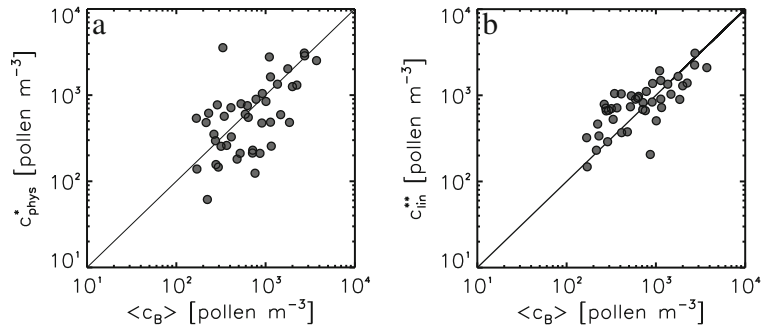
Fig. 7 Measured aspiration efficiency $E_{Av}=c_{Av}/c_B$ plotted as a function of $R=U/U_s$, where U is the freestream velocity and U_s is the sampling velocity of the Air-O-Cell sampler (1.84 ms^{-1}). Dashed curve Modeled aspiration efficiency E_{90} using $G_{90}=2.21$ and $g_l=-0.5$, solid curve Modeled (Eq. 9) using $G_{90}=29.35$ and $g_l=-0.5$. Note that the y-axis is logarithmic

sampler, when the empirical value $G_l=2.21$ determined from human head studies (Tsai and Vincent 1993), is used. The best results (i.e., the lowest bias) for the A_v data yields $G_{90}=29.35$ with $g_l=-0.5$. Thus the parameter G_{90} needs substantial modification for the vertical A sampler, since the greater bluntness of the sampler body must be taken into account. It seems that the exact value of G_{90} is a strong function of the very sampler design. To what extent this value can be considered characteristic for an Air-O-Cell sampler depends on the dimension of the pump housing. Thus it would be helpful to determine the dependence of G_{90} on different sampler designs. The model was used with $G_{90}=29.35$ to correct the vertically measured data through:

$$c_{phys}^* = \frac{1}{E_{90}} c_{Av}, \tag{13}$$

where c_{phys}^* denotes the corrected A_v pollen concentration. Note that the data are corrected only when the deviation from B samplers is larger than the rmse of the B samplers. The correlation of the corrected data ($R^2=0.39$) is considerably less than that of Tsai and Vincent (1993) for their aerosols of aerodynamic diameters up to $60 \mu\text{m}$. The model generally underestimates the measurements when $R \leq 1$, and generally overestimates when $R > 1$. The relative bias and relative rmse between c_{phys}^* and c_B is 0% and 89%, respectively. Figure 8a shows that the corrected data as a function of c_B are widely scattered. A significant correlation can be found only due to a satisfying agreement for pollen concentrations $c > 1 \times 10^3 \text{ pollen m}^{-3}$. Since no pollen counts are considered in Eq. 9, the physically based correction can not take into account errors that are induced by effects other than the aspiration efficiency, e.g., the error due to the extrapolation of A sampler data, as discussed earlier. The errors of the uncorrected and corrected data are summarized in Table 3.

Fig. 8 **a** Corrected 1-h A_v data (c_{phys}^*) using the physically based model, as function of c_B . **b** Corrected 1-hour A_v data (c_{lin}^{**}) using the linear model, as function of c_B . Note that the plots are double-logarithmic



Performance of the linear correction model

The performance of the linear correction was tested against B sampler measurements. The linear model was used to correct the vertically measured data. Note that the data are corrected only when the deviation from B samplers is larger than the rmse of the B samplers. The correlation of the corrected data is $R^2=0.63$ and the relative rmse is 57%. Although the error is still relatively large, it is not substantially larger than the precision error of the B sampler (Table 1). The relative bias of 3% indicates a slight overestimation of the corrected c_{lin}^{**} . Figure 8b shows that the scatter of the corrected data c_{lin}^{**} as function of c_B is considerably less than in the case of the physical model. The linear correction takes into account the measured pollen concentration. Therefore, errors resulting from, e.g., the extrapolation of A sampler data, are taken into account to a certain extent. The errors of the uncorrected and corrected data are summarized in Table 3.

Table 3 Summary of relative bias (mean deviation normalized by the corresponding mean pollen concentration $\langle \bar{c} \rangle$ shown in Table 1) and relative rmse (normalized by the corresponding mean pollen concentration $\langle \bar{c} \rangle$ shown in Table 1) between uncorrected and corrected A_v and B samplers (reference) using the physically based and the linear model, respectively. c_{Av} denotes uncorrected measurements of the vertically oriented A_v sampler, c_{Ah} denotes measurements of the horizontally oriented A_h sampler, c_B denotes measurements of the B sampler, c_{lin}^{**} denotes the corrected c_{Av} data using the linear model (Eq. 12) and c_{phys}^* denotes the corrected c_{Av} data using the physically based model (Eq. 9). The values of the relative bias and relative rmse are given in percent

Data	c_{Ah} (Reference)			c_B (Reference)		
	Relative bias	Relative rmse	R^2	Relative bias	Relative rmse	R^2
c_{Av}	-105	154	0.00	-104	140	0.00
c_{Ah}	-	-	-	-20	50	0.76
c_{lin}^*	9	74	0.60	-	-	-
c_{lin}^{**}	-	-	-	3	57	0.63
c_{phys}^*	-	-	-	0	89	0.39

Conclusions

The present work quantified in a field experiment the uncertainty of vertically oriented blunt aerosol sampling systems using Air-O-Cell cassettes. The investigation focussed on the decrease of vertical pollen aspiration (hazel, sweet chestnut and birch) due to inertial effects on aerosol motion in moving air. The aspiration efficiency of the vertical samplers was determined with wind-oriented reference samplers (Hirst-type Burkard sampler, horizontal Air-O-Cell sampler). The decrease of aspiration efficiency of the vertically oriented sampler resulted in a substantial underestimation of the pollen count relative to horizontal measurements (-104% relative bias). This underlines the importance of applying a correction when the sampler inlet is facing upwards, as is quite common in, e.g., aeroallergenic research. Wind-oriented mounting of the same sampler type yields an considerably smaller underestimation relative to horizontal measurements (-20% relative bias). A physically based semi-empirical correction model was verified with birch pollen measurements for the purpose of the vertically oriented Air-O-Cell sampler. Additionally, a linear model was developed on the basis of pollen counts and wind velocity measurements. Both models were capable of notably reducing the error induced by vertical sampling. In comparison to the physical model, the linear correction yielded a better agreement to the reference. The linear model, however, is valid only under the very conditions of the experimental site and for the specific sampler design. The physically based model, in contrast, can be transferred to each upwards-facing blunt sampler type. It should be noted, however, that the characteristic bluntness of a sampler might make a modification of the semi-empirical model necessary in order to provide a robust correction.

The precision error of the wind-oriented Air-O-Cell sampler is rather large (26% of the mean concentration), yet is smaller than the precision error found for the Burkard sampler (38%). The Air-O-Cell cassette itself, therefore, can be considered a good low-priced alternative to, e.g., the widely used Burkard sampler. Attention should focus on the pump housing that is attached to the sampling cassette, however, since it may strongly affect the aspiration efficiency.

The results of the sampler intercomparison clearly point out that aspiration of aerosols (i.e., heavy aerosols such as pollen) should always be wind-oriented. In the case of blunt samplers and non-isokinetic sampling, the sampling error is a function of wind velocity, also in the case of a wind-oriented inlet. Thus under field conditions, a physically based correction of pollen counts is indispensable.

Acknowledgments Our great appreciation goes to the European Cooperation in Science and Technology (COST) Action ES0603. Financial support for this project by the Swiss State Secretariat for Education and Research (SBF), grant C07.0111, and the Freiwillige Akademische Gesellschaft Basel, is gratefully acknowledged. Many thanks go to MeteoSwiss and the MCR Lab, University of Basel. Their contribution to the field campaigns and the pollen analysis is highly appreciated. The comments of an anonymous reviewer to a first draft of the present paper led to a substantial improvement of the results from this study and are gratefully acknowledged.

References

- Aizenberg V, Reponen T, Grinshpun S, Willeke K (2000) Performance of Air-O-Cell, Burkard and Button Samplers for total enumeration of airborne spores. *Am Ind Hyg Assoc J* 61:855–864
- Ambruster L, Breuer H (1982) Investigations into defining inhalable dust. Pergamon, Oxford, pp 3–19
- Badzioch S (1959) Collection of gas-borne dust particles by means of an aspirated sampling nozzle. *Br J Appl Phys* 10:26–32
- Belyaev S, Levin L (1974) Techniques for collection of representative aerosol samples. *J Aerosol Sci* 5:325–338
- Birks H (1968) The identification of *betula nana* pollen. *New Phytol* 67:309–314
- Bucher E, Kofler V, Vorwohl G, Zieger E (2004) Das Pollenbild der Südtiroler Honige. Landesagentur für Umwelt und Arbeitsschutz, Biologisches Labor
- Cariñanos P, Emberlin J, Galán C, Domínguez-Vilches E (2000) Comparison of two pollen counting methods of slides from a hirst type volumetric trap. *Aero* 16:339–346
- Comtois P, Alcazar P, Neron D (1999) Pollen counts statistics and its relevance to precision. *Aerobiologia* 15:19–28
- Dunnett S, Wen X, Zaripov S, Galeev R, Vanunina M (2006) A numerical study of calm air sampling with a blunt sampler. *Aerosol Sci Technol* 40:490–502
- Durham M, Lundgren D (1980) Evaluation of aerosol aspiration efficiency as function of stokes number, velocity ratio and nozzle angle. *J Aerosol Sci* 11:179–188
- Frenz D (1999) Comparing pollen and spore counts collected with the Rotorod sampler and Burkard spore trap. *Ann Allergy Asthma Immunol* 83:341–347
- Gottardini E, Cristofolini F, Cristofori A, Vannini A, Ferretti M (2009) Sampling bias and sampling errors in pollen counting in aerobiological monitoring in Italy. *J Environ Monitor* 11:751–755
- Grinshpun S, Lipatov G (1990) Sampling errors in cylindrical nozzles. *Aerosol Sci Technol* 12:716–740
- Grinshpun S, Chang CW, Nevalainen A, Willeke K (1994) Inlet characteristics of bioaerosol samplers. *J Aerosol Sci* 25(8):1503–1522
- Hangal S, Willeke K (1990a) Aspiration efficiency: unified model for all forward sampling angles. *Environ Sci Technol* 24:688–691
- Hangal S, Willeke K (1990b) Overall efficiency of tubular inlets sampling at 0–90 degrees from horizontal aerosol flows. *Atmos Environ* 24A:2379–2386
- Hirst J (1952) An automatic volumetric spore trap. *Ann Appl Biol* 39:257–265
- Levetin E (2004) Methods for aeroallergen sampling. *Curr Allergy Asthma Rep* 4:376–383
- Lipatov G, Grinshpun S, Semenyuk T, Sutugin A (1988) Secondary aspiration of aerosol particles into thin-walled nozzles facing the wind. *Atmos Environ* 22:1721–1727
- Lundgren D, Durham M, Mason K (1978) Sampling of tangential flow streams. *Am Ind Hyg Assoc J* 39:640644
- Mandrioli P, Comtois P, Levizzani V (1998) Methods in aerobiology. Pitagora Editrice, Bologna, Italy
- Michel D, Gehrig R, Rotach M, Vogt R (2010) Micropoem: experimental investigation of birch pollen emission. In: 19th Symposium on Boundary Layer and Turbulence, 2–8 August, Keystone, Colorado
- Ogden T, Birkett J (1977) The human head as a dust sampler. Pergamon, Oxford, pp 93–105
- Ogden E, Raynor G, Hayes J, Lewis D, Haines J (1974) Manual for sampling airborne pollen. Hafner, New York
- Paik S, Vincent J (2002) Aspiration efficiency for thin-walled nozzles facing the wind and for very high velocity ratios. *J Aerosol Sci* 33:705720
- Tsai P, Vincent J (1993) Impaction model for the aspiration efficiencies of aerosol samplers at large angles with respect to the wind. *J Aerosol Sci* 24:919–928
- Vincent J (1989) Aerosol sampling: science and practice. Wiley, Chichester
- Vincent J (2007) Aerosol sampling: science, standards, instrumentation and applications. Wiley, Chichester
- Vincent J, Stevens D, Mark D, Marshall M, Smith T (1986) On the spiration characteristics of large-diameter, thin-walled aerosol sampling probes at yaw orientations with respect to the wind. *J Aerosol Sci* 17:211–224
- Wiener R, Okazaki K, Willeke (1988) Influence of turbulence on aerosol sampling efficiency. *Atmos Environ* 22:917–928

5 Transport of background pollen concentration across a natural windbreak

5.1 Introduction

In Section 3.3 the disturbance of the wind flow due to mechanical production of turbulence in the birch canopy has been addressed. In the case of heavy particles, fluid dynamics of the turbulent flow have a large effect on suspended particles, due to their greater inertia. Complex spatial variations of the concentration result from stochastic acceleration and deceleration of the particle with the disturbed flow regime. Additionally, the birch canopy acts as a sink for particles, since a part of the pollen impacting on the canopy are deposited on vegetation elements. The combined effect of wind field disturbance and deposition yields a very complex pattern of background concentration in comparison to the undisturbed upwind situation. In order to be able to accurately estimate the emission from the isolated source by eliminating the bias of background concentration, the transport of the latter across the windbreak is simulated using a CFD model incorporating the wind field effect as well as a separate model accounting for deposition.

The used methods and results of the pollen dispersion simulations are described in the following Section 5.2, which is prepared for submission to *Agr. Forest Meteorol.* in an adapted form.

5.2 Modelling and observations of pollen transport through a natural windbreak

Michel, D.¹, Gartmann, A.¹, Rotach, M.W.²

1) MCR Lab, University of Basel, Switzerland

2) Institute of Meteorology and Geophysics, University of Innsbruck, Austria

Abstract

Vertical profile measurements of birch pollen concentrations up- and downwind of a windbreak consisting of emitting birch trees are used to assess the transport of pollen through the vegetation canopy. A modelling approach aims at simulating the dispersion of birch pollen several hundreds of meters up- and downwind of the thin windbreak with a width/height ratio $w_s/h = 1.6$. The windbreak effect on the concentration fields is numerically simulated with a CFD (computational fluid dynamics) model. The trajectories of airborne pollen are modelled with respect to gravitational settling using a stochastic Lagrangian approach, driven by a wind and turbulence field based on the RANS (Reynolds-averaged Navier-Stokes) method. The filtering effect, i.e. deposition of pollen on vegetation elements within the windbreak, is estimated using a pollen transmissivity model based on the optical porosity of the canopy. The simulated dispersion of background pollen with respect to the two effects is compared to measurements of birch pollen concentrations up- and downwind of the windbreak in order to validate the model performance.

Although the windbreak is thin and porous, the effect of updraft in its upwind area induced by the bluffness of the windbreak as well as accumulation due to deceleration both result in significant local variations of the pollen concentration. Pollen entrapment within the windbreak, on the other hand, has a comparably small effect due to the high porosity of the windbreak.

Using numerical models for assessing the influence of windbreaks on particle concentration under

natural conditions may sometimes be too elaborate in existing or planned operational and experimental frameworks. Therefore, a parameterisation of the particle transport across the windbreak based on the numerical simulations is presented, which allows to estimate windbreak effects on up- and downwind concentrations as function of the distance from the roughness element without the use of a numerical model.

Introduction

Natural windbreaks or shelterbelts are often planted in order to minimise particle loss by drift (e.g. fertilizer), or to shelter adjacent downwind areas from contamination, e.g. with pesticides or pollen of genetically modified (GM) crops (Wenneker et al., 2005; Mercer, 2009). Observations and modelling of the particle concentration field up- and downwind of windbreaks aim at assessing their effectiveness of reducing particle transport into the downwind area. Dispersion of particles up- and downwind of a natural porous windbreak is influenced essentially by two effects: Distortion of the wind flow and turbulence fields *up- and downwind* of the shelterbelt and modification of the particle deposition *within* the canopy. The distortion effect of natural windbreaks on the wind field has been investigated in several numerical simulation and observation studies, e.g. Wilson (1985); McNaughton (1988); Cleugh (1998, 2002); Vigiak et al. (2003); Santiago et al. (2007) and Rosenfeld et al. (2010). If the downwind particle concentration field originating from an upwind source is of interest, both the up- and downwind flow distortion as well as the upwind source location relative to the leading edge of the windbreak are relevant. Within the windbreak, deposition of airborne particles is also modified due to disturbance of wind flow and turbulence on the one hand and impact on vegetation elements on the other hand. This effect reduces the particle load emerging on the downwind face of the shelterbelt in comparison to the upwind particle concentration. This influence of the vegetation on particle deposition will be called the filtering effect. The process of particle deposition to plant canopies has been investigated by Bache (1981); Petroff et al. (2008, 2009). The skills of numerical simulation of heavy particle dispersion with respect to inertial effects using a Lagrangian approach have been documented by Wilson (2000); Reynolds (2000); Aylor and Flesch (2001); Boehm and Aylor (2005); Cai et al. (2006). Only few observational and numerical simulation studies focus on the dispersion of heavy particles in a wind field disturbed by a natural windbreak, i.e. with respect to either the effects of flow distortion due to the canopy roughness (Jarosz et al., 2003, 2004) or filtering (Bouvet et al., 2007; Guo and Maghirang, 2012) on downwind particle concentration. To the knowledge of the authors no systematic investigation of the combined effect of both processes are available with respect to particle inertia and for several hundreds of meters up- and downwind of a natural windbreak.

The present study is motivated by an 'emission experiment', which aimed at estimating the strength of birch pollen emission of an isolated natural source (Michel et al., 2010), i.e. a thin shelterbelt consisting of birch trees with the width/height ratio $w_s/h = 1.6$. Birch trees were used because their pollen are among the most important allergens in Europe, contributing to the continuously increasing prevalence of diseases due to aeroallergens over the last decades (Skoner, 2001). The study used temporally and spatially highly-resolved vertical and longitudinal observations in order to infer the natural pollen emission from the distribution of downwind pollen concentrations and detailed meteorological information.

In the present contribution a CFD model, simulating the particle trajectories with respect to inertial motion using a stochastic Lagrangian approach driven by a RANS flow field, is used to model the influence of the windbreak on wind flow and particle deposition in order to estimate the shelter effect of the windbreak. The results are used to isolate the emission strength, which will be the subject of a later study. A parameterisation of the particle transport across the windbreak derived from the numerical simulations is established based on vertical footprints of pollen concentration,

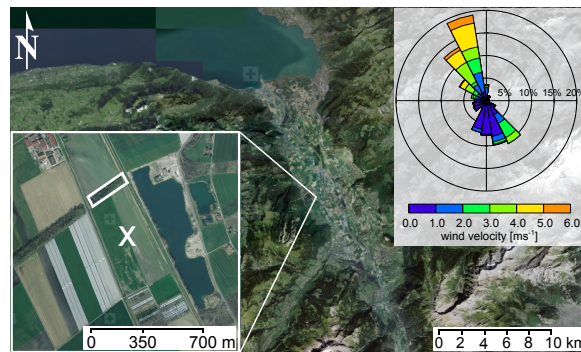


Figure 1: Satellite images of the experiment location in Illarsaz, Switzerland (Lake of Geneva at the top left). The image at the lower left shows the location of the study site (cross), the square denotes the outline of the windbreak. The frequency of wind direction and velocity measured at 18 m above ground upwind of the windbreak is shown at the top right. Federal Office of Topography swisstopo.

in order to provide an estimate of the windbreak effect on observations in case no numerical simulations were available.

The present paper is structured as follows: In the second section the material used in the 'emission experiment' and the principles of particle transport through a natural windbreak as well as of the CFD model are explained. In the third section the results of the particle simulations are compared to in-situ measurements. The fourth section includes the principles and results of the parameterisation of the simulations.

Material and Methods

Experimental site

Since the study uses 'natural tracers' rather than a controlled particle release, the experimental set-up had to respond to the need of inferring the emission from the observed downwind concentration. To facilitate the measurements, the study site was chosen such that it is dominated by persistent wind directions. The field measurements were conducted in the Rhone River Valley in Illarsaz, Switzerland during the birch emission period from 2 to 24 April 2009 (Fig. 1). The location is characterised by a mountain-valley wind system during clear weather periods, which produced northeasterly upvalley winds during daytime and southerly downvalley winds during nighttime. The windbreak is located centrally in the valley with an approximately normal exposition to the mean wind. This natural windbreak consists of five rows of mainly birch trees (*Betula pendula* and *B. pubescens*), which extends 203 m in the cross-wind and 30 m in the along-wind direction. The average height is $h = 19$ m. The height of the understorey is approximately 0.75 m and consists of grass. The region around the tree stand consists of bare soil in the upwind area. The downwind area is divided along the center-line of the windbreak into a pasture crop (east) and a potato crop (west), which was covered with acrylic sheets.

Instrumentation

The set-up was laid out up- and downwind of the pollen source along the main wind direction and aimed at continuously measuring the exchange conditions in longitudinal and cross-wind transects.

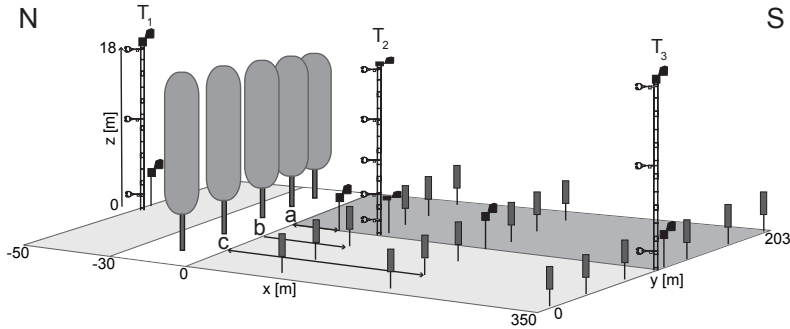


Figure 2: Set-up of sonic anemometers and bioaerosol samplers at the upwind tower T_1 and the downwind towers T_2 and T_3 . The black icons denote Hirst-type samplers and the grey icons denote AOC samplers. The dark grey area south of the windbreak denotes the grass crop, the light grey area denotes the acrylic cover. The distances from the windbreak are *a*) 30 m *b*) 100 m *c*) 200 and 350 m.

Vertical profiles of micrometeorological variables and pollen concentrations were monitored at three towers of 18 m height. They were located centrally (with respect to the cross-wind distance of the windbreak) at 20 m north and 100 m/350 m south of the pollen source (T_{1-3} in Fig. 2). Each tower was equipped with three ($T_{1,3}$) or five (T_2) CSAT3 ultrasonic anemometers (Campbell Scientific, Ltd., 20 Hz resolution) and two Hirst-type (Hirst, 1952) pollen samplers [7-Day Spore Sampler, Burkard Manufacturing Co. Ltd. (Mandrioli et al., 1998) at $T_{1,3}$ and Sporewatch, Burkard Scientific at T_2] at 2 m and 18 m, respectively, above ground. Two additional Burkard traps at 2 m height were located 30 m and 200 m downwind of the windbreak (see Fig. 2).

In addition to the continuous two-hour measurements, an array of 18 Air-O-Cell (AOC) aspiration samplers [Zefon Int., (Levetin, 2004)] was laid-out at 2 m above ground, which was operated during five intensive operation periods (IOP), when the weather was clear and northerly (upvalley) wind prevailed. The sensor array aimed at measuring the pollen concentration in three cross-wind transects in the distances of 100 m, 200 m and 350 m downwind of the source.

The Hirst-type pollen traps use the impaction method, where airborne particles are aspirated with a rate of rate of $0.6 \text{ m}^3 \text{ hour}^{-1}$ through a slit orifice and impinge on a sampling substrate. The sampling substrate is applied to a rotating cylinder, which yields a continuous seven-day information on airborne particle abundance. The number of trapped pollen is determined according to the statistical methods described by Mandrioli et al. (1998), to achieve a temporal resolution of two hours. The sensors use a wind vane to align the orifice towards the oncoming wind. The sensor is designed to measure the inhalability of particles rather than their atmospheric concentration (Tsai and Vincent, 1993; Lacey and West, 2006), using a constant aspiration rate. The sampled volume of air is defined as:

$$V_s = U_s t A_o, \quad (1)$$

where A_o is the area of the sampling orifice and t is the sampling interval. In the case of isokinetic sampling (Gregory et al., 1961; Raynor, 1972; Aylor and Qiu, 1996) the collected pollen can be associated to the volume of air V_a that passed the area A_o and thus yielding the atmospheric pollen concentration, because $V_s = V_a$. In the case of anisokinetic sampling, i.e. when the aspirated flow velocity (U_s) does not equal the free stream velocity, the particle collection is biased due to divergence or convergence, respectively, of the free stream upwind of the sensor (May, 1945; Watson, 1954). In addition, the sampling efficiency is affected as function of wind velocity by the upwind-projected bluntness of the sensor, inducing divergence of the free stream (Ingham, 1981; Vincent and Mark, 1982; Vincent et al., 1982; Dunnet and Ingham, 1986). A comprehensive description of the underlying physical processes in particle sampling can be found in Vincent (2007). The sampling efficiency is strongly influenced by diverging particle and fluid trajectories due to inertial movement of heavy particles. The measured Burkard data thus need to be corrected in

order to represent the atmospheric pollen concentration. On the basis of empirical data (Ogden et al., 1974; Frenz, 1999) a correction function for Burkard data (C_F) has been defined, which accounts for the influence of wind velocity (U) on the sampling efficiency and thus compensates over- or underestimation of sampled pollen. C_F is based on the ratio between the known sampling velocity of the Burkard trap and the variable freestream velocity. At sensor locations, where no direct wind measurement is available (20 and 200 m downwind of the windbreak), input for C_F was determined by interpolation of adjacent measurements. The atmospheric concentration c can be calculated from the Burkard measurements with:

$$c = \left(\frac{n_p}{U_s t A_o} \right) C_F, \quad (2)$$

where n_p denotes the number of sampled pollen and t is the length of the measurements interval. The factor $(U_s t A_B)$ expresses the sampled volume of air.

The AOC sampling also uses the impaction method. Airborne particles are aspirated through disposable cassettes, which contain a glass slide coated with a sampling substrate. The sampling aspiration was generated with a self-built membrane pump, which produces an air flow rate of $1.1 \text{ m}^3 \text{ hour}^{-1}$. The temporal information relates to the exposure time of the cassette. A temporal resolution of one hour was achieved by extrapolating the exposure time of 45 minutes of each AOC sampling slide. In order to determine the number of trapped pollen, the entire sampling slide was analysed. The sensors were oriented vertically (upward facing) in order to make the measurements independent of wind direction. Yet, besides the effects of divergence and convergence of the free stream, the orifice orientation perpendicular to the mean horizontal pollen flow has a large impact on the sampling efficiency due to the inertial movement of the airborne pollen, resulting in a substantial underestimation of the sampled pollen number. Therefore, the performance of the AOC samplers was investigated in a separate field experiment (Michel et al., 2012). A correction function based on the longitudinal wind velocity component was established in reference to the Burkard measurements. C_F is therefore also applied to the corrected AOC observations in order to account for anisokinetic sampling.

Pollen transport across a windbreak

Within an undisturbed airflow under neutral stability conditions, the vertical wind profile can be assumed to be logarithmic. The concentration field of airborne particles under undisturbed conditions is assumed to be uniform in the longitudinal and cross-wind direction and to vary only with height. If the airflow encounters a transverse windbreak, the wind profile is disturbed, which affects the distribution of the airborne particles. Divergence of the fluid trajectories and deceleration of wind velocity favour the deposition of pollen to the ground. Filtering due to impaction and entrapment on obstacle elements in the canopy (stems, branches and leaves) results in a smaller number of pollen emerging from its downwind face. Hence, the windbreak transforms the undisturbed upwind pollen distribution into a non-uniform concentration field within the up- and downwind area. The shelter effect weakens from top to ground with increasing distance as pollen from above the windbreak are entrained, until the downwind concentration eventually adjusts to the undisturbed upwind situation. The undisturbed pollen concentration far upwind of the windbreak will be named background concentration (c_0), which is only a function of height, according to the assumption of uniform longitudinal and cross-wind distribution. The influence of the windbreak on the up-and downwind pollen concentration can be expressed as:

$$\beta_c(x, z_s) = \frac{c_1(x, z_s)}{c_0(z_s)}, \quad (3)$$

where x denotes the longitudinal position in relation to the windbreak location (see Fig. 2), z_s is a specified height above ground and c_1 denotes the pollen concentration field downwind of c_0 ,

i.e. in the area surrounding the windbreak in the up- and downwind direction. β_c indicates the modification of pollen concentration at a certain position in the domain in relation to the far upwind pollen concentration at the corresponding height, which results from the combined effects of wind field disturbance and filtering. The total impact of the shelterbelt on pollen distribution can be estimated based on observations of c_0 and c_1 . This is only true, however, if the downwind concentration field is un-biased by particles that are not related to c_0 . In the present case of a birch stand, however, the shelterbelt does not only act as a pollen sink due to filtering, but also as a pollen source, which contributes to the concentration field in the downwind domain. Note that c_1 and, consequently, β_c are a function of the spatial position in the area around the shelterbelt. In order to estimate the impact of the shelterbelt on particle distribution without the unwanted emission term and thus independently of c_1 , a numerical model was used to simulate pollen trajectories with a stochastic Lagrangian approach in a flow field driven by a RANS model. Since neither particle deposition nor a particle source within the canopy is implemented in the model, it only accounts for the effect of wind field distortion. The deposition part is thus estimated with a second model based on the parameterisation of pollen impaction and the optical porosity of the windbreak. With respect to the individual windbreak effects, β_c can be expressed as:

$$\beta_c(x, z_s) = \sigma_p(z_s) \omega(x, z_s), \quad (4)$$

where σ_p denotes the transmissivity factor related to filtering and ω accounts for the effect of wind field distortion on particle dispersion, which will be named wind field effect. ω describes the portion of upwind concentration that arrives in the sheltered area (see Section *Wind field effect* ω). σ_p describes the fraction of upwind particles, which are not affected by deposition and thus emerge from the downwind face of the windbreak. Conversely, the particle deposition rate within the windbreak can be expressed as $1 - \sigma_p$. The filtering effect of the present windbreak is estimated based on a parameterisation from the literature (see the following section).

Windbreak transmissivity σ_p

The transmissivity of a windbreak is inversely related to its filtering effect. Particles are filtered from the particle plume by a natural windbreak if the collision with a vegetation obstacle or the deceleration of its velocity results in deposition, i.e. entrapment of the particle within the canopy. For the case of particle impact on vegetation surface, Paw U (1983) found a critical 'rebound' velocity (U_c) as function of the adhesion force field between the particle and the impinging surface. If the particle velocity is below U_c before impact, the particle is deposited. In the case of thick windbreaks with low porosity such as maize Bouvet et al. (2007) implemented U_c in a dispersion model for glass beads, where vegetation elements are represented with a parameter for the probability of impaction. In the present study, particle velocity is modified as function of the drag coefficient of the canopy, which is described by the leaf-area density, and vegetation elements are not actually accounted for. For ragweed pollen, which are similar to birch pollen in terms of shape, diameter and mass, Paw U (1983) found a critical rebound velocity of 2.87 ms^{-1} . Applying U_c to the CFD-simulated particle velocities (see Section *CFD model*) would yield a large deposition rate for low velocities, which seems highly improbable in regard of the high windbreak porosity. For thin windbreaks Raupach et al. (2001) found a simple empirical estimation of the particle transmissivity σ_p based on the optical porosity of the windbreak and the turbulent motion through the canopy. For the case of birch pollen, σ_p can be expressed as:

$$\sigma_p = \kappa^{mE}, \quad (5)$$

where κ is the optical porosity, E denotes the impaction efficiency of particles on obstacles and m denotes the ratio of the meandering distance across the windbreak to its width.



Figure 3: View on the north face of the windbreak with the upwind mast T_1 .

A common empirical definition of the impaction efficiency is:

$$E = \left(\frac{St}{St + p_s} \right)^{q_s}, \quad (6)$$

where p_s and q_s are dimensionless coefficients, for which Peters and Eiden (1992) found $p_s = 0.8$ and $q_s = 2$, which are valid for different obstacle shapes. St is the Stokes number, which describes the motion of particles in relation to its surrounding fluid. It is defined as:

$$St = \left(\frac{\rho_p d^2}{18\mu} \right) \left(\frac{\delta}{\bar{U}} \right)^{-1}, \quad (7)$$

where ρ_p is the particle density, μ is the dynamic molecular viscosity of air and δ is the characteristic size of the obstacle element. The average obstacle length $\delta = 0.02$ m was determined with manual measurements of branches and leaves. For the estimation of the meandering factor Raupach et al. (2001) propose a parameterisation using the upwind turbulence intensity, expressed as:

$$m = \left(1 + I_u^2 + I_v^2 + I_w^2 \right)^{1/2}, \quad (8)$$

where $I_{u,v,w}$ are the turbulence intensities of the three wind components, which can be calculated from the measurements via $I_j = \sigma_j/\bar{U}$, where σ is the standard deviation and the subscript j denotes the wind component. The optical porosity κ is defined as the proportion of background visible through the canopy (Loeffler et al., 1992; Vigiak et al., 2003). A photograph of the windbreak (see Fig. 3 and Appendix C) was used to determine the vertical profile $\kappa(z)$, where z denotes the height above ground. Raupach et al. (2001) derived a modification of κ as function of wind velocity, which accounts for streamlining of the vegetation elements in strong wind. Since the wind velocity was rather low during the measurement period, the effect of streamlining is neglected in the calculation of the windbreak transmissivity. With the impaction efficiency of birch pollen (Eq. 6) and the meandering factor (Eq. 8) being known from the sonic measurements, the transmissivity can be calculated. Note that for cases, when $z > h$, the transmissivity is defined as $\sigma_p(z) = 1$. The filtering effect as function of z is applied to the CFD-simulated pollen dispersion via $1 - \sigma_p(z)$, which defines the probability of trapping for a single particle entering the windbreak at a certain height z , which is deposited within the canopy, i.e. does not emerge from the downwind face of the windbreak. Particle deposition is applied to the model results by ignoring the trajectories of a certain fraction $1 - \sigma_p(z)$ of randomly chosen particles at the moment they cross the upwind face of the windbreak at $x = -30$ m and at the height z . This simplified method, however, does not account for an increasing deposition rate across the longitudinal extent of the windbreak, which might be expected under natural conditions. Since κ is a one-dimensional (i.e. vertical) porosity

scale and thus provides no information on variability in the along-wind direction, σ_p can not be a function of x . Therefore, $1 - \sigma_p$ describes the filtering effect as the ratio of the number of particles emerging from the downwind face of the windbreak to the number of particles entering the upwind face.

Wind field effect ω

The wind field in the surrounding area up- and downwind and its influence on particle dispersion was simulated with a CFD model in order to estimate the effect of the windbreak on the pollen concentration field c_1 , when filtering is neglected. Based on Eq. 3, ω can be expressed as:

$$\omega = \frac{c_1 |_{\sigma_p = 1}}{c_0}, \quad (9)$$

where the condition $|\sigma_p = 1$ determines that no deposition occurs within the windbreak and c_1 is modified by the wind field distortion only.

CFD model

CFD simulations are able to simulate turbulent flows over ground including complex topography. The area of interest is divided by a grid, based on which the Navier-Stokes-Equations (NSE) are discretised and solved. The CFD simulations were performed for different velocity classes and windbreak widths using the open-source OpenFOAM (Open Field Operation and Manipulation) software package (OpenFOAM Foundation, 2014). For the present work the solver *simpleFOAM* was used for the wind field simulation. For the particle simulation the solver *uncoupledKinematicParcelFOAM* has been adapted (Gartmann, 2012).

Governing equations

The NSE describe the physics of liquids and gases in motion and can be written for incompressible fluids as

$$\frac{DU_i}{Dt} = -\frac{1}{\rho} \frac{\delta p}{\delta x_i} + f_i + \mu \frac{\delta^2 U_i}{\delta x_j^2}, \quad (10)$$

where U_i are the velocity components in three dimensions, f_i the body force per unit mass, ρ the density and μ the dynamic viscosity (Versteeg and Malalasekera, 2007). The continuity equation for incompressible flows is defined as:

$$\frac{\partial U_i}{\partial x_i} = \nabla \cdot \mathbf{U} = 0 \quad (11)$$

Incompressible flows are characterized by very low Mach numbers. The term 'incompressible' thus describes a property of flow and not a fluid property.

Turbulence modelling

A very common turbulent model approach is obtained by applying the Reynolds Decomposition (Eq. 12) to the NSE (Eq. 10)

$$U_i = \langle U_i \rangle + u_i, \quad (12)$$

which leads to the RANS equations:

$$\frac{\bar{D}\langle U_i \rangle}{\bar{D}t} = -\frac{1}{\rho} \frac{\partial \langle p \rangle}{\partial x_i} + f_i + \nu \frac{\partial^2 \langle U_i \rangle}{\partial x_i^2} - \frac{\partial \langle u_i u_j \rangle}{\partial x_j} \quad (13)$$

The additional terms $\frac{\partial \langle u_i u_j \rangle}{\partial x_j}$ denote Reynolds stresses and are crucial to turbulence modelling using the RANS method. By applying the turbulent-viscosity hypothesis, a proportional relation between the Reynolds stresses and the mean rate of strain can be derived. The scalar coefficient of the ratio is the turbulent viscosity ν_t .

$$\langle u_i u_j \rangle = \frac{2}{3} k \delta_{ij} - \nu_t \left(\frac{\partial \langle U_i \rangle}{\partial x_j} + \frac{\partial \langle U_j \rangle}{\partial x_i} \right), \quad (14)$$

where k is the turbulent kinetic energy (TKE) $k = \frac{1}{2} \langle u_i u_i \rangle$. Two-equation models are among the more evolved methods to compute the turbulent viscosity. There is a wide range of approaches (Pope, 2000), of which the k - ϵ model is the most commonly used model in engineering applications. It solves two transport equations for k and dissipation ϵ . The turbulent viscosity can then be obtained via:

$$\nu_t = C_\mu \frac{k^2}{\epsilon}, \quad (15)$$

where $C_\mu = 0.09$ is a model parameter. The Reynolds stresses (Eq. 14) are determined based on ν_t and the NSE can be calculated.

Incorporation of vegetation effects

The effects of vegetation on the flow field can be incorporated in the CFD calculations by adding an additional source term in the governing equations (Kobayashi et al., 1994). The vegetation canopy effects the reduction of momentum from the flow and production of turbulent kinetic energy (Wilson and Shaw, 1977). The reduction of momentum can be achieved by adding the following source term to the RANS:

$$S_{u,i} = \frac{1}{\rho} \frac{\partial p}{\partial x} = C_d \alpha |U| U_i, \quad (16)$$

where C_d is the drag coefficient and α denotes the leaf-area density. Both parameters are dependent on the vegetation canopy. Lalic and Mihailovic (2004) propose an empirical model for α in forest canopies based on the height z_m and magnitude of the maximum leaf-area density α_m . Iterative CFD calculations were performed to determine these parameters for the birch stand on the basis of measured wind profiles and typical values of the drag coefficient C_d , which yielded $\alpha_m = 0.2$ and $z_m/h = 0.7$. The numerically derived value of α_m corresponds to the findings of Stadt and Lieffers (2000) for birch trees, which suggest the range 0.042 to 0.222, depending on the flowering phase. For the understorey, $\alpha = 0.75$ is assumed. Following Sanz (2003), the turbulent kinetic transport equation can be modelled with the source term of k :

$$S_k = C_d \alpha [\beta_p |U_i|^3 - \beta_d k |U_i|], \quad (17)$$

where $\beta_p \in [0, 1]$ is the transfer coefficient of turbulent energy production by the mean velocity and β_d the coefficient for the TKE breakdown. Furthermore, the source term for the dissipation is:

$$S_\epsilon = \frac{C_d \alpha}{2} \left[C_{\epsilon 4} \beta_p \frac{\epsilon}{k} |U_i|^3 - C_{\epsilon 5} \beta_d |U_i| \epsilon \right], \quad (18)$$

where $C_{\epsilon 4}$ and $C_{\epsilon 5}$ are model parameters. Based on the relationship between k and ϵ , Sanz (2003) derived Eq. 19 from the transport equation of the k - ϵ model:

$$\beta_d = C_\mu^{1/2} \left(\frac{2}{v} \right)^{2/3} \beta_p + \frac{3}{\sigma_k} \quad (19)$$

$$C_{\epsilon 4} = \sigma_k \left[\frac{2}{\sigma_\epsilon} - \frac{\sqrt{C_\mu}}{6} \left(\frac{2}{v} \right)^{2/3} (C_{\epsilon 2} - C_{\epsilon 1}) \right], \quad (20)$$

Table 1: Summary of the used model parameters

$C_{\epsilon 1}$	$C_{\epsilon 2}$	β_p	β_d	<i>std</i> $C_{\epsilon 4}/C_{\epsilon 5}$	<i>real</i> $C_{\epsilon 4}/C_{\epsilon 5}$	v
0.43	1.9	1.0	6.508	1.352	1.6502	0.05

std denotes parameters used in the the standard $k - \epsilon$ model and *real* denotes parameters used in the realizable model.

where v is a dimensionless coefficient independent of the vegetation characteristics and σ_k and σ_ϵ denote the standard deviations of k and ϵ , respectively. $C_{\epsilon 1}$ and $C_{\epsilon 2}$ are model parameters. The parameters used for the turbulence simulation are summarised in Table 1.

Lagrangian particle dispersion modelling

A Lagrangian approach was applied to simulate pollen dispersion. Newton's Second Law postulates the following relation for a falling particle in the air (Shao, 2008):

$$\rho_p V \frac{\partial U_{i,p}}{\partial t} = -\rho_f \frac{\pi d^2}{8} C_{dp} (U_{ip} - U_i) |U_{i,p} - U_i| + Vg(\rho_p - \rho_f), \quad (21)$$

where the subscript p denotes particle properties and the subscript f denotes properties of the gaseous fluid. $g = 9.81 \text{ ms}^{-2}$ is the acceleration due to gravity, V denotes the volume and d the particle diameter. Equation (21) can be rearranged to:

$$\frac{\partial U_{i,p}}{\partial t} = -\frac{U_{i,p} - U_i}{\tau} + F \quad (22)$$

with the particle response time τ (Shao, 2008):

$$\tau = \frac{8\rho_p V}{\pi\rho_f C_{dp} d^2 |U_{i,p} - U_i|}, \quad (23)$$

F abbreviates the forces of gravity and lift. The particle aerodynamic drag coefficient is dependent on the particle Reynolds number Re_p (Shao, 2008) and modelled using the *SphereModel* of OpenFOAM, which incorporates the following relations:

$$Re_p = \frac{|U_{i,p} - U_i|d}{\nu_f} \ll 1 : C_{dp} = \frac{24}{Re_p} \quad (24)$$

$$0 \ll Re_p < 1000 : C_{dp} = \frac{24}{Re_p} \left(1 + \frac{1}{6} Re_p^{2/3}\right) \quad (25)$$

$$Re_p > 1000 : C_{dp} = 0.424 \quad (26)$$

The trajectories of the particles, i.e. pollen, are not only influenced by the mean velocity components U_i , but also by the turbulence behaviour of the gaseous fluid (Fritsching, 2004). The influence of the turbulence on the particle trajectories is modelled according to Sommerfeld (1992). The basic idea is that turbulence influences the particle path during a defined time period τ_i , which precisely corresponds to the time the particle is influenced by one eddy, before the influence of another eddy begins. The time period τ_i is defined as:

$$\tau_i = \frac{L_t}{|U_{i,p} - U_i|}, \quad (27)$$

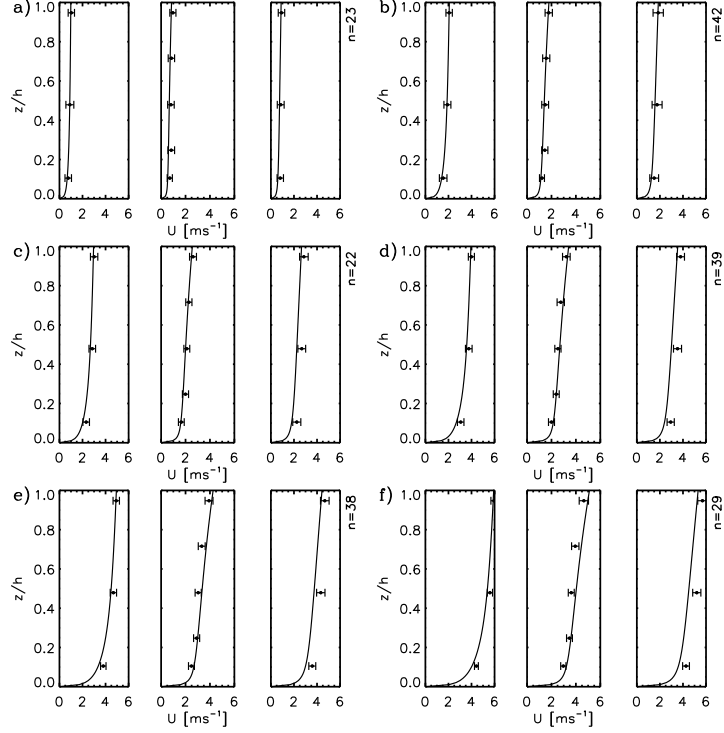


Figure 4: Agreement of modelled (solid lines) and averages of measured 10-minute wind velocities (dots) for 1 - 6 ms^{-1} (panels a - f) at 20 m upwind (left) 100 m downwind (middle) and 350 m downwind (right) of the windbreak in the case of normal approach with a threshold of $\pm 10^\circ$. n denotes the sample size of each velocity class with respect to its threshold. One simulation run was performed per velocity class. The horizontal lines denote the standard deviations of the measured wind velocities. The wind velocity observed 20 m upwind of the windbreak at 18 m height was used to determine the corresponding velocity class.

where L_t is the Lagrangian integral time scale of the turbulence according to Sommerfeld (1992), expressed as:

$$L_t = c_i \frac{k}{\epsilon}, \quad (28)$$

where $c_i = 0.3$ is an empirically derived parameter. The fluctuating velocities are sampled using a Gaussian distribution with a standard deviation of an isotropic turbulence field $u_i = \sqrt{2k/3}$ (Gjesing et al., 2009). The turbulence is included through:

$$U_{i,new} = U_i + U_i \mathcal{R} \sqrt{2k/3}, \quad (29)$$

where the subscript *new* defines the updated velocity field and \mathcal{R} is a random number. Using the trajectory information of every particle, analyses of the particle concentration distribution can be made with respect to the source location based on the model runs 1-6 ms^{-1} .

CFD set-up

In order to assess the influence of edge effects on the particle dispersion behind the windbreak, the wind field around the shelterbelt was simulated with a focus on cross-wind variations using three-dimensional runs of the wind flow simulations. The results indicated that the downwind sensor array is not affected by effects induced at the lateral edges, which could have an influence

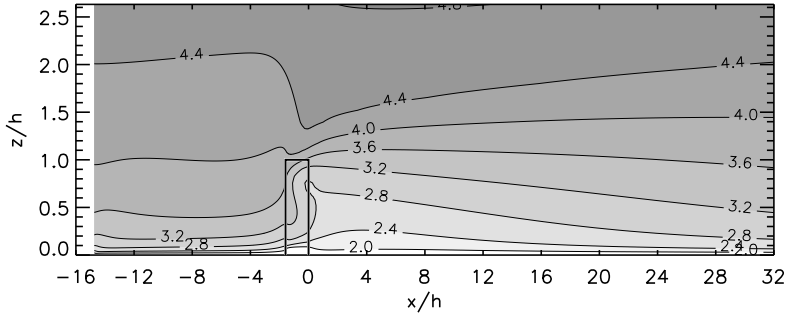


Figure 5: Lateral view of the simulated wind field around the windbreak calculated for the case of 4 ms^{-1} at $z = 18 \text{ m}$ at the upwind model boundary. The contour lines denote the wind velocity in ms^{-1} . The bold solid square denotes the outline of the windbreak.

on concentrations. Hence, the lateral dimension of the windbreak facing the oncoming free stream in relation to the downwind array of sensors is large enough to be assumed as infinite. The model is thus constricted to two dimensions along the center-line of the model domain with a length of 1000 m in the longitudinal and 100 m in the vertical direction. The windbreak with the height $h = 19 \text{ m}$ was located in a distance of 250 m from the inlet boundary in order to ensure undisturbed flow conditions upwind of the canopy. The mesh consisted of 50 elements in the vertical direction with a spacing of 2 m. The ratio from near-ground to top mesh cell was 1:50 in order to obtain a higher mesh resolution near the ground. The inflow velocity boundary condition was based on the profile according to Richards and Hoxey (1993). The aerodynamic roughness length (z_0) was converted to the roughness height according Blocken et al. (2007) for the ground roughness property. The vegetation density in the windbreak was incorporated by an additional field with the leaf-area density obtained from an empirical function for birch trees (Lalic and Mihailovic, 2004).

Since the actual shape of the profile $c_0(z)$ is mostly unknown except for the observations at 2 m and 18 m, a uniform far upwind source profile c_{0u} is assumed in order to simulate undisturbed conditions. Taking into account non-stationary wind conditions, ω is a function of wind velocity. The model is thus run for six velocity classes, i.e. 1, 2, 3, 4, 5 and 6 ms^{-1} , which correspond to the range of measured upwind velocity during favourable conditions. The wind field runs were forced by a logarithmic wind profile $U_i(z)$ at the upwind model boundary, where the velocity at 18 m height was used as the reference for the velocity class. The initial wind profile is defined as:

$$U_i(z) = \frac{u_*}{k'} \ln \left(\frac{z}{z_0} \right), \quad (30)$$

where k' is the von Kármán constant and the roughness length $z_0 = 0.01 \text{ m}$ is assumed for the bare soil in the fetch area. The specific friction velocity u_* for a particular velocity class was calculated based on the corresponding upwind reference value at T_1 , e.g. $U_i(18 \text{ m}) = 1 \text{ ms}^{-1}$ for the 1 ms^{-1} velocity class. The incorporated width of the windbreak used for the six velocity classes corresponds to the actual width $w_s = 30 \text{ m}$. In order to assess the influence of windbreak width on particle dispersion, two additional runs for $U = 4 \text{ ms}^{-1}$ are performed with a windbreak width of $w_s = 15 \text{ m}$ and $w_s = 60 \text{ m}$, respectively (see Section *Parameterisation CFD-based pollen transport*). Figure 4 shows that the modelled wind profiles agree well with the observations at the three towers. The mean deviations of all heights and all velocity classes lie well between -0.5 ms^{-1} and 0.5 ms^{-1} . The calculations for the velocity were steady-state, which were used as initial fields for the transient particle dispersion. The convergence criteria for the iteratively solved velocity fields were set to normalised residuals lower than 10^{-5} ms^{-1} . Based on the small spherical particle diameter ($d = 23 \mu\text{m}$), the particle calculations were coupled one-way: the flow field could influence the trajectories, but the particles did not influence the flow properties.

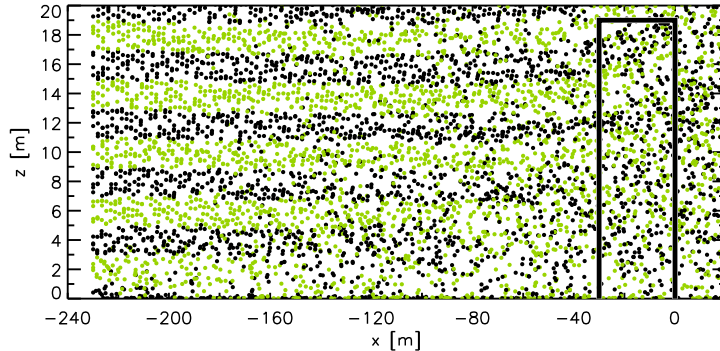


Figure 6: Lateral view of the simulated particle distribution in the 4 ms^{-1} wind class for a single 'snapshot' in the equilibrium state (every 30^{th} particle shown). The particle colour alternates with respective release height. The bold square denotes the outline of the windbreak.

The particles are introduced from a vertical source array consisting of 16 point sources in the undisturbed region at $x=-230 \text{ m}$ (or $x/h=-12.1$, respectively, see Fig. 5). The lowest source point was located at a height of 0.5 m , the higher source points were set at 2 to 30 m with a separation distance of 2 m .

As mentioned above, a uniform upwind concentration profile c_{0u} is used to describe the inlet conditions. It is defined as $c_{0u}=67 \text{ pollen m}^{-2}$. In order to obtain this vertically uniform concentration field at the inlet under neutral wind conditions characterised by the logarithmic wind profile, the strength of the point sources $Q(z)$ in the undisturbed upwind region was defined via:

$$Q(z) = \frac{c_{0u} U(z)}{b}, \quad (31)$$

where b denotes the height of the bin around the source points, i.e. 2 m , except for $b=1 \text{ m}$ in the case of the lowest source point. The total number of particles emitted in a single run as function of the velocity class can be approximated with $n_p = 1 \cdot 10^6 \text{ pollen/ms}^{-1} \cdot U$.

In order to achieve well-mixed conditions of the particle distribution right from the start, the release height from each source was statistically distributed within the bin length (Fig. 6). The field of particle concentration is calculated by using the box-counting method with a grid consisting of cells of 10 m length and 2 m height. In order to achieve stationary conditions of the particle transport, the model runtime with continuous particle emission was 1500 s in the case of the velocity classes 1 to 3 ms^{-1} and 1000 s in the case of the velocity classes 4 to 6 ms^{-1} with a temporal resolution of 1 s . During stationary periods, i.e. when the particle transport from the upwind to downwind boundary was steady, the number of particles in each box at each timestep was counted. The average from the samples during the timesteps within the equilibrium period was used to obtain the concentration field. The model analysis was restricted to the area between the particle inlet and up to 500 m downwind of the windbreak and from the ground to a height of 30 m , which was large enough to capture the pollen dispersion patterns in the experimental array. Figure 5 shows how the logarithmic velocity profile of the oncoming flow is disturbed as it moves through the windbreak. Deceleration of wind starts upwind of the canopy and already reaches its maximum at the downwind face of the windbreak. At a distance of $x/h = 32$, the influence of the disturbance is still visible, yet the profile has almost returned to the logarithmic shape. The influence of the windbreak on the flow is still substantial for heights $z/h > 2$, i.e. $>38 \text{ m}$. The source profile was limited to the height, from where the amount of released particles arriving at the downwind sensors near the ground is less than one percent, i.e. $z = 30 \text{ m}$. The contribution of individual source points on the downwind area decreases with increasing height above the canopy, because turbulent motions become less important above the windbreak and the settling of particles depends mostly on gravity. Figure 7 shows that for low wind velocities, i.e. when the longitudinal displacement of

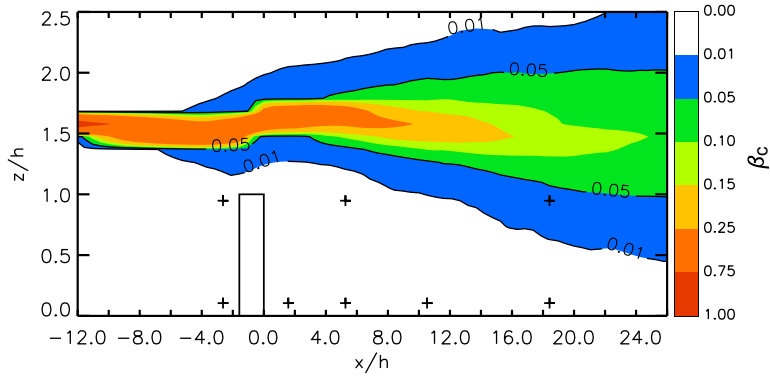


Figure 7: Modelled fraction of the inlet particle concentration for the velocity class 1 ms^{-1} if only one single source height (30 m) is analysed. The square denotes the outline of the windbreak. Plus signs indicate the positions of the Burkard measurements.

settling particles is smallest, less than one percent of the particles released from the highest source point arrive at the farthest observation point near the ground and less than five percent arrive at the corresponding observation point at 18 m.

Results

Pollen transmissivity of the canopy

The pollen transmissivity of the windbreak is calculated for all velocity classes with respect to the optical porosity (Eq. 5). For each class, a logarithmic initial wind profile is assumed, according to Eq. 30. The vertical profiles of porosity and transmissivity are inversely related to the vertical profile of foliage density. Therefore, σ_p based on the measured optical porosity is compared to the leaf-area density used in the numerical simulation. Figure 8 shows that the height z/h of the lowest pollen transmissivity within the crown area ($z/h > 0.25$), which is based on the optical porosity, coincides well with the height of the maximum leaf-area density $z_m/h = 0.7$, which was derived from the CFD calculations. In the case of birch trees, Lalic and Mihailovic (2004) found $z_m/h = 0.8$. The transmissivity is also compared to the windbreak porosity P , which is defined as the volume of air in relation to the total volume of the stand. Gross (1993) provides a function $\alpha = f(P)$, which can be solved numerically for P , if α is known. The rather high transmissivity calculated with Eq. 5 seems reasonable in perspective of the high porosity. Note that in Fig. 8 the understorey is only considered for σ_p , since α is derived from a generic function, as mentioned above. The optical porosity of the grass understorey ranges from zero to 0.03 and is thus considered impermeable for particles.

The uncertainty of the transmissivity is sensitive mainly to the assumed value of the obstacle length scale δ . An increase from the used 0.02 to 0.04 m generates an increase of $\bar{\sigma}_p(z)$ from 0.89 to 0.95 in the case of a wind velocity of 6 ms^{-1} . Using $\delta = 0.002$, e.g. for a coniferous canopy with the same optical porosity, $\bar{\sigma}_p(z)$ would decrease to approximately 0.5 in the case of a wind velocity of 6 ms^{-1} . Thus, it can be stated that the deposition within a birch stand with an optical porosity similar to the present windbreak is generally low and less important compared to coniferous stands. Figure 8 also shows the effect of wind velocity on particle transmissivity. It is larger for low wind velocities and lower for high wind velocities. This relation is explained by Eq. 6 and 7, where the impaction efficiency E increases with wind velocity: The higher the particle velocity, the stronger

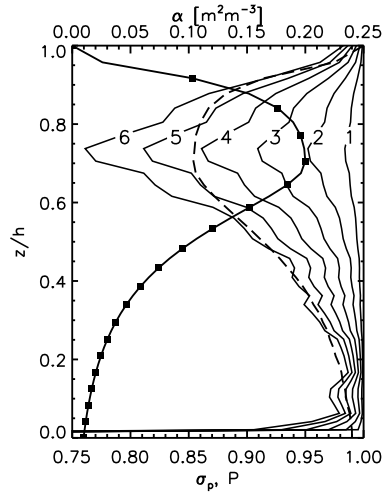


Figure 8: Pollen transmissivity σ_p through the windbreak for different velocity classes (solid lines) calculated via Eq. 5. The numbers denote the velocity class in ms^{-1} . Within the understorey ($z/h < 0.04$), the pollen transmissivity is approximately zero. The dashed line denotes the windbreak porosity (P). The solid lines with squares denote the leaf-area density (α).

the tendency of the airborne particles to maintain their initial direction and deviate from the diverging fluid trajectories upwind of the obstacle, which results in impaction. In the case of the used filtering model, impaction equals deposition. In general, it can be stated that the total pollen transmissivity of the thin windbreak is very high for the velocity classes used in the present work. The strongest filtering effect of the windbreak is associated to the denser crown area. However, for very low velocities ($U \leq 1 \text{ ms}^{-1}$) the filtering effect is almost negligible. For higher velocities, i.e. 6 ms^{-1} , almost 25% of the particles are filtered at z_m . Within the trunk space, deposition is very low (i.e. a transmissivity of $>95\%$), regardless of the wind velocity.

Results of the numerical simulations

The effect of the windbreak on the up- and downwind concentration field is strongly dependent on the velocity of the oncoming flow, resulting in an increase or decrease of pollen concentration up- and downwind of the shelterbelt. Figure 9 shows the simulated field of ω and β_c , i.e. without and with filtering, based on the uniform inlet concentration profile for the velocity classes 1 ms^{-1} and 5 ms^{-1} . In the case of low wind velocities (panel *a*) the downwind concentrations are largely increased due to accumulation, which is induced by deceleration of the flow in the windbreak. Compared to the upwind concentration at the same height, the downwind concentrations near the ground reach values of up to 134%. Right behind the windbreak accumulation builds up a high-concentration layer, which imbeds the observation points at 2 m above the ground. The turbulence is relatively weak in this velocity class, so that a large portion of the pollen can settle to the ground and is not mixed into higher regions. As the stream velocity increases, accumulation is weaker due to stronger turbulent mixing in the downwind area (panel *c*). Hence, in the case of the velocity class of 5 ms^{-1} and near the ground, the downwind concentrations are lower than upwind, i.e. 75%. The reduction of the accumulation layer with increasing wind velocity is shown in Appendix A.

The effect of the leaf-area density profile $\alpha(z)$ on the stream velocity and thus pollen concentration is clearly visible for all velocity classes (Fig. 9 and A.1). At around the height $z/h = 0.7$, a layer of higher downwind concentrations is generated due to higher foliage density, which decelerates the

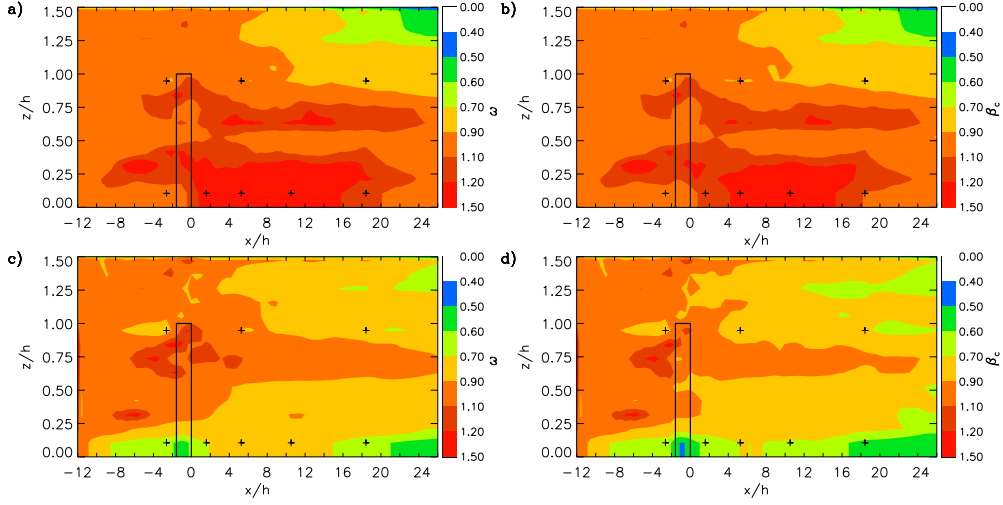


Figure 9: Modelled field of pollen concentration around the windbreak normalised by a vertically uniform inlet concentration ($\beta_c = c_1/c_{0u}$) for the velocity class 1 ms^{-1} (top row) and 5 ms^{-1} (bottom row). The panels on the left show the relative concentration field ω based purely on wind field effects. The panels on the right show the relative concentration field β_c resulting from the combined effects of wind field disturbance and particle trapping. The square denotes the outline of the windbreak. Plus signs indicate the positions of the Burkard measurements.

wind flow at this level. The observations at 18 m, however, are not as strongly affected by accumulation as the measurements near the ground, since higher velocities from above the windbreak are entrained, which mitigates the deceleration at this level. The banking of the wind flow upwind of the shelterbelt results in an updraft of the oncoming particle stream near the ground, as it flows around the canopy. This results in regions of lower concentrations near the ground. On the other hand, upwind regions of higher concentration are generated, where the trajectories of the lifted pollen converge. In the case of higher velocities, this effect is more pronounced (panel *c*).

Figures 9*b* and 9*d* show how the filtering effect of the windbreak increases with increasing wind velocity due to the higher impaction efficiency. While the downwind concentration is not significantly reduced by deposition within the canopy in the case of wind velocities around 1 ms^{-1} (panel *b*), the effect is more pronounced in the case of higher velocities (panel *d*). Pollen travelling through the windbreak at around $z/h = 0.7$, i.e. at the maximum thickness of the foliage, are more affected by filtering than pollen crossing in the trunk space. The increase of the filtering effect with increasing wind velocity is shown in more detail in Fig. A.1.

Note that the 'reference' upwind observations of the oncoming pollen field are also substantially influenced by the windbreak. The lower and upper sensor are both located in regions of divergence, i.e. in regions with lower pollen concentration than in the undisturbed conditions further upwind.

Validation of modelled actual pollen concentrations

The actual pollen concentration field c_1 is sensitive to the shape of the undisturbed background concentration profile, which is not necessarily uniform under natural conditions. The pollen dispersion resulting from the CFD simulations is, therefore, analysed with respect to non-uniform background concentration profiles, as observed at the upwind tower T_1 . From here on, the non-uniform background concentration c_0 as function of height is thus used instead of c_{0u} . Since the trajectories of all particles are known from the Lagrangian dispersion approach, the contribution of each individual source to any point in the domain can be determined. This allows to derive the

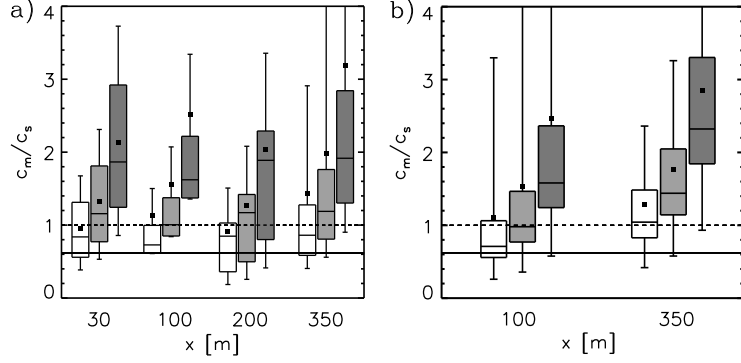


Figure 10: Variability of the ratio between measured c_m and simulated c_s pollen concentration behind the windbreak in the case of wind directed normally to the windbreak with a threshold of $\pm 10^\circ$. The sample consists of 18 cases. *a)* data of measurements at 2 m height and *b)* data of measurements at 18 m height. The background concentration was calculated with respect to the range of sensor uncertainty ($\pm 38\%$) according to Michel et al. (2012): upper limit of the uncertainty range (white), lower limit (dark grey), no alteration (light grey). Squares denote the mean value, horizontal lines denote the median, vertical lines denote the spread between the 0.05 and 0.95 percentile, respectively. The shaded area denotes the spread of the 0.25 and 0.75 percentile, respectively. The solid line denotes the lower range of data within the sensor uncertainty.

virtual emission ϕ of undisturbed background concentration c_0 . The fraction ϕ at each position in the domain can be estimated by summing all the particles coming from a particular height and dividing by the number of particles released at the corresponding height. Introducing height ranges or bins (z_q) then yield:

$$c_1(x, z) = \sum_{i=1}^{n_z} \phi(x, z, z_{qi}) c_0(z_{qi}) \sigma_p(z_{qi}), \quad (32)$$

where n_z denotes the number of bins in the background concentration profile, i.e. $n_z = 16$ for the present CFD-source profile from 1 to 30 m with bins of 1 and 2 m, respectively.

The CFD simulations of β_c have shown that the upwind tower T_1 is located within a disturbed region upwind of the shelterbelt (see Fig. 9). The observations of pollen concentration at T_1 , which will be named c_{T_1} , thus do not represent the true undisturbed upwind concentration c_0 . Therefore, the actual *undisturbed* far upwind concentration profile $c_0(z)$ is estimated by extrapolating the measured upwind concentration observations via $c_0 = 1/\beta_c$ with β_c at $x = -50$ m and $z = 2$ m and $z = 18$ m, respectively. In response to the stationary wind direction in the two-dimensional CFD model, pollen measurements at the upwind tower T_1 are only accepted for analysis during situations, when the wind is directed normally to the windbreak with a threshold of $\pm 10^\circ$ and wind velocities larger than 0.5 ms^{-1} .

The measurements of the oncoming pollen field revealed that the upwind profile is non-uniform in most cases. The ratio of the upper to lower concentrations (c_u/c_l) ranges from 0.7 to 4.7 with an average ratio of 3.1, which indicates that the concentration at 18 m is mostly higher than near the ground.

On the downwind side, the validation of the model with measured data must rely on the observation of total concentration, without the knowledge of the additional emission part. A good agreement of simulation and observation can theoretically only be expected in the case of zero emission from the birch stand. The plausibility of the simulation is thus assessed with the assumption that the ratio of measured concentration c_m to simulated concentration c_s should be $c_m/c_s \geq 1$. Consequently, $c_m/c_s = 1$ ideally describes situations with zero emission from the birch stand.

The model performance is assessed with respect to the uncertainty of the measurements. The relative precision error of Burkard pollen traps in the case of birch pollen is substantial ($\pm 38\%$)

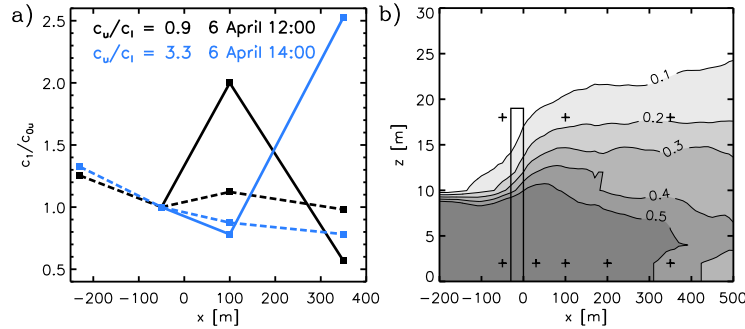


Figure 11: a) Pollen concentration measured (solid lines) and modelled (dashed lines) at the towers T_{1-3} in relation to the concentration c_{T1} measured at the upwind tower for the cases of a vertical profile ratio of upper to lower measurement $c_u/c_l = 0.9$ (black) on 6 April 12 UTC+1 and $c_u/c_l = 3.3$ (blue) on 6 April 14 UTC+1. b) Modelled field β_c of pollen concentration normalised by the inlet concentration for the velocity class 2.0 ms^{-1} in the case of release below 10m only. The square denotes the outline of the windbreak. Plus signs indicate the positions of the Burkard measurements.

according to the findings of the sensor inter-comparison field experiment by (Michel et al., 2012). The precision error is taken into account in the model validation by applying the precision error to c_s , i.e. $0.62c_s$ and $1.38c_s$, which thereon represent the validity range of the observations. Consequently, also lower validity threshold for situations with zero emission reduces to $c_m/c_s = 0.62$ instead of $c_m/c_s = 1$. Figure 10 shows that in most cases the measured concentrations are larger than the simulated background concentration, even in the case of the largest positive uncertainty. The performance of the model is also assessed with respect to different patterns of vertical pollen concentration profiles, as they move through the windbreak. The example in Fig. 11a shows that if the measured pollen concentration at the upper sensor is higher than near the ground, i.e. $c_u/c_l > 1$, the concentration at 18 m height and 100 m behind the windbreak is lower than upwind. If the ratio of upper to lower observation is $c_u/c_l < 1$, the downwind concentration is higher than upwind. This specific correlation of vertical ratio to longitudinal ratio at the upper sensors is an effect which is typical for the entire data series. In both cases, the measured pattern of longitudinal increase/decrease as function of the vertical ratio is reproduced.

Figure 11b shows how the effect of the upwind profile to the downwind concentration is related to the turbulent mixing of pollen behind the canopy. In the case of $c_u/c_l < 1$, few pollen from the upper upwind level contribute to the downwind area and a larger amount from the lower upwind region contributes to the upper level. The total of horizontally and vertically transported pollen then results in an increase at 18 m above the ground and 100 m behind the windbreak, compared to the same height upwind. In the case of $c_u/c_l > 1$ (not shown), the downwind concentration 100 m behind the windbreak is decreased at the upper sensor position, because it is mixed with the less disturbed stream above the canopy, as mentioned above. When the pollen concentration is low near the ground, only few pollen are lifted up to this region.

Sensitivity to non-stationary conditions

Micrometeorological observations in a natural environment are often characterised by a large variability due to non-stationary conditions. Near-stationary conditions of a variable during a measurement interval can be achieved by using a high temporal resolution. The field observations in the present study indicate substantial variability of wind conditions and pollen concentrations in the case of a one- and two-hourly resolution. The sensitivity of the agreement between modelled and measured data is assessed with respect to variable wind direction and pollen concentration. Figure 12a shows an example of the modelled concentration and measured concentration in the

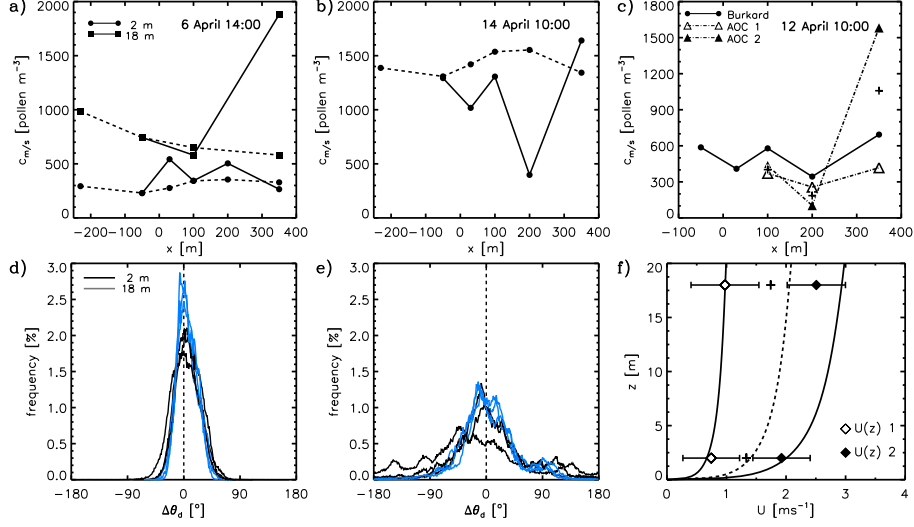


Figure 12: The left column (panels *a* and *d*) shows the longitudinal variability of pollen concentrations and the frequency distribution of wind direction at T_{1-3} in a height of 2 and 18 m, respectively, for April 6 2010 12-14 UTC+1. The middle column (panels *b* and *e*) shows the same for April 14 2010 8-10 UTC+1. In panels *a* and *b* solid lines denote Burkard observations and the dashed lines denote modelled pollen concentrations. Dots denote data at 2 m height, squares denote data at 18 m height. The right column (panels *c* and *f*) shows longitudinal Burkard and AOC observations at 2 m height along the center-line of the downwind area and the corresponding measured and modelled wind velocity profiles at the upwind tower T_1 . In panel *c* the solid lines denote two-hourly Burkard data and the dashed lines denote one-hourly AOC data. For AOC data, empty triangles correspond to the first (1) and filled triangles correspond to the second half (2) of the two-hour measurement interval. Plus signs denote the two-hour averages of AOC data. In panel *f* the solid lines denote the modelled wind profiles and diamonds denote the average of measured wind velocities. Horizontal lines denote the standard deviation of the measured wind velocity for the corresponding one-hour interval. The blue dashed line denotes the two-hour average wind profile.

case of persistent wind direction normal to the windbreak (see panel *d*). The amount of observed concentration exceeding the modelled concentration can thus be associated to emission from the birch stand. In the case of the large variability of the wind direction shown in panel *e*, which on average fulfills the requirement of a normal approach, the simulation largely overestimates the concentration at 18 m (panel *b*). Note that the situation at 2 m is not shown here. When the flow approaches the downwind area from a lateral or opposite direction ($|\Delta\theta_a| \geq 90^\circ$), the windbreak has no effect on the natural pollen distribution in the instrumental array, resulting in lower concentrations, which explains the discrepancy between modelled and measured data.

The effect of non-stationary wind velocity and pollen concentration is demonstrated in Fig. 12*c* based on the hourly AOC observations. The average of the nearest AOCs east and west of the center-line are used, when the spatial variability of pollen concentrations is assumed to be low within the lateral distance of < 33 m and these AOC observations are comparable to the Burkard data. The AOC data indicate that the variability of the measured pollen concentration can be substantial within a two-hour interval. This variability is averaged out in the two-hourly Burkard data. The difference of the two consecutive intervals of one hour increases with distance from the windbreak. Figure 12*f* clearly shows the influence of wind velocity on the longitudinal decrease rate of concentration due to settling, as mentioned above.

Temporal variations of the upwind pollen concentration within the two-hour interval might also have a substantial influence on the observed downwind concentration. However, observations of the oncoming pollen stream is limited to the two-hour Burkard measurements. Therefore, temporal variations of the upwind pollen concentration could not be monitored.

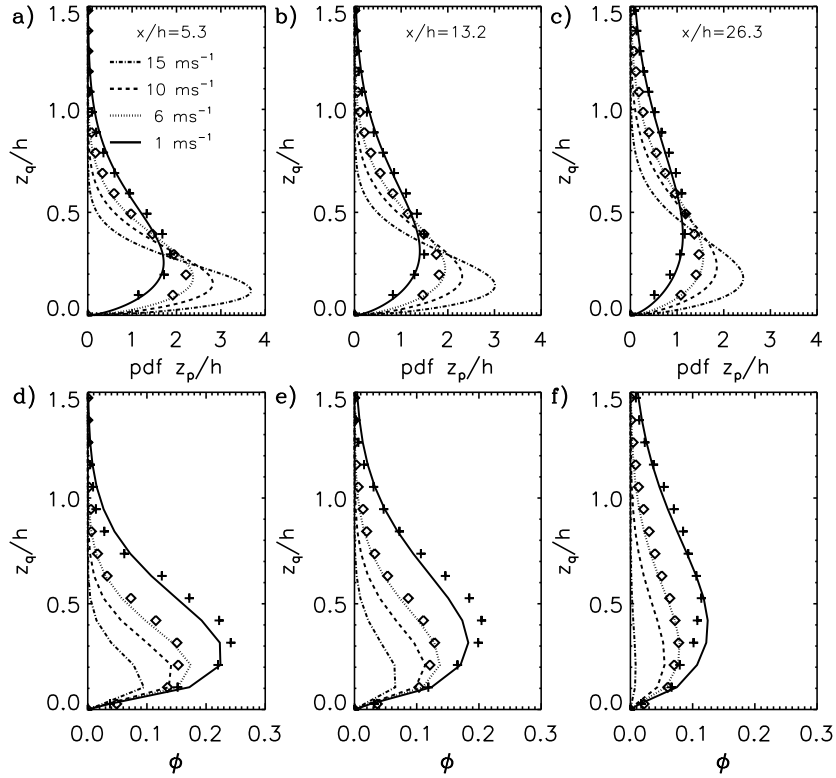


Figure 13: *Top row:* Probability density of the particle release height as function of wind velocity and longitudinal distance from the windbreak at 2 m above ground. *Bottom row:* Virtual emission ϕ as function of wind velocity and longitudinal distance from the windbreak at 2 m above ground. Note that for both parameters the pollen transmissivity $\sigma_p = 1$ is assumed. The lines denote model data, diamonds denote the discrete parameterised profile for the 1 ms^{-1} wind class, plus signs denote the discrete parameterised profile for the 6 ms^{-1} wind class. The distance from the windbreak increases from left to right.

Parameterisation of CFD-based pollen transport

In the context of both operational or experimental observations of atmospheric pollen concentrations, it is important to eliminate the problem of disturbance due to obstacles in the surrounding area, or to quantify its influence. In terms of a brief evaluation of the conditions in a given environment, the use of a numerical simulation may be unpractical. In order to provide a simple estimate of the dispersion of particles similar to birch pollen, the results of the CFD simulations are parameterised. Since the model respects very specific conditions, i.e. pollen size and windbreak characteristics, the parameterisation is valid only for particles with a diameter of around $23 \mu\text{m}$ and for natural windbreaks with a porosity corresponding to the canopy described in the present study, as well as for distances from the windbreak of up to $x/h = 26.3$, which corresponds to the length of the model domain. The parameterisation is also limited to 2 m above the ground, since this is a standard height for pollen observations.

The parameterisation of ω is based on the vertical footprint of the downwind concentration c_1 . It denotes the probability density of the height z_p in the undisturbed background profile of pollen, which contribute to a certain location behind the windbreak. The vertical footprint of any point in the model domain was determined by fitting the corresponding histogram of the CFD-based discrete z_p/h for all positions and velocity classes. The probability densities as function of z/h can

be described by a continuous Weibull (Weibull, 1951) probability density function (pdf), which is only based on wind velocity, longitudinal distance from the windbreak, a shape factor (k_w) and a scale factor (λ). Integrating the pdf of z_p/h over a certain vertical range thus yields the probability ϕ_P of particles originating from the chosen vertical section in the background concentration profile and contributing to c_1 behind the windbreak. The parameterisation of ϕ_P with the Weibull pdf normalised with h can be expressed as:

$$\phi_P(z_q) = \int_{z_1}^{z_2} \left[\frac{k_w}{\lambda} \left(\frac{z_q/h}{\lambda} \right)^{k_w-1} e^{-\left(\frac{z_q/h}{\lambda}\right)^{k_w}} \right] dz_q, \quad (33)$$

where z_1 is defined as $z_q - b/2$ and z_2 is defined as $z_q + b/2$ and thus denote the lower and upper limit of the bin around the respective height z_q . Curve-fitting of ϕ_P for all velocity classes and distances from the windbreak with the Weibull function indicated that the density function is sensitive to variations of the scale factor only and variations of the shape factor can thus be neglected. The best fit of the Weibull function to the frequency of $z_p(z/h)$ with a constant shape factor was obtained using $k_w = 1.65$. The dependence of the scale factor λ on U and x was determined by using the constant k_w and fitting the Weibull pdf to the frequency of $z_p(z/h)$. The best results were obtained with an exponential function:

$$\lambda = e^{\left[(0.17 \frac{x}{h}) / \left(\frac{x}{h} \right)^{0.54} \right]} \lambda_0, \quad (34)$$

where λ_0 is a scaling factor as function of velocity:

$$\begin{aligned} \lambda_0(U) &= 0.36 - 0.05 U \quad 1 \text{ ms}^{-1} \leq U \leq 2 \text{ ms}^{-1} \\ &= 0.27 - 0.009 U \quad U > 2 \text{ ms}^{-1} \end{aligned} \quad (35)$$

Note that $\phi_P(z_q)$ indicates the *probability distribution* of virtual pollen emission as function of height and not the actual virtual emission. ϕ , however, is directly proportional to ϕ_P , and can be calculated via:

$$\phi(z_q) = \phi_P(z_q) r_f, \quad (36)$$

where $r_f = r_{f_i} + r_{f_s}$ accounts for the proportionality between ϕ and ϕ_P . The best results for r_{f_i} and r_{f_s} were found using linear fitting. The term r_{f_i} is used to scale ϕ_P with respect to wind velocity:

$$\begin{aligned} r_{f_i}(U) &= 1.52 - 0.37 U \quad 1 \text{ ms}^{-1} \leq U \leq 2 \text{ ms}^{-1} \\ &= 0.89 - 0.05 U \quad U > 2 \text{ ms}^{-1} \end{aligned} \quad (37)$$

r_{f_s} accounts for the distance from the windbreak and can be approximated with a third order polynomial of x/h :

$$r_{f_s}(x/h) = 0.04 \frac{x}{h} - 0.003 \left(\frac{x}{h} \right)^2 + 6.4 \cdot 10^{-5} \left(\frac{x}{h} \right)^3 \quad (38)$$

Once the profile $\phi(z_q)$ is determined, the absolute particle concentration c_1 can be calculated via Eq. 32.

With increasing distance from the source, more particles from higher regions contribute to the concentration near the ground, which results in a larger vertical spread of the density function (see Fig. 13a-c). The linear form of Eq. 37 allows to apply wind velocities, which are larger than the classes addressed with the CFD model. In contrast to the effect of distance, increasing wind velocity reduces the vertical spread, because particles from higher regions travel further in the same time interval. Hence, particles are less effectively transported to lower regions by gravitational settling and turbulent mixing. The fitted Weibull function agrees very well with the results of the simulation. The use of the scaling factor r_f on the Weibull function integrated over the bin size

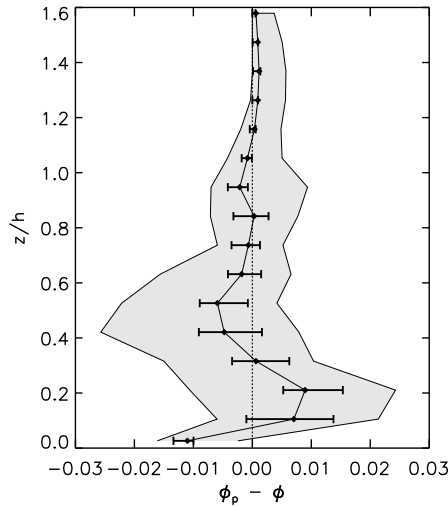


Figure 14: Distribution of the deviation of parameterised virtual emission ϕ_p from CFD-based ϕ vertical profiles as function of z_q/h with respect to all velocity classes and distances from the windbreak. Diamonds denote the mean value, horizontal lines denote the spread between the 0.25 and 0.75 percentile, respectively. The shaded area denotes the spread of the 0.05 and 0.95 percentile, respectively.

(Fig. 13d-f) results in higher values of $\phi(z_q/h)$ for lower wind velocities, since the contribution of each height to any location x/h near the ground increases, because the effect of gravitational settling becomes more important. In the case of high wind velocities, e.g. 15 ms^{-1} , settling is less important and ϕ becomes small. Fig. 13f shows that for $U = 15 \text{ ms}^{-1}$ only few particles are observed at $x/h = 26.3$ in relation to the upwind profile, because settling to the ground is reduced by the high velocity. Note, however, that $\phi(z_q/h)$ is a relative estimate of the vertical footprint of a concentration profile. Thus, if the background concentration is very large, the actual concentration at this point could still be substantial.

In order to assess the performance of the parameterisation of ϕ , its equations are solved using the height z , longitudinal distance x , wind velocity U and bin size b according to the CFD set-up, which yields ϕ_p . It is compared to ϕ derived from the model results taking into account all wind velocity classes and values of x against the vertical profiles. Figure 14 shows that the average absolute deviation of the parameterised profiles $\phi_p(z_q/h)$ from $\phi(z_q/h)$ is smaller than 0.01. This corresponds to an average under- or overestimation of one percent of the portion of the particles, which originate from a certain height and contribute to c_1 . The deviation decreases with increasing height, since the wind flow is less disturbed around the top of the canopy, in contrast to regions near the ground. In order to estimate the validity range of the parameterisation in terms of the fixed windbreak width, the sensitivity of the simulated pollen distribution to the width of the windbreak is assessed (Fig. 15). Note that the leaf-area density remains the same for all cases. Differences of the pollen dispersion thus result solely from enhanced or reduced turbulence in the canopy due to the canopy thickness. Effects of the windbreak width on the dispersion are investigated with half (15 m) and double (60 m) the original width (30 m), respectively. The ratios of the resulting normalised concentration fields based on a uniform background profile are shown with respect to the longitudinal distance. The data are scattered between a ratio of 0.8 and 1.2, which indicates that the influence of the windbreak is not uniform for different heights and distances from the windbreak. In general, a smaller windbreak width results in mostly higher concentrations (and hence larger ω) and a wider windbreak results in lower concentrations (and smaller ω) behind the canopy in comparison to the situation with the original windbreak. The median of the vertical range of ratios in regard of the longitudinal locations indicates that the pollen concentration directly behind a thinner windbreak is lower in comparison to the situation with the original windbreak and that

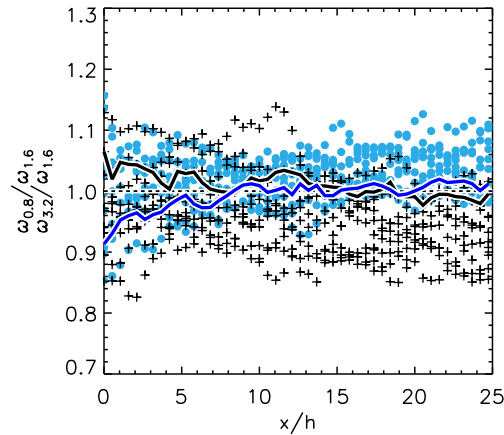


Figure 15: Normalised modelled concentration without respect to filtering in the case of a windbreak width of $w_s/h = 0.8$ (blue dots) and $w_s/h = 3.2$ (plus sign), respectively, in relation to the standard width of $w_s/h = 1.6$, with respect to height (2 to 10 m above the ground) and distance from the windbreak. The used velocity class is 4 ms^{-1} . The blue line denotes the median of the entire vertical profile (0 to 30 m) in the case of $w_s/h = 0.8$, the black line denotes the median of the entire vertical profile in the case of $w_s/h = 3.2$.

the concentration slightly increases with distance and eventually exceeds the pollen concentration in the case of the smaller windbreak width. This effect is related to higher wind velocities, which mitigate the accumulation right behind the canopy and move the pollen further away, where they eventually settle to the ground. In the case of a larger canopy width, accumulation is favoured near the downwind edge due to stronger deceleration. Consequently, the concentration is slightly lower in the distance, because a certain amount is already deposited in the accumulation area behind the windbreak. In general, however, it can be stated that the influence of the windbreak width on pollen dispersion is not substantial within the range of the tested canopy thickness and is therefore neglected in this parameterisation.

Conclusions

Observations up- and downwind of a pollen-emitting birch canopy aimed at inferring its emission strength as function of meteorological conditions and with a high temporal resolution. A CFD model was used to quantify the bias of the readings due to background concentration, which is influenced by the shelter effect of the canopy. For the validation of particle models in a disturbed wind field, monitoring the initial conditions of the wind field and particle distribution is crucial in order to get the source strength right. This is of particular importance, when simulations are assessed in a natural environment. In order to minimise the uncertainty induced by natural variability of particle concentration, corresponding experiments are thus usually performed by using controllable artificial sources and particles. The present study illustrates the difficulty of calibrating and validating particle dispersion simulations, when both particle emission and wind conditions are largely variable. The observations of birch pollen concentrations and wind flow have indicated that non-stationary source strength and meteorological conditions in a two-hourly interval, especially wind direction, strongly impede the prediction of pollen dispersion. Even in the case of rather steady conditions, as found in a mountain-valley system, short gusts of pollen from different wind directions can result in substantially different readings of pollen samplers compared to the model.

However, the CFD simulations were able to reproduce certain observed patterns, which are related to the shape of the vertical background concentration profile and changes of wind direction. Note that the validation of the simulations would benefit from a higher temporal resolution of pollen measurements, which would allow a more detailed assessment of model accuracy based on shorter events. However, available and operational pollen sensors can only provide a higher resolution at the expense of accuracy. The findings allow to attest the model a certain degree of plausibility. The simulations thus give insight into phenomena, which can be of interest for experimental and operational monitoring sites in areas characterised by wind flow distortion due to large roughness elements: The concentration field around a porous windbreak is altered by the combined effects of pollen filtering within and deceleration of the wind flow in the downwind area. Both effects are dependent on the upwind velocity of the freestream and are counteracting. Low freestream velocities result in lower pollen deposition on vegetation elements, while accumulation behind the canopy is favoured. With increasing wind velocity, filtering gets stronger, whereas pollen tend to be carried further away, resulting in a more homogeneous and lower concentration in the downwind area. In the case of the thin and rather porous birch canopy, the influence of the filtering effect on pollen dispersion is always substantially smaller than the wind field effect. Deceleration and divergence of the flow crossing the canopy result also in a distortion of the upwind pollen concentration field, up to a distance of more than the canopy height. The CFD simulations with respect to the settling velocity of the heavy birch pollen have shown that the wind field effect is still detectable several hundreds of meters downwind.

The analyses of the numerical simulations highlighted the benefit of using a trajectory-based Lagrangian approach, where the position of each particle, i.e. also its origin, can be monitored. In contrast to a grid-based Eulerian model, this allows a more detailed investigation of the pollen transport and a focus on the connections between wind field and particle dispersion. This was of special importance in the present study, where the initial conditions to force the model were largely unknown. The information on particle trajectories also allowed to establish a parameterisation of the pollen dispersion, which agrees very well with the model data for the case of pollen concentrations near the ground. Although the applicability of the parameterisation is limited to thin shelterbelts of broadleaf trees, it may be useful to understand and estimate the combined effects of filtering and windbreak without the use of a model.

The approach of estimating the natural particle emission of an isolated source with a high temporal resolution on the base of downwind observations is very straightforward and can be successful if an capable dispersion model is used. The measurements in this study have shown, however, that any influence of background concentration should be avoided, since it is hardly possible to take the variability of upwind conditions into account.

Acknowledgements

Our great appreciation goes to the European Cooperation in Science and Technology (COST) Action ES0603. The financial support for this project by the Swiss State Secretariat for Education and Research (SBF), grant C07.0111, and the Freiwillige Akademische Gesellschaft Basel, is gratefully acknowledged. Many thanks go to MeteoSwiss and the MCR Lab, University of Basel. Their contribution to the field campaigns and the pollen analysis is highly appreciated.

References

- Aylor, D. and Flesch, T. (2001), ‘Estimating spore release rates using a Lagrangian stochastic simulation model’, *J. App. Meteorol.* **40**, 1196–1208.
- Aylor, D. and Qiu, J. (1996), ‘Micrometeorological determination of release rate of *Venturia inaequalis* ascospores from a groundlevel source during rain’, *Agr. Forest Meteorol.* **81**, 157–178.
- Bache, D. (1981), ‘Analysing particulate deposition to plant canopies’, *Atmos. Envir.* **15**, 1759–1761.
- Blocken, B., Stathopoulos, T. and Carmeliet, J. (2007), ‘CFD simulation of the atmospheric boundary layer: wall function problems’, *Atmospheric Environment* **41**, 238–252.
- Boehm, M. and Aylor, D. (2005), ‘Lagrangian stochastic modeling of heavy particle transport in the convective boundary layer’, *Atmos. Environ.* **39**, 4841–4850.
- Bouvet, T., Loubet, B., Wilson, J. and Tuzet, A. (2007), ‘Filtering of windborne particles by a natural windbreak’, *Bound.-Lay. Meteorol.* **123**, 481–509.
- Cai, X., Zhang, R. and Li, Y. (2006), ‘A large-eddy simulation and lagrangian stochastic study of heavy particle dispersion in the convective boundary layer’, *Bound.-Lay. Meteorol.* **120**, 413–435.
- Cleugh, H. (1998), ‘Effects of windbreaks on airflow, microclimates and crop yields’, *Agroforestry Systems* **41**, 55–84.
- Cleugh, H. (2002), ‘Field measurements of windbreak effects on airflow, turbulent exchange and microclimates’, *Australian Journal of Experimental Agriculture* **42**, 665–677.
- De Haan, P. (1999), ‘On the use of density kernels for concentration estimations within particle and puff dispersion models’, *Atmos. Envir.* **33**, 2007–2021.
- Dunnet, S. and Ingham, D. (1986), ‘A mathematical theory to two-dimensional blunt body sampling’, *J. Aerosol Sci.* **17**, 839–853.
- Frenz, D. (1999), ‘Comparing pollen and spore counts collected with the Rotorod sampler and Burkard spore trap’, *Ann. Allergy Asthma Immunol.* **83**, 341–347.
- Fritsching, U. (2004), *Spray Simulation*, Cambridge University Press.
- Gartmann, A. (2012), CFD methods in the atmospheric roughness layer at different scales, PhD thesis, University of Basel, Switzerland.
- Gjesing, R., Hattel, J. and Fritsching, U. (2009), ‘Coupled atomization and spray modelling in the spray forming process using openFOAM’, *Engineering Applications of Computational Fluid Mechanics* **3**, 471–486.
- Gregory, P., Longhurst, T. and Sreeramulu, T. (1961), ‘Dispersion and deposition of airborne *Lycopodium* and *Ganoderma* spores’, *Ann. Appl. Biol.* **49**, 645–658.
- Gross, G. (1993), *Numerical simulation of canopy flows*, Springer, Berlin.
- Guo, L. and Maghirang, R. (2012), ‘Numerical simulation of airflow and particle collection by vegetative barriers’, *Enginee* **6**, 110–122.
- Hirst, J. (1952), ‘An automatic volumetric spore trap’, *Ann. Appl. Biol.* **39**, 257–265.

- Ingham, D. (1981), 'The entrance of airborne particles into a blunt sampling head', *J. Aerosol Sci.* **12**, 541–549.
- Jarosz, N., Loubet, B., Durand, B., McCartney, A., Foueillassar, X. and Huber, L. (2003), 'Field measurements of airborne concentration and deposition rate of maize pollen', *Agr. Forest Meteorol.* **119**, 37–51.
- Jarosz, N., Loubet, B. and Huber, L. (2004), 'Modelling airborne concentration and deposition rate of maize pollen', *Atmos. Envir.* **38**, 5555–5566.
- Kobayashi, M., Pereira, J. and Siqueira, M. (1994), 'Numerical study of the turbulent flow over and in a model forest on a 2d hill', *Journal of Wind Engineering & Industrial Aerodynamics* **53**, 357–374.
- Lacey, M. and West, J. (2006), *The Air Spora: A manual for catching and identifying airborne biological particles*, Springer, Dordrecht.
- Lalic, B. and Mihailovic, D. (2004), 'An empirical relation describing leaf-area density inside the forest for environmental modeling', *J. App. Meteor.* **43**, 641–645.
- Levetin, E. (2004), 'Methods for aeroallergen sampling', *Current Allergy and Asthma Reports* **4**, 376–383.
- Loeffler, A., Gordon, A. and Gillespie, T. (1992), 'Optical porosity and windspeed reduction by coniferous windbreaks in southern Ontario', *Agro* **17**, 119–133.
- Mandrioli, P., Comtois, P. and Levizzani, V. (1998), *Methods in aerobiology*, Pitagora Editrice, Bologna, Italy.
- May, K. (1945), 'The Cascade Impactor: An instrument for sampling coarse aerosols', *J. Sci. Instrum.* **22**, 187–195.
- McNaughton, K. (1988), 'Effects of windbreaks on turbulent transport and microclimate', *Agriculture, Ecosystems and Environment* **22/23**, 17–39.
- Mercer, G. (2009), 'Modelling to determine the optimal porosity of shelterbelts for the capture of agricultural spray drift', *Environmental modelling & software* **24**, 1349–1352.
- Michel, D., Gehrig, R., Rotach, M. and Vogt, R. (2010), MicroPoem: Experimental investigation of birch pollen emission, in '19th Symposium on Boundary Layer and Turbulence, Keystone, Colorado, 2 - 8 August'.
- Michel, D., Rotach, M., Gehrig, R. and Vogt, R. (2012), 'On the efficiency and correction of vertically oriented blunt bioaerosol samplers in moving air', *Int. J. Biometeorol.* **56**, 1113–1121.
- Ogden, E., Raynor, G., Hayes, J., Lewis, D. and Haines, J. (1974), *Manual for sampling airborne pollen*, Hafner Press, New York.
- OpenFOAM Foundation (2014), *OpenFOAM. The open source CFD toolbox. User guide*.
- Paw U, K. (1983), 'The rebound of particles from natural surfaces', *J. Colloid Interface. Sci.* **93**, 442–452.
- Peters, K. and Eiden, R. (1992), 'Modelling the dry deposition velocity of aerosol particles to a spruce forest', *Atmosph. Environ.* **26**, 2555–2564.

- Petroff, A., Mailliat, A., Amielh, M. and Anselmet, F. (2008), 'Aerosol dry deposition on vegetative canopies. Part II: A new modelling approach and applications', *Atm* **42**, 3654–3683.
- Petroff, A., Zhang, L., Pryor, S. and Belot, Y. (2009), 'An extended dry deposition model for aerosols onto broadleaf canopies', *Aerosol Science* **40**, 218–240.
- Pope, S. B. (2000), *Turbulent Flows*, Cambridge University Press.
- Raupach, M., Woods, N., Dorr, G., Leys, J. and Cleugh, H. (2001), 'The entrapment of particles by windbreaks', *Atmos. Envir.* **35**, 3373–3383.
- Raynor, G. (1972), 'An isokinetic sampler for use on light aircraft', *Atmos. Envir.* **6**, 191–196.
- Reynolds, A. (2000), 'On the formulation of Lagrangian stochastic models for heavy-particle trajectories', *J. Colloid Interface Sci.* **232**, 260–268.
- Richards, P. and Hoxey, R. (1993), 'Appropriate boundary conditions for computational wind engineering models using the k- ϵ turbulence model', *Journal of Wind Engineering and Industrial Aerodynamics* **46 and 47**, 145–153.
- Rosenfeld, M., Marom, G. and Bitan, A. (2010), 'Numerical simulation of the airflow across trees in a windbreak', *Bound.-Lay. Meteorol.* **135**, 89–107.
- Santiago, J., Martín, F., Cuerva, A., Bezdeneznykh, N. and Sanz-Andrés, A. (2007), 'Experimental and numerical study of wind flow behind windbreaks', *Atmospheric Environment* **41**, 6406–6420.
- Sanz, C. (2003), 'A note on k- ϵ modelling of vegetation canopy air-flows', *Boundary-Layer Meteorology* **108**, 191–197.
- Shao, Y. (2008), *Physics and modelling of wind erosion*, 2nd revised and expanded edn, Springer.
- Skoner, D. (2001), 'Allergic rhinitis: definition, epidemiology, pathophysiology, detection and diagnosis', *J. Allergy Clin. Immunol.* **108(Suppl.)**, 2–8.
- Sommerfeld, M. (1992), 'Modelling of particle-wall collisions in confined gas-particle flows', *International Journal of Multiphase Flow* **18(6)**, 905–926.
- Stadt, K. and Lieffers, V. (2000), 'MIXLIGHT: a flexible light transmission model for mixed-species forest stands', *Agr. Forest Meteorol.* **102**, 235–252.
- Tsai, P. and Vincent, J. (1993), 'Impaction model for the aspiration efficiencies of aerosol samplers at large angles with respect to the wind', *J. Aerosol Sci.* **24**, 919–928.
- Versteeg, H. and Malalasekera, W. (2007), *An introduction to Computational Fluid Dynamics*, second edn, Longman Scientific & Technical.
- Vigiak, O., Sterk, G., Warren, A. and Hagen, J. (2003), 'Spatial modeling of wind speed around windbreaks', *Catena* **52**, 273–288.
- Vincent, J. (2007), *Aerosol Sampling: Science, Standards, Instrumentation and Applications*, John Wiley & Sons, Ltd., Chichester.
- Vincent, J., Hutson, D. and Mark, D. (1982), 'The nature of air flow near the inlets of blunt dust sampling probes', *Atmos. Envir.* **16**, 1243–1249.
- Vincent, J. and Mark, D. (1982), Applications of blunt sampler theory to the definition and measurement of inhalable dust, in W. Walton, ed., 'Inhaled Particles V', Pergamon Press, Oxford, pp. 3–19.

- Watson, H. (1954), ‘Errors due to anisokinetic sampling of aerosols’, *Am. Ind. Hyg. Assoc. Q.* **15**, 21–25.
- Weibull, W. (1951), ‘A statistical distribution function of wide applicability’, *J. Appl. Mechanics* **18**, 293–297.
- Wenneker, M., Heijne, B. and Van De Zande, J. C. (2005), ‘Effect of natural windbreaks on drift reduction in orchard spraying’, *Commun. Agric. Appl. Biol. Sci.* **70**, 961–969.
- Wilson, J. (1985), ‘Numerical studies of flow through a windbreak’, *Journal of Wind Engineering and Industrial Aerodynamics* **21**, 119–154.
- Wilson, J. (2000), ‘Trajectory models for heavy particles in atmospheric turbulence: Comparison with observations’, *J. Appl. Meteorol.* **39**, 1894–1912.
- Wilson, N. R. and Shaw, R. H. (1977), ‘A higher order closure model for canopy flow’, *J. of Appl. Meteorol.* pp. 1197–1205.

Appendix A Effect of wind velocity on pollen dispersion

Figure A.1 shows how the effect of accumulation near the ground is reduced with increasing wind velocity. The effect of the thickness at the height of maximum leaf-area density is clearly visible in all velocity classes, resulting in higher pollen concentrations at that height due to stronger deceleration. The increasing filtering strength of the windbreak with increasing wind velocity is indicated in the case of the 6 ms^{-1} velocity class (panel *f*, where the largest discrepancies between ω and β_c are observed). The scattered regions shown in panel *f* result from the problem of grid resolution in relation to the wind velocity. In the case of high wind velocities, certain particles skip a box from one timestep to another due to their velocity, which yields lower concentrations in the simulation at this particular point. This effect is explained in e.g. De Haan (1999).

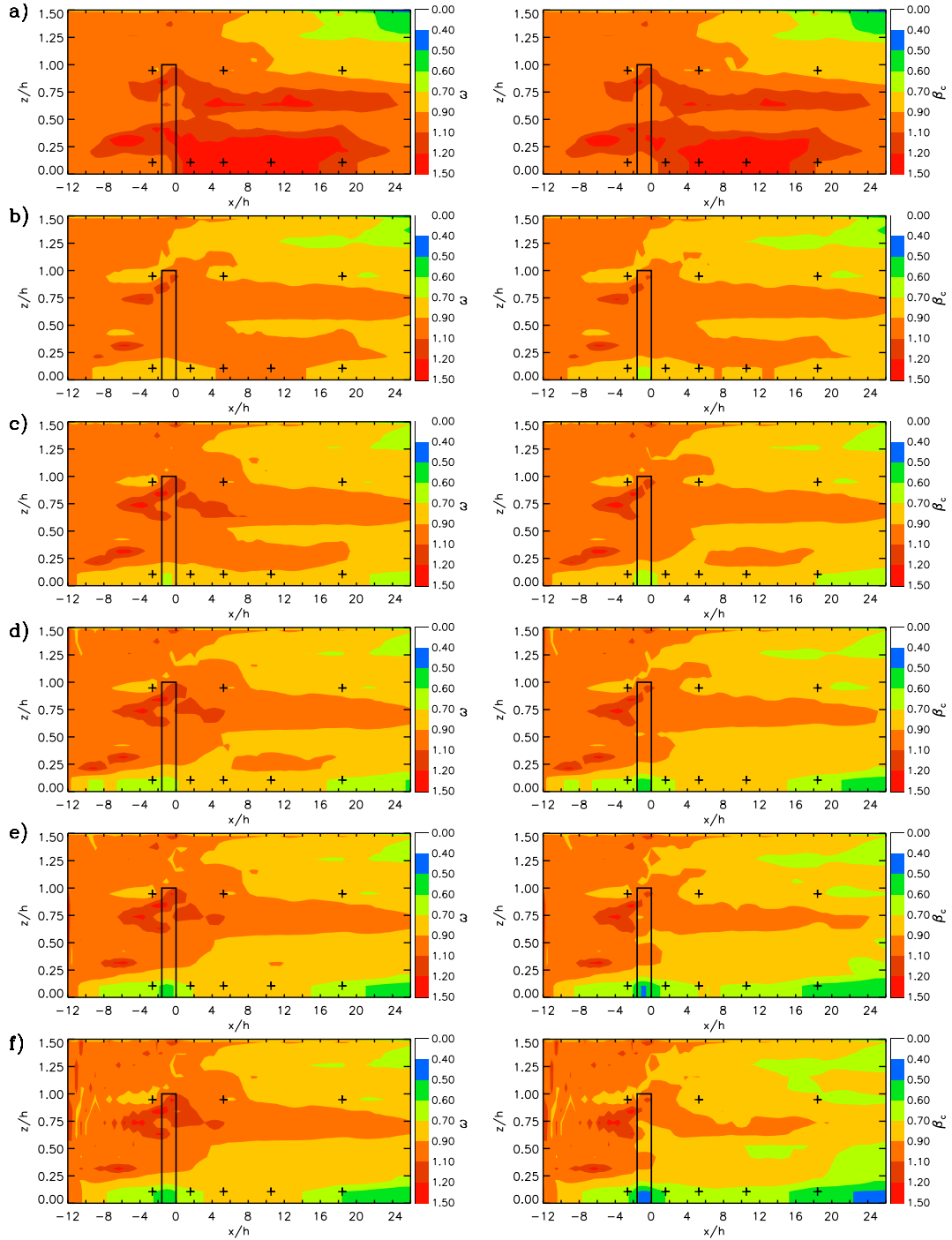


Figure A.1: Modelled field of pollen concentration around the windbreak normalised by a vertically uniform inlet concentration ($\beta_c = c_1/c_{0u}$) for the velocity class 1 ms^{-1} through 6 ms^{-1} (a-f). The plots on the left show the relative concentration field based purely on wind field effects. The plots on the right show the relative concentration field resulting from the combined effects of wind field disturbance and particle trapping. The square denotes the outline of the windbreak. Plus signs indicate the positions of the Burkard measurements.

5.3 Set-up of the source characteristics in the CFD model

The results in Section 5.2 show that the observations upwind of the windbreak are already influenced by the banking effect of the canopy on the oncoming wind flow. Several approaches of implementing particle release into the model domain have been tested with focus on achieving well-mixed conditions well before the location of the upwind sensors, in order to be able to quantify the disturbance in relation to the uniform case. Figure 5.1 indicates that introducing the particles at the exact longitudinal position of the sensors results in mixed conditions only behind the shelterbelt due to production of mechanical turbulence. If the particles are introduced further upwind, e.g. 100 m in front of the windbreak, the induced turbulence is visible, yet the sources are still too close to the canopy to react to the turbulent conditions. If the particles are released 200 m upwind of the windbreak, the boundary layer building up to the canopy is indicated by a region of higher turbulence near the ground. However, the pollen trajectories are mostly identical for several timesteps after their release, until turbulence is large enough to initiate random dispersion. The cases of identical particle trajectories are associated to undisturbed conditions, where the vertical profile of background concentration is transported more or less in its original shape. This corresponds to the uniform normalised distribution upwind of the canopy, shown in Fig. P2-9 and P2-A.1 in the paper P2 (Section 5.2). Only near the ground well-mixed conditions are induced due to friction. The distance that a particle travels without new turbulent input, is dependent on the time period τ_i , which denotes the time a particle is influenced by one eddy. The downward trend of the trajectories in the undisturbed regions behind the release points relates to the settling velocity of the pollen.

The concentration of simulated particles is highly sensitive to the applied cell grid, when the particle counting method is applied. In the case of a vertical point source profile, derived concentrations are sensitive mostly to the height of the cells. If the cells are too small, i.e. smaller than the vertical spacing of the point sources, concentration distribution becomes scattered, if turbulence is low and the cell lies between two particle streams. If the grid cells are too large, i.e. larger than the vertical spacing of the sources, spatial variability is oversmoothed (De Haan, 1999). Therefore, the particle dispersion presented in Section 5.2 (Fig. P2-6) is based on the same point sources as in Fig. 5.1c, yet with a randomly distributed source height per bin. The wind velocity acting on a released particle, however, is equal to the velocity at the 'real' source height. Since the maximum height difference is 1 m only, this effect is neglected in order to achieve well-mixed conditions at the particle inlet.

5.4 Estimating background concentration based on spatial uniformity

The original plan in the present study was to infer the pollen emission directly from observations downwind of the windbreak with respect to the background concentration obtained at the tower T_1 . The background concentration had been assumed to be more or less uniform in the longitudinal direction and to vary only with height above ground. In Section 5.2 it is demonstrated, however, that the pollen dispersion in the up- and downwind area is substantially modified by the windbreak. The modelled concentration is normalised with the undisturbed initial background concentration c_0 , which yields β_c . The results have shown that the observations of the upwind sensors at T_1 , which aimed at determining the level of background concentration, are in fact biased due to the barrier effect of the shelterbelt. Using these distorted upwind observations as a reference for initial concentrations for the numerical simulations would thus result in inaccurate downwind concentrations. Therefore, the uncertainty of predicted downwind concentrations in the case of assumed longitudinal uniformity of background concentration is assessed.

β_c represents a *normalised* pollen distribution, which relates concentrations to the background

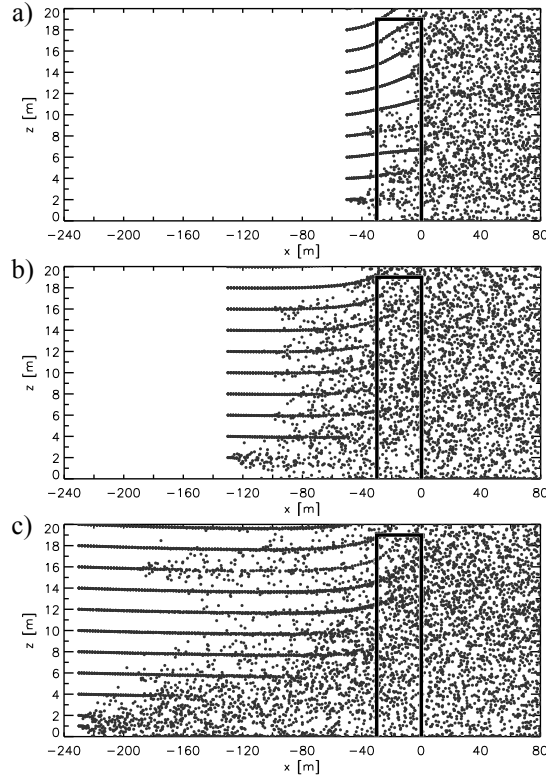


Figure 5.1: Different approaches of implementing particle release at the point sources. *a)* Stationary release conditions 20m upwind of the windbreak at 15 point sources from 2 to 30m with a vertical separation of 2m. *b)* Stationary release conditions 100m ($x = -130\text{ m}$) upwind of the windbreak at 15 point sources from 2 to 30m with a vertical separation of 2m. *c)* Stationary release conditions 200m ($x = -230\text{ m}$) upwind of the windbreak at 16 point sources from 1 to 30m with a vertical separation of 1m between the lowest two source heights and a vertical separation of 2m between the heights above. The solid black lines denote the windbreak and the dots denote particles (every 30th particle shown). All cases represent the 4 s^{-1} velocity class.

concentration c_0 . By comparing the value of β_c at T_1 to any point in the domain the relative error induced by the assumption of longitudinal uniformity of background concentration (see Fig. 5.2) is obtained with:

$$\beta_e(x, z_s) = \frac{\beta_c(x_{T_1}, z_s) - \beta_c(x, z_s)}{\beta_c(x_{T_1}, z_s)}, \quad (5.1)$$

where $x_{T_1} = -50\text{ m}$, i.e. at the longitudinal position of the upwind measurements of tower T_1 . With respect to the sensor positions, the largest underestimation (-22.3%) would result in the case of the velocity class 1 ms^{-1} at 200m downwind of the birch stand (Fig. 5.2a). The largest overestimation (13.1%) would also result in the case of the velocity class 1 ms^{-1} at the upper sensor 350m downwind of the birch stand. In general, the background concentration is mostly underestimated in all wind velocity classes. Only at the furthest sensor location, both near the ground and at a height of 18m, the background concentration is mostly overestimated. The best agreement is also found at the furthest position in the velocity class 2 ms^{-1} .

The error of the uniform concentration approach basically results from an underestimation of the accumulation in the near downwind area and an underestimation of the deposition at the furthest locations. The substantial errors induced by assuming a longitudinally uniform background concentration based on the upwind measurements thus underline the importance of simulating the transport of background pollen through the disturbed wind field.

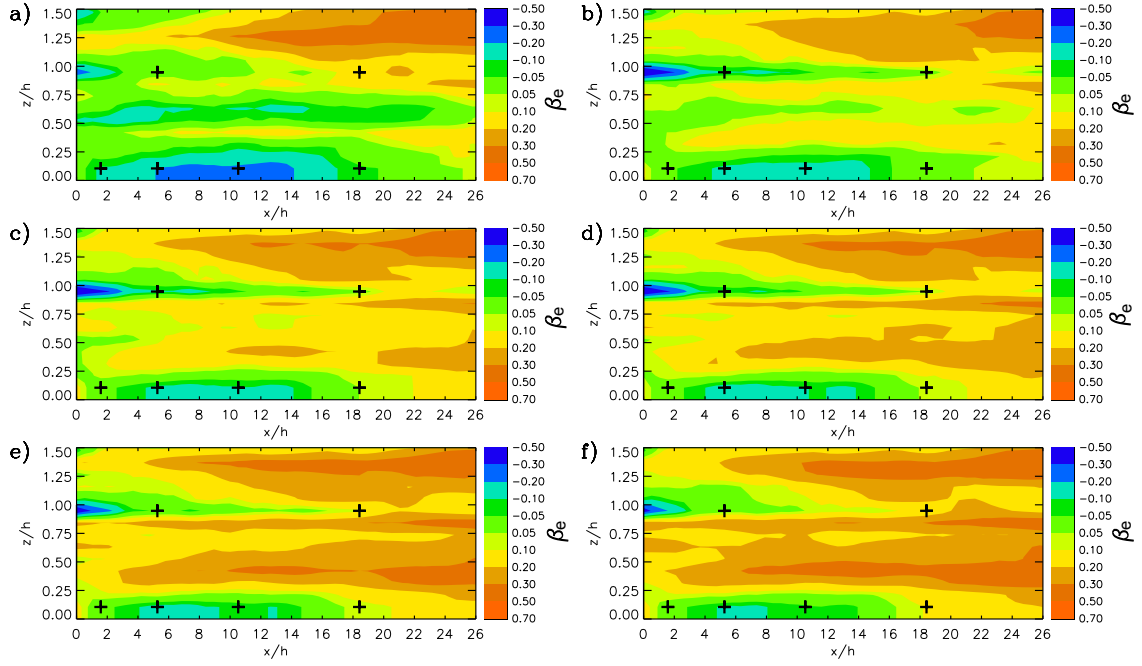


Figure 5.2: Relative error of the modelled background concentration between longitudinally uniform and disturbed background concentration in the case of a vertically uniform background concentration field. The relative error is calculated via Eq. 5.1. Negative values indicate an underestimation, positive values indicate an overestimation of background concentration. *Panels a-f:* Velocity classes 1 through 6 ms^{-1} . Plus signs indicate the positions of the Burkard measurements.

6 On the estimation of pollen emission using a Lagrangian dispersion model

6.1 Introduction

With the information of the CFD model on the distribution of background concentration in the downwind area (Section 5.2), its part of the observed concentration can be eliminated with respect to wind velocity, height above ground and distance from the source, according to the pollen source profile $Q_p = f(U, x, z)$. The residual pollen load should thus represent a concentration, which is related solely to pollen released from the isolated source. In order to infer the absolute emission flux of the isolated source, a three-dimensional stochastic Lagrangian particle model is used to reproduce observations of the background-corrected measurements. In the case of congruency between measured and simulated distribution of pollen in the downwind area, the applied source strength in the model can be used as an estimate for the natural emission flux.

This approach is tested for a single case using AOC measurements of an IOP for the information on the longitudinal and lateral pollen distribution pattern in the downwind area.

6.2 The LPDM model

For the estimation of pollen emission from β_c -corrected observations of pollen concentration, a three-dimensional Lagrangian stochastic particle dispersion model (LPDM) is used, which is based on the two-dimensional model by Rotach et al. (1996). The extension of the latter model to three dimensions is described in De Haan and Rotach (1998). The LPDM uses a pdf of particle velocities, which is suitable for neutral (Gaussian pdf for u , v and w) to convective conditions (skewed pdf for w , Gaussian for u and v). The model is, therefore, capable of simulating the atmospheric conditions at the experiment site during daytime, i.e. unstable conditions (see Section 3.3). In the three-dimensional LPDM, concentrations are estimated with density kernels (De Haan, 1999). In this methodology, the mass represented by particles is spread out spatially as function of a density distribution. Note that in the LPDM the settling velocity is not incorporated.

The LPDM originally uses a single point source, which can be shifted among the domain in three dimensions to define the release location. In this thesis, the model was adapted in order to represent the dimension of the birch stand. Any number of sources with individual locations can be defined. However, all particles released within one timestep at the different locations, behave identically. Hence, turbulence characteristics are spatially uniform in one timestep. This method allows to simulate the simultaneous emission from different source locations, which corresponds to the natural case. Since the LPDM uses a fixed coordinate system, the wind direction observed in the field is accounted for by shifting each sensor and source location in relation to the normal wind approach in the model.

The required input for the model, i.e. turbulence characteristics, including the Obukhov length L as a measure of atmospheric stability, and a wind velocity profile, is obtained from the observations at T_1 .

6.3 Assessment of the approach

In order to simulate the pollen emission from the birch stand, an array of 40 sources in the cross-wind direction (200 m) with a horizontal separation of 5 m and 15 sources in the vertical dimension with a vertical separation of 1 m was set-up, yielding a total of 615 individual sources.

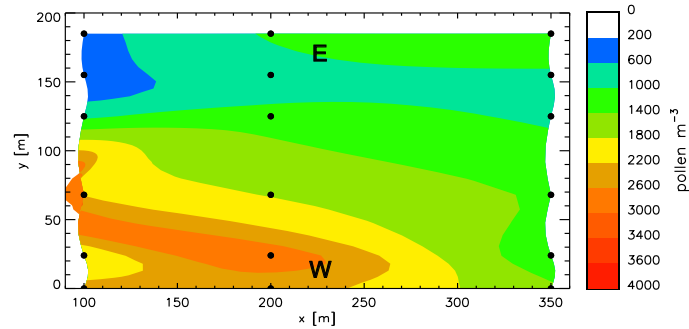


Figure 6.1: Interpolated β_c -corrected longitudinal and lateral downwind pollen concentration observed with AOC sensors at 2 m height in a single two hour interval on 14 April 2010 12-14 UTC+1. The dots denote the location of the used AOC samplers. E denotes east and W denotes west.

The lowest source points were located at a height of 5 m, which corresponds approximately to the lower limit of the crown area. The relative source strength was estimated according to the manual evaluation of the potential source strength (see Fig. 2.2). Figure 6.1 shows the interpolated longitudinal and cross-wind distribution of birch pollen concentration measured on 14 April 2010 12-14 UTC+1. Based on the corresponding meteorological observations, which in this case indicate weakly unstable conditions ($\zeta = -0.2$) and a mean wind direction of 352.5° , the model was initiated with 500 particles per source, yielding a total number of particles per timestep of $n_p=307500$. The internal timestep was 0.1 s and every 0.2 s the output was written.

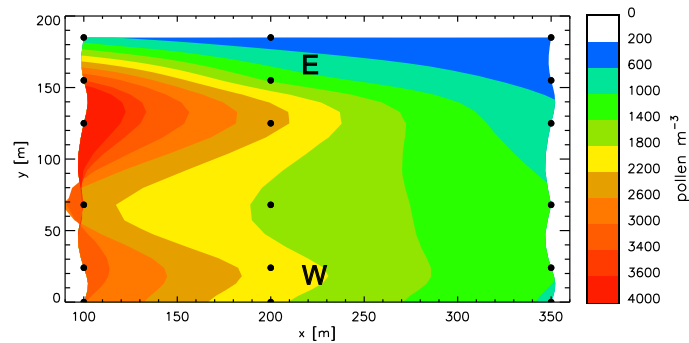


Figure 6.2: Interpolated modelled longitudinal and lateral downwind pollen concentration at 2 m height for the situation on 14 April 2010 14 UTC+1. The dots denote the location of the Air-O-Cell samplers. E denotes east and W denotes west.

Based on the longitudinal transect of the β_c -corrected AOC observations at the cross-wind position of 70 m in Fig. 6.1, the vertical source strength of the LPDM was scaled empirically. In order to achieve the rapidly decreasing concentration with increasing distance from the source, the strongest sources were positioned at 18 m, which is approximately 1 m below the crown top of the birch trees. The resulting modelled concentration field, which is interpolated based on the sensor locations only (Fig. 6.2), resembles the measured pattern only at the longitudinal transect, where the source strength was scaled. In the modelled case, the signal of the cross-wind potential source strength (Fig. 2.2) is clearly visible. In accordance with the measured concentration pattern, the influence of the wind direction (approximately $+10^\circ$ from normal approach) is indicated by a slight shift of the dispersion towards southwest.

Based on the total number of particles released from one source, the relative weight of one 'pollen'

can be estimated. For this particular case, the average emission strength of the birch stand determined at the downwind face of the canopy (at $x = 0$) is $0.07 \text{ pollen m}^{-2}\text{s}^{-1}$. The method of inferring the emission from observed concentration with a Lagrangian particle model works in theory. However, the large discrepancies between the measured and modelled concentration distribution can be related to uncertainties of the observation, over- or underestimation of the potential source strength, or to non-stationary wind conditions.

7 Summary and conclusions

In this thesis an extensive field study used a large instrumental array in order to continuously observe the dispersion of birch pollen from an isolated source with respect to micrometeorological factors. The instrumentation included meteorological and aerosol sensors with a high temporal and spatial resolution, comprising horizontal alignment in the longitudinal and cross-wind direction as well as vertical alignment. The observation of pollen concentration up- and downwind of the pollen source with respect to simultaneous longitudinal and vertical variation is a key feature of the experimental set-up. The situation of the experiment site in a valley dominated by persistent wind conditions allowed to investigate dispersion patterns with respect to upwind and downwind conditions. The observational array aimed at inferring the source strength of an isolated source in the micro-scale in order to enhance the accuracy of the emission parameter in operational prognostic transport models.

Performance and uncertainty of aerosol samplers: The high spatial resolution of the experimental set-up demanded for the use of different aerosol samplers, including self-fabricated sensors. In order to obtain a consistent standard accuracy between different sampler types, the agreement of the sensors was assessed based on in-situ measurements and in reference to the standard instrument (wind-aligned Burkard trap). Apart from certain errors related to the manual analysis method, the results indicate a substantial underestimation of the pollen abundance (-104% relative bias) as function of wind velocity in the case of upward-facing sensors (Air-O-Cell sampler). The error relates to the effect of inertia on the response time of heavy birch pollen to abrupt changes of direction, which is most pronounced in the case of vertical aspiration, i.e. normal to the mean wind.

The large uncertainty of Air-O-Cell samplers was investigated in three separate field intercomparison studies including different pollen species, which aimed at determining the relative error to the Burkard reference. With respect to wind velocity, the influence of sampler orientation was assessed by using vertically as well as horizontally aligned instruments. The effect of particle inertia was confirmed with good agreements of horizontally oriented Air-O-Cell samplers with the Burkard reference. The correction of the erroneous samplers with a physically-based function developed for light particles in the Stokesian regime proved to be unfit for the heavy birch pollen. Therefore, an in-situ correction algorithm based on the longitudinal wind component was established, which mitigated the relative bias to 3%. However, the intercomparison also revealed a substantial precision error of the reference instrument (38% relative root mean square error). The findings of the sampler intercomparison lead to the recommendation that only wind-oriented samplers should be used, when heavy particles are to be monitored.

In general, the uncertainty and precision error of bioaerosol samplers is often underestimated in experimental field studies focussing on atmospheric concentrations, because inaccuracies related to inertial motion are also induced due to convergence and divergence of the freestream upwind of a sampler body. For the case of the widely used Burkard samplers, an empirically derived correction function from the literature was used to correct the data.

However, it must be stated, that the significance of the results presented in this thesis is reduced to a certain degree by the substantial uncertainty of all used aerosol samplers.

Quantification of the background concentration bias: The persistent wind direction during the experimental campaign allowed to divide the experiment site into a upwind and downwind area, in terms of their location in front of or behind the isolated source. The upwind pollen observations were used to determine the background concentration in the experiment area, since the downwind readings are substantially biased by birch pollen, which originate from regions upwind of the isolated source. In the case of an undisturbed flow, a pollen-loaded Surface Layer is characterised by a horizontally uniform pollen concentration in the longitudinal direction. However, it is

shown that the birch canopy acts as a windbreak, where turbulence is induced mechanically due to friction on the vegetation elements. The approach of assuming a uniform background concentration is thus compromised by the wind flow disturbance.

The contribution of background concentration to the downwind area as function of wind velocity is estimated with a numerical simulation of Lagrangian-based pollen trajectories with respect to the wind field disturbance, which is described by a computational fluid dynamics (CFD) model based on the Reynolds-averaged Navier-Stokes method. The results indicate a substantial longitudinal variation of background concentration due to the pollen settling velocity alone. In general, locations further away from the windbreak are less influenced by background concentration. Closer to the source, the background signal behind the windbreak can even exceed the upwind case in low wind velocities, since pollen tend to accumulate due to flow deceleration within the canopy. The distribution of pollen behind the windbreak is also influenced by deposition within the canopy on vegetation obstacles such as stems, branches and leaves. This filtering effect is a function of the windbreak porosity, which is proportional to the leaf-area density of the canopy. In addition to the wind field disturbance, the filtering effect is estimated separately with a model based on the optical porosity. Both effects combined yield an estimate of the total windbreak effect on pollen transport across the shelterbelt. In the case of the birch stand, however, the effect of deposition within the canopy is substantially smaller than the effect of wind field disturbance.

Since the background simulation is used to correct a long time series rather than individual cases, the numerical simulations are generalised by determining the ratio of down- to upwind concentrations. Applying the simulated ratio to measured upwind concentrations allows to predict the actual background concentration. The simulated concentration upwind of the birch stand indicates a substantial influence 20 m in front of the canopy due to the development of a boundary layer around the roughness element. These findings illustrate that undisturbed conditions are only found further away from the birch stand.

Regardless of the plausibility of the numerical simulation, a conclusive evaluation of the model results can only be achieved by reproducing the simulated pattern by artificially released particles or by monitoring different pollen species. In this thesis, however, a significant model validation was not feasible. Furthermore, non-stationary conditions of pollen emission and wind direction in the natural environment result in large discrepancies between observations and the numerical simulation.

Estimating the emission with a Lagrangian particle model: Based on a single case of Air-O-Cell observations, which are corrected for their vertical orientation as well as cleared of the portion of background concentration, the approach of inferring the corresponding emission from the isolated source is tested. The basic idea is to reproduce an observed pollen distribution by adapting the strength and distribution of simulated sources with respect to the natural dimensions of the birch stand. Based on the used input parameters, the corresponding emission characteristics yielding the observed pattern and absolute concentration can be determined. The results indicate that the method is feasible in theory. However, the reference dataset is subject to a series of uncertainties and corrections, which makes it difficult to estimate its reliability and thus to evaluate the accuracy of the simulated case.

In conclusion, it is stated that the main goal, i.e. obtaining a robust estimation of pollen emission from the birch stand with respect to micrometeorological factors, could not be fulfilled conclusively. The problems encountered in this thesis relate, on the one hand, to shortcomings of the experimental design: Firstly, the use of untested pollen samplers in combination with their vertical orientation initiated a series of studies, which were only marginally related to the main goal, yet essential for its pursuit. Secondly, the complexity of the distribution of background pollen concentration in the downwind area was substantially underestimated. However, since the thesis aimed at determining *natural* birch pollen emission, this problem could only have been avoided, if the experiment had been located in an environment with zero background concentration. On the

other hand, certain problems arose from non-stationary conditions of pollen emission and wind conditions in the case of highly resolved measurements in the temporal dimension.

However, the evaluation of uncertainties in pollen observations with a high temporal resolution provided further knowledge at the interface of health-related and biometeorological studies. Also, the use of the CFD model in combination with respect to the pollen settling velocity, i.e. their inertial motion, and deposition within the birch canopy, is a great benefit for ongoing studies in related fields of research.

Outlook: The knowledge gained from the extensive field study can be used to adapt and improve future similar field experiments with respect to the provided information on the used material, sensor uncertainties and pitfalls in terms of applied methods. The use of a three-dimensional CFD model to simulate emission and dispersion of pollen as well as the distribution of background concentration could be very promising in order to take into account all factors related to the atmospheric conditions and pollen abundance presented in this thesis.

Bibliography

- Armbruster, L. and Breuer, H. (1982), *Investigations into defining inhalable dust*, Pergamon, Oxford, pp. 3–19.
- Arritt, R., Clark, C., Goggi, A., Sanchez, H., Westgate, M. and Riese, J. (2007), ‘Lagrangian numerical simulations of canopy air flow effects on maize pollen dispersal’, *Field Crops Research* **102**, 151–162.
- Aylor, D. (1990), ‘The role of intermittent wind in the dispersal of fungal pathogens’, *Annu. Rev. Phytopathol.* **28**, 73–92.
- Aylor, D., Boehm, M. and Shields, E. (2006), ‘Quantifying aerial concentrations of maize pollen in the atmospheric surface layer using remote-piloted airplanes and lagrangian stochastic modeling’, *J. Appl. Meteorol.* **45**(7), 1003–1015.
- Aylor, D. and Flesch, T. (2001), ‘Estimating spore release rates using a Lagrangian stochastic simulation model’, *J. App. Meteorol.* **40**, 1196–1208.
- Badzioch, S. (1959), ‘Collection of gas-borne dust particles by means of an aspirated sampling nozzle’, *Br. J. Appl. Phys.* **10**, 26–32.
- Bates, D., Fish, B., Hatch, T. and Morrow, P. (1966), ‘Deposition and retention models for internal dosimetry of human respiratory tract’, *Health Physics* **12**, 173–207.
- Belyaev, S. and Levin, L. (1974), ‘Techniques for collection of representative aerosol samples’, *J. Aerosol Sci.* **5**, 325–338.
- Boehm, M. and Aylor, D. (2005), ‘Lagrangian stochastic modeling of heavy particle transport in the convective boundary layer’, *Atmos. Environ.* **39**, 4841–4850.
- Boehm, M., Aylor, D. and Shields, E. (2008), ‘Maize pollen dispersal under convective conditions’, *J. of App. Meteorol.* **47**, 291–307.
- Bouvet, T., Loubet, B., Wilson, J. and Tuzet, A. (2007), ‘Filtering of windborne particles by a natural windbreak’, *Bound.-Lay. Meteorol.* **123**, 481–509.
- Brunet, Y., Foueillassar, X., Audran, A., Garrigou, D. and Dayau, S. (2004), ‘Evidence for long-range transport of viable maize pollen.’, *Preprints, 16th Conf. on Biometeorology and Aerobiology, Vancouver BC, Canada, Amer. Meteor. Soc. CD-ROM, P4A.2*.
- Chamecki, M., Meneveau, C. and Parlange, M. (2009), ‘Large eddy simulation of pollen transport in the atmospheric boundary layer’, *J. Aerosol Sci.* **40**, 241–255.
- Cleugh, H. (1998), ‘Effects of windbreaks on airflow, microclimates and crop yields’, *Agroforestry Systems* **41**, 55–84.
- Cleugh, H. (2002), ‘Field measurements of windbreak effects on airflow, turbulent exchange and microclimates’, *Australian Journal of Experimental Agriculture* **42**, 665–677.
- Comtois, P., Fernández-Gonzales, D., Valencia-Barrera, R., Sánchez, J., Fraile, R. and Rodier, S. (2000), ‘Pollen content study of the lower atmosphere in León (Spain) by use of a tethered balloon’, *Aerobiologia* **16**, 187–191.
- De Haan, P. (1999), ‘On the use of density kernels for concentration estimations within particle and puff dispersion models’, *Atmos. Envir.* **33**, 2007–2021.
- De Haan, P. and Rotach, M. (1998), ‘A novel approach to atmospheric dispersion modelling: The Puff-Particle-Model’, *Quart. J. Roy. Meteor. Soc.* **124**, 2771–2792.
- Dupont, S., Brunet, Y. and Jarosza, N. (2006), ‘Eulerian modelling of pollen dispersal over hete-

- rogeous vegetation canopies', *Agr. Forest Meteorol.* **141**, 82–104.
- Durham, M. and Lundgren, D. (1980), 'Evaluation of aerosol aspiration efficiency as function of Stokes number, velocity ratio and nozzle angle', *J. Aerosol Sci.* **11**, 179–188.
- Frenz, D. (1999), 'Comparing pollen and spore counts collected with the Rotorod sampler and Burkard spore trap', *Ann. Allergy Asthma Immunol.* **83**, 341–347.
- Galán, C., Cariñanos, P., García-Mozo, H., Alcázar, P. and Domínguez-Vilches, E. (2001), 'Model for forecasting *Olea europea* L. airborne pollen in South-West Andalusia, Spain', *Int. J. Biometeorol.* **45**, 59–63.
- Grinshpun, S., Chang, C.-W., Nevalainen, A. and Willeke, K. (1994), 'Inlet characteristics of bioaerosol samplers', *J. Aerosol Sci.* **25**(8), 1503–1522.
- Grinshpun, S. and Lipatov, G. (1990), 'Sampling errors in cylindrical nozzles', *Aerosol Sci. Technol.* **12**, 716–740.
- Guo, L. and Maghirang, R. (2012), 'Numerical simulation of airflow and particle collection by vegetative barriers', *Enginee* **6**, 110–122.
- Hangal, S. and Willeke, K. (1990a), 'Aspiration efficiency: unified model for all forward sampling angles', *Envir. Sci. Technol.* **24**, 688–691.
- Hangal, S. and Willeke, K. (1990b), 'Overall efficiency of tubular inlets sampling at 0-90 degrees from horizontal aerosol flows', *Atmos. Envir.* **24A**, 2379–2386.
- Helbig, N., Vogel, B., Vogel, H. and Fiedler, F. (2004), 'Numerical modelling of pollen dispersion on the regional scale', *Aerobiologia* **3**, 3–19.
- Hirst, J. (1952), 'An automatic volumetric spore trap', *Ann. Appl. Biol.* **39**, 257–265.
- Jäger, S. (1990), 'Tageszeitliche Verteilung und langjährige Trends bei allergiekompetenten Pollen', *Allergologie* **13**(5), 159–182.
- Jarosz, N., Loubet, B., Durand, B., Foueillassar, X. and Huber, L. (2005), 'Variations in maize pollen emission and deposition in relation to microclimate', *Environ. Sci. Technol.* **39**, 4377–4384.
- Jarosz, N., Loubet, B., Durand, B., McCartney, A., Foueillassar, X. and Huber, L. (2003), 'Field measurements of airborne concentration and deposition rate of maize pollen', *Agr. Forest Meteorol.* **119**, 37–51.
- Jarosz, N., Loubet, B. and Huber, L. (2004), 'Modelling airborne concentration and deposition rate of maize pollen', *Atmos. Envir.* **38**, 5555–5566.
- Kaimal, J. and Finnigan, J. (1994), *Atmospheric boundary layer flows: their structure and measurement*, Oxford University Press, Oxford, United Kingdom.
- Lacey, M. and West, J. (2006), *The Air Spora: A manual for catching and identifying airborne biological particles*, Springer, Dordrecht.
- Lavigne, C., Godelle, B., Reboud, X. and Gouyon, P. (1996), 'A method to determine the mean pollen dispersal of individual plants growing within a large pollen source', *Theor. Appl. Genet.* **93**, 1319–1326.
- Lavigne, C., Klein, E., Vallée, P., Pierre, J., Godelle, B. and Renard, M. (1998), 'A pollen-dispersal experiment with transgenic oilseed rape. Estimation of the average pollen dispersal of an individual plant within a field', *Theor. Appl. Genet.* **96**, 886–896.
- Levetin, E. (2004), 'Methods for aeroallergen sampling', *Current Allergy and Asthma Reports* **4**, 376–383.

- Linkosalo, T., Rantab, H., Oksanenb, A., Siljamoc, P., Luomajokid, A., Kukkonenc, J. and Sofiev, M. (2010), 'A double-threshold temperature sum model for predicting the flowering duration and relative intensity of *betula pendula* and *b. pubescens*', *Agr. Forest Meteorol.* **150**, 1579–1584.
- Lipatov, G., Grinshpun, S., Semenyuk, T. and Sutugin, A. (1988), 'Secondary aspiration of aerosol particles into thin-walled nozzles facing the wind', *Atmos. Envir.* **22**, 1721–1727.
- Loeffler, A., Gordon, A. and Gillespie, T. (1992), 'Optical porosity and windspeed reduction by coniferous windbreaks in southern Ontario', *Agro* **17**, 119–133.
- Lundgren, D., Durham, M. and Mason, K. (1978), 'Sampling of tangential flow streams', *Am. Ind. Hyg. Assoc. J.* **39**, 640644.
- Mahura, A., Baklanov, A. and Korsholm, U. (2009), 'Parameterization of the birch pollen diurnal cycle', *Aerobiologia* **25**, 203–208.
- Mandrioli, P., Comtois, P. and Levizzani, V. (1998), *Methods in aerobiology*, Pitagora Editrice, Bologna, Italy.
- Masanari, S. and Tadashi, K. (2003), 'Development of automatic pollen monitor and its performance', *Papers of Technical Meeting on Micromachine and Sensor System, IEE Japan* .
- McNaughton, K. (1988), 'Effects of windbreaks on turbulent transport and microclimate', *Agriculture, Ecosystems and Environment* **22/23**, 17–39.
- Méndez, J., Comtois, P. and Iglesias, I. (2005), 'Betula pollen: One of the most important aeroallergens in Ourense, Spain', *Aerobiologia* **21**, 115–123.
- Mercer, G. (2009), 'Modelling to determine the optimal porosity of shelterbelts for the capture of agricultural spray drift', *Environmental modelling & software* **24**, 1349–1352.
- Nieddu, G., Chessa, I., Canu, A., Pellizzaro, G., Sirca, C. and Vargiu, G. (1997), 'Pollen emission from olive trees and concentrations of airborne pollen in an urban area of North Sardinia', *Aerobiologia* **13**, 235–242.
- Obukhov, A. (1946), 'Turbulence in an atmosphere with a non-uniform temperature', *Tr. Inst. Teor. Geofiz. Akad. Nauk. SSSR* **1**, 95–115.
- Ogden, E., Hayes, J. and Raynor, G. (1969), 'Diurnal patterns of pollen emission in *Ambrosia*, *Phleum*, *Zea* and *Ricinus*', *Amer. J. Bot.* **56**(1), 16–21.
- Ogden, E., Raynor, G., Hayes, J., Lewis, D. and Haines, J. (1974), *Manual for sampling airborne pollen*, Hafner Press, New York.
- Ogden, T. and Birkett, J. (1977), *The human head as a dust sampler*, Pergamon Press, Oxford, pp. 93–105.
- Paik, S. and Vincent, J. (2002), 'Aspiration efficiency for thin-walled nozzles facing the wind and for very high velocity ratios', *J. Aerosol Sci.* **33**, 705–720.
- Raabe, O. (1976), 'Aerosol aerodynamic size conventions for inertial sampler calibration', *J. Air Pollut. Control Assoc.* **26**, 856–860.
- Raupach, M., Woods, N., Dorr, G., Leys, J. and Cleugh, H. (2001), 'The entrapment of particles by windbreaks', *Atmos. Envir.* **35**, 3373–3383.
- Raynor, G., Hayes, J. and Ogden, E. (1974), 'Mesoscale transport and dispersion of airborne pollens', *J. App* **13**, 87–95.
- Raynor, G., Ogden, E. and Hayes, J. (1970), 'Dispersion and deposition of Ragweed pollen from experimental sources', *J. Appl. Meteorol.* **9**, 885–895.
- Reynolds, A. (1999), 'A Lagrangian stochastic model for heavy particle deposition', *J. Colloid*

- Interface Sci.* **215**, 85–91.
- Reynolds, A. (2000), ‘On the formulation of Lagrangian stochastic models for heavy-particle trajectories’, *J. Colloid Interface Sci.* **232**, 260–268.
- Ronneberger, O. (2007), 3D Invariants for automated pollen recognition, PhD thesis, Fakultät für Angewandte Wissenschaften der Albert-Ludwigs-Universität Freiburg im Breisgau.
- Rosenfeld, M., Marom, G. and Bitan, A. (2010), ‘Numerical simulation of the airflow across trees in a windbreak’, *Bound.-Lay. Meteorol.* **135**, 89–107.
- Rotach, M., Gryning, S. and Tassone, C. (1996), ‘A two-dimensional Lagrangian stochastic dispersion model for daytime conditions’, *Quart. J. Roy. Meteor. Soc.* **122**(530), 367–389.
- Santiago, J., Martín, F., Cuerva, A., Bezdenejnykh, N. and Sanz-Andrés, A. (2007), ‘Experimental and numerical study of wind flow behind windbreaks’, *Atmospheric Environment* **41**, 6406–6420.
- Schueler, S. and Schlünzen, K. (2006), ‘Modeling of oak pollen dispersal on the landscape level with a mesoscale atmospheric model’, *Environ. Model Assess* **11**, 179–194.
- Shigeto, K., Toshio, F., Kazuhito, M. and Hiroyuki, S. (2004), ‘Development of an automatic corn pollen monitor’, *Jap. J. Palynol.* **50**, 5–14.
- Shigetoshi, Y., Tadao, E. and Akira, S. (2005), ‘A comparative study between real time monitor KH-3000 and conventional Durham sampler measuring airborne pollen’, *Nippon Jibiinkoka Gakkai Kaiho* **108**, 801–805.
- Siljamo, P., Sofiev, M., Filatova, E., Grewling, L., Jäger, S., Khoreva, E., Linkosalo, T., Jimenez, S., Ranta, H., Rantio-Lehtimäki, A., Svetlov, A., Veriankaitė, L., Yakovleva, E. and Kukkonen, J. (2013), ‘A numerical model of birch pollen emission and dispersion in the atmosphere. Model evaluation and sensitivity analysis’, *Int. J. Biometeorol.* **57**, 125–135.
- Skjøth, C., Brandt, J., Christensen, J., Løfstrøm, P., Frohn, L., Geels, C., Hvidberg, M., Frydendall, J. and Hansen, K. (2006), THOR: An operational and integrated model system for air pollution and pollen forecasts, in ‘Proceedings of 8th International Congress on Aerobiology, “Towards a comprehensive vision”’, Neuchâtel, Switzerland, 21-25 August 2006.
- Sofiev, M., Siljamo, P., Ranta, H. and Rantio-Lehtimäki, A. (2006a), ‘Towards numerical forecasting of long-range air transport of birch pollen: theoretical considerations and a feasibility study’, *Int. J. Biometeorol.* **50**, 392–402.
- Sofiev, M., Siljamo, P., Valkama, I., Ilvonen, M. and Kukkonen, J. (2006b), ‘A dispersion modelling system SI-LAM and its evaluation against ETEX data’, *Atmosph. Environ.* **40**, 674–685.
- Sofiev, M., Siljamo, P. and Ranta, H., Linkosalo, T., Jaeger, S., Rasmussen, A., Rantio-Lehtimäki, A., Severova, E. and Kukkonen, J. (2013), ‘A numerical model of birch pollen emission and dispersion in the atmosphere. Description of the emission module’, *Int. J. Biometeorol.* **57**, 45–58.
- Steinacker, R. (1984), ‘Areaheight distribution of a valley and its relation to the valley wind’, *Contrib. Atmos. Phys.* **57**, 64–71.
- Stöber, W. (1972), *Assessment of Airborne Particles*, Charles C. Thomas, Springfield, Illinois.
- Stull, R. (1988), *An introduction to Boundary Layer Meteorology*, Kluwer Academic Publishers, Dordrecht, The Netherlands.
- Takahashi, Y., Kawashima, S. and Fujita, T. (2001), ‘Comparison between real-time pollen monitor KH-3000 and Burkard sampler’, *Aerugi* **50**, 1136–42.
- Tsai, P. and Vincent, J. (1993), ‘Impaction model for the aspiration efficiencies of aerosol samplers at large angles with respect to the wind’, *J. Aerosol Sci.* **24**, 919–928.

- Van Hout, R., Chamecki, M., Brush, G., Katz, J. and Parlange, M. (2008), ‘The influence of local meteorological conditions on the circadian rhythm of corn (*Zea mays* L.) pollen emission’, *Agr. Forest Meteorol.* **148**, 1078–1092.
- Venkatram, A. and Wyngaard, J. (1988), *Lectures on air pollution modeling*, American Meteorological Society, Boston.
- Vigiak, O., Sterk, G., Warren, A. and Hagen, J. (2003), ‘Spatial modeling of wind speed around windbreaks’, *Catena* **52**, 273–288.
- Vincent, J. (1987), ‘Recent advances in aspiration theory for thin-walled and blunt aerosol sampling probes’, *J. Aerosol Sci.* **18**, 487–498.
- Vincent, J. (1989), *Aerosol Sampling: Science and Practice*, John Wiley & Sons, Ltd., Chichester.
- Vincent, J. (2007), *Aerosol Sampling: Science, Standards, Instrumentation and Applications*, John Wiley & Sons, Ltd., Chichester.
- Vincent, J., Stevens, D., Mark, D., Marshall, M. and Smith, T. (1986), ‘On the aspiration characteristics of large-diameter, thin-walled aerosol sampling probes at yaw orientations with respect to the wind’, *J. Aerosol Sci.* **17**, 211–224.
- Von Wahl, P.-G. and Puls, K. E. (1989), ‘The emission of mugwort pollen (*Artemisia vulgaris* L.) and its flight in the air’, *Aerobiologia* **5**, 55–63.
- Šaulienė, I. and Veriankaitė (2012), ‘Analysis of high allergenicity airborne pollen dispersion: common ragweed study case in Lithuania’, *Annals* **19**, 415–419.
- Weigel, A., Chow, F., Rotach, M., Street, R. and Xue, M. (2006), ‘High-resolution Large-Eddy Simulations of flow in a steep alpine valley. Part II: Flow structure and heat budgets’, *J. Appl. Meteorol.* **45**, 87–107.
- Wenneker, M., Heijne, B. and Van De Zande, J. C. (2005), ‘Effect of natural windbreaks on drift reduction in orchard spraying’, *Commun. Agric. Appl. Biol. Sci.* **70**, 961–969.
- Wiener, R., Okazaki, K. and Willeke (1988), ‘Influence of turbulence on aerosol sampling efficiency’, *Atmos. Envir.* **22**, 917–928.
- Wilson, J. (1985), ‘Numerical studies of flow through a windbreak’, *Journal of Wind Engineering and Industrial Aerodynamics* **21**, 119–154.
- Wilson, J. (2000), ‘Trajectory models for heavy particles in atmospheric turbulence: Comparison with observations’, *J. Appl. Meteorol.* **39**, 1894–1912.

Appendix A Pollen concentration in high elevations

A.1 Methods

During discrete intervals (Table A.2), pollen concentrations in high elevations were observed using a tethered balloon ascending to a maximum height of 300 m above the ground downwind of the birch stand. The limited payload of the balloon required a light and stand-alone pollen sampler type. Three Rotorod Model 20 samplers (Sampling Technologies Inc.) (Mandrioli et al., 1998) were attached to the balloon cord (Fig. A.1). The pollen sampler consists of a electric motor which rotates two vertical four-sided rods. The lateral surface facing towards the rotation direction is coated with silicone. Airborne pollen are trapped as the rods move through the air. From the rectangular area moving ahead and the cyclic distance covered in a certain amount of time, a volume can be determined which corresponds to the sampling volume. The pollen concentration can be calculated via $c = n_p/3.12$, where n_p is the number of trapped pollen. The rotation rate is 2400 rpm. It was necessary to modify the original design of the Rotorods to achieve a lower weight and fix them to the tether. The temporal resolution of the measurements is one hour. During the ascent and descent, respectively, the Rotorods were not operated in order to avoid the signal to be biased by different layers. If the instrument is not operated, the rods are spring-retracted and thus not exposed to pollen. The counting procedure was performed according to the AOC analysis method.

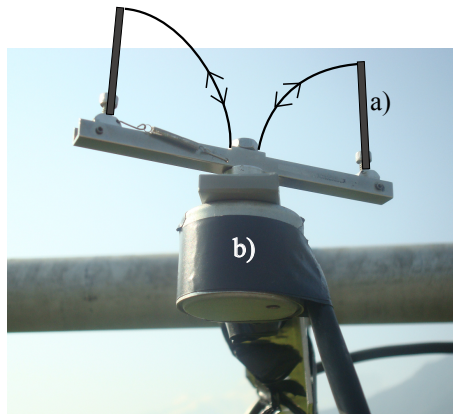


Figure A.1: Rotorod sampler [mounted in the field during the intercomparison experiment 2009 (Section 4.4)]. *a)* The position of sampling rods during operation. The arrows denote the movement of the sampling rods between idle (horizontal) and operation mode (vertical). *b)* Electric motor producing 2400 rotations per minute.

A.2 Observations

Figure A.2 shows that the abundance of birch pollen in higher elevations was substantial. However, the concentrations rapidly decrease with height. At 25 m above the ground the measurements range from 300 to 900 pollen m^{-3} . Above a height of 100 m and up to 260 m the concentrations already decreased to a range from 50 to 350 pollen m^{-3} . Hence, the findings of Comtois et al. (2000) and Brunet et al. (2004), which indicate a uniform profile of pollen concentration up to 1500 m or even higher concentrations than near the ground, could not be confirmed.

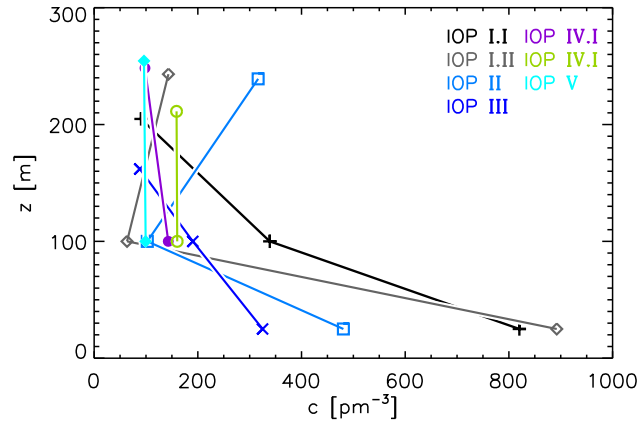


Figure A.2: Birch pollen concentrations measured with Rotord samplers mounted on the tethering of a balloon during intensive operation periods (IOP). In the case of a vertical orientation of the tether the measuring heights were 25 m, 100 m and 290 m above the ground. Real heights are determined via observations of air pressure at a meteorological sensor mounted below the balloon in a height of 300 m in the case of a vertical tether.

Table A.2: Timing of tethered balloon ascents.

IOP number	I	I	II	III	IV	IV	V
time (UTC+1)	13:00	17:00	13:00	13:00	11:00	14:00	11:00

Appendix B Diurnal course of pollen concentrations

The course of pollen concentrations measured near the ground up-and downwind of the windbreak presents a slight diurnal pattern only for average values, which indicates stronger pollen emission during the day. However, a more pronounced increase of concentration is indicated during the night, which could be related to lifting of deposited pollen due to mechanical turbulence or settling of long-range transported pollen.

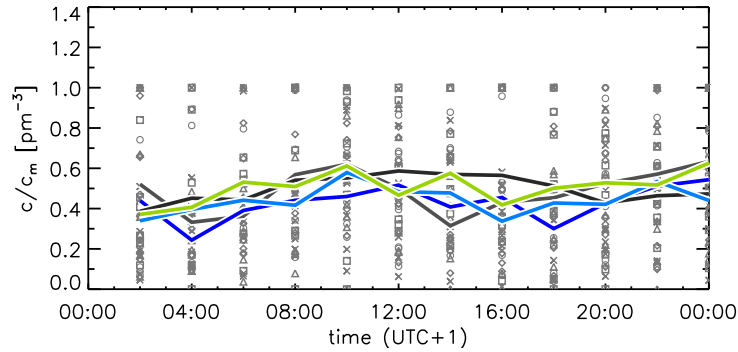


Figure B.1: Diurnal course of normalised pollen concentration observed at 2 m above the ground during the experimental period, using corrected Burkard data (correction described in Section 4.2). The data are normalised with the maximum of the respective 24-hour period. Grey symbols denote two-hourly data of individual Burkard samplers (symbols according to Fig 3.6). The lines denote the average diurnal course for the sensor at 20 m upwind (light grey), 30 m downwind (blue), 100 m downwind (dark grey), 200 m downwind (light blue) and 350 m downwind (green).

Appendix C Perspective correction of the optical porosity profile

The optical porosity of the birch canopy (κ), which is required for the calculation of transmissivity (σ_p) according to Raupach et al. (2001), is determined based on a photograph of the windbreak (Loeffler et al., 1992). $\kappa(z)$ describes the ratio of visible background to the entire area on the respective height along the vertical extent. Since the image of the windbreak was taken near the ground and relatively close to the tree-line at V_p (Fig. C.1), the vertical information of κ is distorted due to perspective. Since $\alpha_a \neq \alpha_b$, where α denotes the angle of perspective related to 1 m in the canopy, the real height in $\kappa(z)$ is corrected as function of distance from the windbreak and the height, where the image was taken.

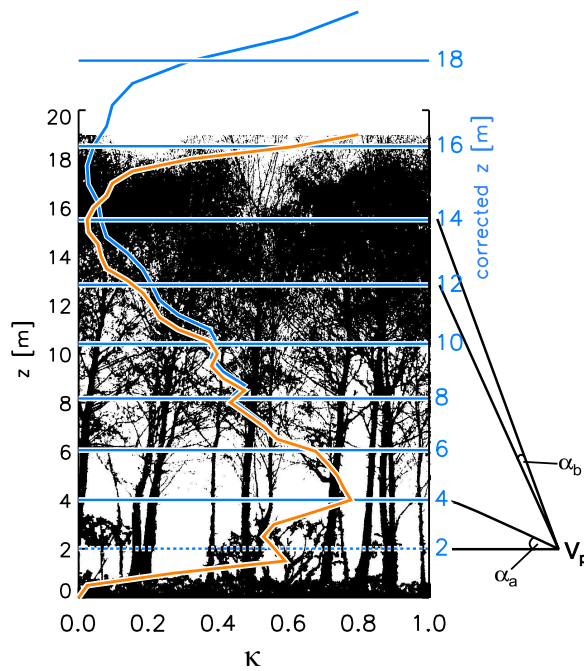


Figure C.1: Perspective correction of the optical porosity (κ). The underlying image of a representative portion of the windbreak is filtered for vegetation objects based on their colour signature, which produces white pixels for background and black pixels for vegetation elements. The orange line denotes the ratio of white pixels to the total number of pixels in a row of the image. The blue line denotes the aspect-ratio corrected profile of κ . The dashed line denotes the height of neutral perspective (V_p , 2 m above the ground), i.e. where the image was taken. α_a and α_b denote angles of perspective, related to 1 m in vertical direction.

Appendix D Stepwise pollen dispersal across a wind-break

The attached CD contains:

- *NormalPollenConcu1.mp4*: Movie of the distribution of normalised pollen concentration into an empty domain for the velocity class 1 ms^{-1} .
- *NormalPollenConcu2.mp4*: Movie of the distribution of normalised pollen concentration into an empty domain for the velocity class 2 ms^{-1} .
- *NormalPollenConcu3.mp4*: Movie of the distribution of normalised pollen concentration into an empty domain for the velocity class 3 ms^{-1} .
- *NormalPollenConcu4.mp4*: Movie of the distribution of normalised pollen concentration into an empty domain for the velocity class 4 ms^{-1} .
- *NormalPollenConcu5.mp4*: Movie of the distribution of normalised pollen concentration into an empty domain for the velocity class 5 ms^{-1} .
- *NormalPollenConcu6.mp4*: Movie of the distribution of normalised pollen concentration into an empty domain for the velocity class 6 ms^{-1} .

The movies show the normalised pollen concentration c_1/c_0 from $t = 0 \text{ s}$ to $t = 1500 \text{ s}$ in the case of the velocity classes 1 to 3 ms^{-1} and from $t = 0 \text{ s}$ to $t = 1000 \text{ s}$ in the case of the velocity classes 4 to 6 ms^{-1} . The upper plot shows the dispersion based on the wind field disturbance only. In the lower plot deposition within the windbreak is enabled. One timestep equals 0.5 s . The replay speed is scaled 33:1. The start and duration of the equilibrium conditions (Section 5.2) for each velocity class is shown in Table D.1.

Table D.1: Start and duration of stationary source conditions in CFD simulations.

velocity class [ms^{-1}]	1	2	3	4	5	6
start time [s]	1300	700	700	600	500	500
duration [s]	200	800	800	400	500	500

Curriculum Vitae

Dominik Michel

Date of birth: 29 November 1980 **Citizenship:** Basel, Switzerland

PostDoc - since 1/2014

Institute for Atmospheric and Climate Science, ETH Zürich, Switzerland. Group Land-Climate Interactions, Prof. Dr. Sonia I. Seneviratne

Dissertation - 5/2008 until 12/2013

Dissertation at the Institute of Meteorology, Climatology, University of Basel, Switzerland: *Observations and modelling of birch pollen emission and dispersion from an isolated source*, supervised by: Prof. Dr. Eberhard Parlow, Prof. Dr. Mathias Rotach, Dr. Roland Vogt

Scientific assistant, ETH Zürich - 6/2012 until 12/2013

Responsible person for the Rietholzbach research site of the Institute for Atmospheric And Climate Science, ETH Zürich, Switzerland. Group Land-Climate Interactions, Prof. Dr. Sonia I. Seneviratne

Assistant, University of Basel - 4/2008 until 12/2013

Assistant at the Institute of Meteorology, Climatology, University of Basel, Switzerland. Various teaching activities (mathematical exercises, meteorological exercises, meteorological seminars, practical exercises for meteorological observations and instruments)

Diploma in Geography 04/2008

Diploma at the Institute of Meteorology, Climatology, University of Basel: *Flux measurements using optical scintillometry and eddy-covariance over inhomogeneous terrain* supervised by Dr. R. Vogt. Diploma examinations in Physical Geography, Human Geography, Meteorology and Nature- and Landscape Conservation and Environmental Protection (NLU)

Internships - 10/2005 until 3/2006

Lufthygieneamt beider Basel, Liestal, Switzerland (Dr. Hansruedi Moser)

Federal Office of Meteorology and Climatology Meteoswiss, Payerne (Dr. Rolf Philipona): Michel, D., Philipona, R., Ruckstuhl, C., Vogt, R., Vuilleumier, L. (2008): *Performance and uncertainty of CNR1 net radiometers during a one year field comparison*, J. Atm. and Oceanic Tech., 25, pp. 442-451, DOI: 10.1175/2007JTECHA973.1.

Student assistant, University of Basel 10/2004 until 3/2008

Student assistant at the Institute of Meteorology, Climatology at the University of Basel, Switzerland. Maintenance and support of the internal observation network as well as maintenance and data control in the framework of the INTERREG-Project Nr. 3c.10 (Dissertation Dr. Irene Lehner) and preparation/support in international experimental campaigns (Sicily, Italy; Pianosa, Italy).

Matura - 12/2000

Swiss high-school degree with focus on Latin, Gymnasium Oberwil, BL

List of publications

- Michel, D., Rotach, M.W., Gehrig, R., Vogt, R.: (2012): *On the efficiency and correction of vertically oriented blunt bioaerosol samplers in moving air*, Int. J. of Biometeorol, **56** (6), pp. 1113-1121, DOI: 10.1007/s00484-012-0526-x.
- Michel, D., Rotach, M.W., Gehrig, R., Vogt, R. (2011): *MicroPoem: Experimentelle Untersuchung der mikrometeorologischen Einflüsse auf die Birkenpollenemission im Rhonetal*, Regio Basiliensis **52** (1): pp. 55-62.
- Michel, D., Rotach, M.W., Gehrig, R., Vogt, R. (2010): *Experimental investigation of micro-meteorological influences on birch pollen emission*, Arbeitsberichte der MeteoSchweiz, **230**, 37 pp.
- Michel, D., Rotach, M.W., Gehrig, R., Vogt, R. (2010): *MicroPoem: Experimental investigation of birch pollen emissions*, 19th Symposium on Boundary Layers and Turbulence, Keystone, CO (extended abstract).
- Michel, D., Philipona, R., Ruckstuhl, C., Vogt, R., Vuilleumier, L. (2008): *Performance and uncertainty of CNR1 net radiometers during a one year field comparison*, J. Atm. and Oceanic Tech., **25**, pp. 442-451, DOI: 10.1175/2007JTECHA973.1.

Conference talks

- Michel, D., Rotach, M.W., Gehrig, R., Vogt, R. (2009): *Set-up of the birch pollen experiment: Impact of micrometeorological factors on birch pollen emission - MicroPoem*, COST Action ES0603 Management Committee meeting, Munich, Germany, 28 - 29 January.
- Michel, D., Rotach, M.W., Gehrig, R., Vogt, R. (2009): *Impact of micrometeorological factors on birch pollen emission - MicroPoem: Description of the field experiment and first results*, COST Action ES0603 Management Committee meeting, Aveiro, Portugal, 12 - 13 October.
- Michel, D., Rotach, M.W., Gehrig, R., Vogt, R. (2010): *MicroPoem: experimental investigation of birch pollen emission*, 19th Symposium on Boundary Layer and Turbulence, Keystone, Colorado, 2 - 8 August 2010.
- Michel, D., Rotach, M.W., Gehrig, R., Vogt, R. (2011): *Experimental investigation of birch pollen emission (MicroPoem) and the influence of sensor orientation and meteorological factors on the inlet sampling characteristics of volumetric bioaerosol samplers*, EGU General Assembly, Vienna, Austria, 3 - 8 April.
- Michel, D., Rotach, M.W., Gehrig, R., Vogt, R. (2011): *MicroPoem: Characteristics of birch pollen dispersion downwind of an isolated source*, COST Action ES0603 Final Management Committee meeting, Berlin, Germany, 14 - 15 October.